RELATIVISTIC JETS FROM COMPACT BINARY MERGERS AS ELECTROMAGNETIC COUNTERPARTS TO GRAVITATIONAL WAVE SOURCES

Gavin Paul Lamb

A thesis submitted in partial fulfilment of the requirements of
Liverpool John Moores University for the degree of Doctor of Philosophy.

January 2018

Declaration

The work presented in this thesis was carried out at the Astrophysics Research Institute, Liverpool John Moores University. Unless otherwise stated, it is the original work of the author.

While registered as a candidate for the degree of Doctor of Philosophy, for which submission is now made, the author has not been registered as a candidate for any other award. This thesis has not been submitted in whole, or in part, for any other degree.

Gavin Paul Lamb

Astrophysics Research Institute

Liverpool John Moores University

IC2, Liverpool Science Park

146 Brownlow Hill

Liverpool

L3 5RF

UK

APRIL 12, 2018

Abstract

The advent of gravitational wave (GW) astronomy has provided a new window through which to view and understand the Universe. To fully exploit the potential of GW astronomy, an understanding of all the potential electromagnetic counterparts to a gravitational wave detected source will help maximise the science returns. Here I present a study of the electromagnetic emission from relativistic jets that accompany the merger of binary neutron stars or black hole neutron star systems. These counterparts provide a probe for the structure and dynamics of these relativistic outflows.

Binary neutron star, or neutron star black hole, mergers are thought to be the dominant progenitor of short gamma-ray bursts (GRBs). Here we investigate the possibility that there is a hidden population of low-Lorentz factor jets resulting in failed GRBs, on-axis orphan afterglows, and what kind of counterparts can be expected given a merger-jet population dominated by these failed-GRB jets. I find that for GW detected mergers, $\sim 80\%$ of the population of on-axis events may result in a failed GRB afterglow. The afterglow of a failed GRB is characterised by the lack of any prompt emission; where the γ-rays are emitted within an optically thick region of the low-Lorentz factor (Γ) outflow and significant suppression via pair production and a high opacity results in the photons coupled to the pair plasma. This plasma will undergo adiabatic expansion, and the photons will decouple at the photospheric radius. The energy in the prompt photons, for a sufficiently low-Γ outflow, will have been signifi-

cantly suppressed.

GW detected mergers have a Malmquist bias towards on-axis events (i.e. the rotational axis of the system), where the peak of the probability distribution is an inclination $\sim 30°$. If the jets from these mergers have an intrinsic structure out to wider angles, then the majority of mergers will be accompanied by electromagnetic counterparts from these various jet structures. By making some simple assumptions about the energetic structure of a jet outside of a bright core region, the various temporal features that result from a given jet structure can be predicted. Where the population of merger jets is dominated by a single structure model, I show the expected fractions of optical counterparts brighter than $m_{AB} = 21$.

On 17 August 2017, the Light Interferometer Gravitational Wave Observatory (LIGO) in collaboration with *Virgo* detected the merger of a binary neutron star system. Various electromagnetic counterparts were detected: the GRB 170817A by *Fermi*/GBM and INTEGRAL; an optical, blue to red, macro/kilo-nova from $\sim 1/2$ day post merger to $\sim 5 - 10$ days; and a brightening radio, and X-ray counterpart from ~ 10 days. Optical detection of this counterpart at a magnitude ~ 26 was made at ~ 100 days post-merger. Analysis of this counterpart is consistent with the afterglow of a Gaussian structured jet viewed at the system inclination, $\sim 18 \pm 8°$.

If all short GRB jets have a similar jet structure, then the rates of orphan afterglows in deep drilling blind surveys e.g. the Large Synoptic Survey Telescope (LSST), will be higher than those expected from a homogeneous, or 'top-hat' jet, population. The rates for the various jet structures for orphan afterglows from mergers is discussed, showing that for a population of failed GRBs, or an intrinsic Gaussian structure, an excess in the orphan rate may be apparent.

Understanding the dynamics and structure for the jets from black-hole systems born at the merger of a compact binary can help give clues as to the nature of jets

from black holes on all scales. As an aside, I show empirically that regardless of black hole mass or system phenomenology, the relativistic jets from such systems share a universal scaling for the jet power and emitted γ-ray luminosity. This scaling could be due to the similar efficiencies of various processes, or alternatively, the scaling may be able to give insights into the emission and physical processes that are responsible for high-energy photons from these outflows.

GW astronomy offers a probe of the most extreme relativistic outflows in the Universe, GRBs. The predicted electromagnetic counterparts from these outflows, in association with GW detections, provides a way to probe the Lorentz-factor distribution for merger-jets. Additionally, the phenomenological shape of the afterglows, at various inclinations, gives an indication of the intrinsic structure of these jets. An understanding of these dynamical and structural qualities can be used to constrain the parent population, merger rates, and binary evolution models for compact binary systems.

"Amoebas don't make motorcycles and atomic bombs!" [sic] - Kei

<div align="right">

(Popular misquotation) Akira by Katsuhiro Otomo, 1988

</div>

"I am the Nightrider. I'm a fuel injected suicide machine. I am the rocker, I am the roller, I am the out-of-controller!" - Nightrider

<div align="right">

Mad Max by George Miller, 1979

</div>

"If you didn't do anything that wasn't good for you it would be a very dull life. What are you gonna do? Everything that is pleasant in life is dangerous." - Lemmy (RIP)

<div align="right">

Interview with Fiona Sturges, 2005

</div>

Acknowledgements

Publications

Refereed Articles

Lyman, J., **Lamb, G. P.**, Levan, A. J. et al., "*The optical afterglow of the short gamma-ray burst associated with GW 170817*", 2018, (submitted to Nature Astronomy).

Lamb, G. P., Tanaka, M. & Kobayashi, S., "*Transient Survey Rates for Orphan Afterglows from Compact Merger Jets*", 2018, MNRAS,

Boyajian, T. S., Alonso, R., Ammerman, A., et al., "*The First Post-Kepler Brightness Dips of KIC 8462852*", 2018, ApJL, 853, L8.

Lamb, G. P. & Kobayashi, S., "*GRB 170817A as a Jet Counterpart to Gravitational Wave Trigger GW 170817*", 2017, (submitted to MNRAS).

Steele, I. A, Copperwheat, C. M., Jermak, H. E., Kennedy, G. M., & **Lamb, G. P.**, "*Optical Polarimetry of KIC 8462852 in May-August 2017*", 2018, MNRAS, 473, L26.

Lamb, G. P. & Kobayashi, S., "*Electromagnetic Counterparts to Structured Jets from Gravitational Wave Detected Mergers*", 2017, MNRAS, 472, 4953.

Lamb, G. P., Kobayashi, S., & Pian, E., "*Extending the 'energetic scaling of relativistic jets from black hole systems' to include γ-ray loud X-ray binaries*", 2017, MNRAS, 472, 475.

Copperwheat, C. M., Steele, I. A., Piascik, A. S., et al., "*Liverpool Telescope follow-up of candidate electromagnetic counterparts during the first run of Advanced LIGO*", 2016, MNRAS, 462, 3528-3536.

Lamb, G. P. & Kobayashi, S., "*Low-Γ Jets from Compact Stellar Mergers: Candidate Electromagnetic Counterparts to Gravitational Wave Sources*", 2016, ApJ, 829, 112.

Jermak, H., Steele, I. A., Lindfors, E., et al., "*The RINGO2 and DIPOL optical polarization catalogue of blazars*", 2016, MNRAS, 462, 4267-4299.

Kopač, D., Mundell, C. G., Japelj, J., et al., "*Limits on Optical Polarization during the Prompt Phase of GRB 140430A*", 2015, ApJ, 813, 1.

Conference Proceedings etc.

Lamb, G. P. & Kobayashi, S., "*Revealing short GRB jet structure and dynamics with Gravitational Wave Electromagnetic Counterparts*", 2018, Proceedings of IAU Symposium 338 (Gravitational Wave Atsrophysics: Early Results from GW Searches and Electromagnetic Counterparts).

Lamb, G. P. & Kobayashi, S., "*Low-Γ Jets from Compact Binary Mergers as Can-*

didate Electromagnetic Counterparts to Gravitational Wave Sources", 2017, Proceedings of IAU Symposium 324 (New Frontiers in Black Hole Astrophysics), 324, 66.

Jermak, H., Steele, I. A., **Lamb, G. P.**, Valtonen, M., & Zola, S., "*Observations of possible jet formation in the binary blazar OJ287*", 2017, Proceedings of IAU Symposium 324 (New Frontiers in Black Hole Astrophysics), 324, 241

Jermak, H., Steele, I., Lindfors, E., et al., "*Ringo2 Optical Polarimetry of Blazars*", 2016, Galaxies, 4, 52.

Lamb, G. P., & Kobayashi, S., "*On and Off Axis Orphan Afterglow from Low Lorentz Factor Jets - Candidate Electromagnetic Counterparts to Gravitational Wave Sources*", 2016, Eighth Huntsville Gamma-Ray Burst Symposium, 1962, 4015

Steele, I. A., **Lamb, G. P.**, Copperwheat, C. M., & Jermak, H. E., "*Medium Resolution Spectroscopy of Boyajian's Star (KIC 8462852)*", 2017, The Astronomer's Telegram, 406.

Contents

6   An aside - Energetic Scaling of Black Hole Jets   144

7   Conclusions and Future Work   164

List of Figures

List of Tables

1. Introduction

Astrophysical jets are seen on all scales, from Active Galactic Nuclei where the central object is a supermassive black hole to the jets from young stars that form Herbig-Haro objects. For the relativistic jets from black holes, from supermassive to stellar mass alike, the precise nature of the formation and acceleration processes are unknown but the underlying physics is thought to be similar. Gravitational wave observed compact binary mergers give an opportunity to probe the dynamics and structure of the ultra-relativistic jets that produce short gamma-ray bursts. Understanding the dynamics and structure of these jets will provide clues to the physical processes responsible for these ultra-relativistic collimated outflows.

1.1   Gamma-Ray Bursts

Gamma-Ray Bursts (GRBs) are enigmatic bright flashes of high energy photons that were first discovered by the *Vela* satellites on 2 July 1967. Subsequent observations from July 1969 to July 1972 resulted in sixteen detected GRBs in the energy range 0.2-1.5 MeV; these were the first published GRBs (Klebesadel et al., 1973).

For the next ~ 25 years the origin of GRBs was fiercely debated (e.g. see Fishman & Meegan, 1995). By 1993 there were $\gtrsim 100$ published GRB theory models (Nemiroff, 1994), and by late 1990 the majority consensus was for a Galactic disk

neutron star progenitor origin. However, the launch in 1991 of the *Compton* Gamma Ray Observatory (CGRO), with an instrument designed for the detection of GRBs, the Burst and Transient Source Experiment (BATSE), resulted in a challenge to this consensus. The BATSE GRB sample was distributed isotropically but not homogeneously, this favoured a cosmological origin for GRBs (Meegan et al., 1992).

A cosmological origin for GRBs meant that the events were instantaneously the most luminous electromagnetic sources in the Universe, and very rare (Piran, 1999; Kumar & Zhang, 2015). However, there was a problem with the cosmological origin for GRBs. This problem was in how to explain the apparent compactness of the sources. The observed sub-second variability, δt, of the γ-ray light-curves imply compact sources, and the high-energy and non-thermal photons imply the emission region is optically thin, $\tau \leq 1$. By considering the inferred size and the opacity due to pair-production of the emitting region, plus the cosmological distance D_L, the source should have a high opacity, $\tau \propto F D_L^2 \delta t^{-2}$, here F is the observed fluence (Ruderman, 1975; Schmidt, 1978).

The solution to the compactness problem lies in understanding the relativistic motion of the source. If the source of the radiation is moving towards an observer at a relativistic velocity, then the size of the emitting region is larger by a factor Γ^2 than the size inferred by the minimum variability timescale, $\sim c\delta t$; here Γ is the Lorentz factor of the source towards the observer, and c is the speed of light. The optical depth of the emitting region is a factor $\Gamma^{-2\alpha}$ smaller, where α is the high-energy photon spectral index. Estimates for the required Lorentz-factor from these conditions indicate a typical value of $\Gamma \sim 100$ (Fenimore et al., 1993; Woods & Loeb, 1995).

The duration of GRBs observed by BATSE revealed a bimodal distribution (Kouveliotou et al., 1993; Lamb et al., 1993; Mao et al., 1994). Using the duration called T_{90} within which the cumulative counts increase from 5% to 95%, giving a timescale

for 90% of the energy, the two distributions of GRBs were clearly shown. These two distributions have been classed as: short GRBs where $T_{90} < 2$ s; and long GRBs where $T_{90} > 2$ s. Kouveliotou et al. (1993) also showed that short GRBs have a higher average hardness than long GRBs. Here hardness was defined by the ratio of the counts in the 100-300 keV energy band to the 50-100 keV energy band.

The variability timescale of GRBs can also imply that the emission region is most likely internal to the outflow i.e. the internal shock model (Meszaros & Rees, 1993; Kobayashi et al., 1997; Sari & Piran, 1997; Daigne & Mochkovitch, 1998). The high energy and ultrarelativistic velocity of the outflow that produces GRBs via some internal dissipation process will eventually interact with the interstellar medium. This interaction will produce external shocks that radiate via the synchrotron process and give rise to an observable afterglow (e.g. Paczynski & Rhoads, 1993; Katz, 1994a,b; Mészáros & Rees, 1997; Sari et al., 1998).

The first afterglow detection was made by the X-ray telescope, Beppo-SAX, following GRB 970228. The X-ray afterglow contained a significant fraction of the total GRB energy and faded from detection with a power-law decay function (Costa et al., 1997). The position determined by the Wide Field Camera on Beppo-SAX enabled the identification of an optical afterglow at an I-band magnitude 20.6 and V-band magnitude 21.3 by the William Herschel Telescope on La Palma (van Paradijs et al., 1997). Confirmation of the cosmological distance for GRBs came via spectroscopy of an optical counterpart to GRB 970508. Here, prominent absorption lines indicated an absorption system along the line-of-sight at a redshift $z = 0.835$ (Metzger et al., 1997). A radio afterglow for GRB 970508 was also observed by the Very Large Array (VLA) at 1.43 GHz (Frail et al., 1997).

For some well sampled afterglows, a steepening in the decline of the optical and X-ray afterglow is observed (e.g. Harrison et al., 1999). This steepening decline was

predicted by Rhoads (1999) as an observable feature for a collimated outflow, or a jet. As the outflow decelerates, the relativistic beaming angle of the emission, described by the inverse of the instantaneous bulk Lorentz factor, widens. When this value is equal to the angle that describes the collimated outflow, a distant observer will begin to see the edge of the jet, and the observed flux at all frequencies will decrease, the temporal index reducing by $3/4$ from the pre-break decline (Panaitescu & Mészáros, 1999). Alternatively, the jet may start to expand laterally and this sideways expansion will result in a post-break temporal decline with an index equal to the blast wave electron energy distribution (Rhoads, 1999; Sari et al., 1999; Panaitescu et al., 1998).

Long duration GRBs are now known to be associated with the core-collapse of massive stars. The first supernova (SN) - GRB association was found with SN 1998bw, a very luminous type Ic supernova, and GRB 980425, a low-luminosity long duration GRB (Galama et al., 1998). Initial GRB-SNe had GRB luminosities significantly below that typical for long GRBs. However, a SNe-like rebrightening or bump in the optical afterglow at ~ 10 days has also been observed as well as SNe association with higher-luminosity GRBs. The current number of spectroscopically confirmed GRB-SNe is seventeen (as of 18/12/17), plus two X-ray flash (XRF) SNe; e.g. 2001ke/GRB 011121 (Bloom et al., 2002), 2003dh/GRB 030329 (Hjorth et al., 2003; Stanek et al., 2003; Mazzali et al., 2003), 2003lw/GRB 031203 (Malesani et al., 2004), 2005nc/GRB 050525A (Della Valle et al., 2006a), 2006aj/XRF 060218 (Modjaz et al., 2006; Campana et al., 2006; Pian et al., 2006), 2008hw/GRB 081007 (Olivares E. et al., 2015), 2009nz/GRB 091127 (Olivares E. et al., 2015), 2010bh/XRF 100316D (Starling et al., 2011), 2010ma/GRB 101219B (Sparre et al., 2011; Olivares E. et al., 2015), 2011kl/GRB 111209A (Greiner et al., 2015), 2012bz/GRB 120422A (Melandri et al., 2012), 2013ez/GRB 130215A (Cano et al., 2014), 2013cq/GRB 130427A (Levan et al., 2014; Melandri et al., 2014), 2013dx/GRB 130702A (D'Elia et al.,

2015), 2013fu/GRB 130831A (Cano et al., 2014), 2016jca/GRB 161219B (Ashall et al., 2017), and 2017iuk/GRB 171205A. There are a further fourteen GRB/XRF-SNe, but without spectroscopic confirmation. Afterglow from long GRBs can also be consistent with a shockwave propagating through a wind medium. Such a medium is expected from a massive star progenitor (Chevalier & Li, 2000; Panaitescu & Kumar, 2000; Gou et al., 2001; Perley et al., 2014).

The progenitor for short GRBs would prove to be more elusive. Optical and radio follow-up observations of short GRBs resulted in non-detections (Kehoe et al., 2001; Hurley et al., 2002). However, with the more accurate localization of GRBs made possible by the *Swift* satellite (Gehrels et al., 2004), the hopes of finding a counterpart to a short GRB increased. Rapid X-ray follow-up of GRB 050509B by the *Swift*/X-ray telescope (XRT) led to the discovery of an X-ray counterpart and the short GRB's association with a massive elliptical galaxy at redshift, $z = 0.225$ (Gehrels et al., 2005; Castro-Tirado et al., 2005; Bloom et al., 2006).

GRB 050509B was followed by the HETE-2 (Ricker et al., 2003) detected GRB 050709 (Villasenor et al., 2005). Follow-up by *Chandra* X-ray observatory localized the X-ray afterglow to the outer regions of a star forming galaxy at $z = 0.160$ (Fox et al., 2005), and led to the first optical afterglow for a short GRB (Hjorth et al., 2005b). Soon after, *Swift* detected the GRB 050724 (Barthelmy et al., 2005) which was localised to an elliptical galaxy at $z = 0.257$ with X-ray, optical/near-infra-red (IR), and radio afterglow (Berger et al., 2005). These observations secured the cosmological origin for short GRBs, and demonstrated that they were not associated with the core-collapse of massive stars (Hjorth et al., 2005a,b).

A non-core-collapse progenitor for short GRBs pointed to compact binary mergers involving neutron stars or a neutron star and a black hole as the most likely candidate for the progenitor system (e.g. Paczynski, 1986, 1991; Popham et al., 1999). The

merger of such a binary system was proposed by Li & Paczyński (1998) to result in an isotropic transient that would peak hours to days after the merger at optical frequencies. This transient is powered by the radioactive decay of the disrupted neutron star matter ejected during the merger; this ejected material forms heavy elements resulting in an abundance estimate that is roughly comparable to the observed Solar-system r-process material (Lattimer & Schramm, 1974; Lattimer et al., 1977). These transients have been termed 'macronovae' (Kulkarni, 2005) or 'kilonovae' (Metzger et al., 2010) (and 'mergernovae' (Gao et al., 2015), amongst others). If short GRBs are from compact binary mergers, then a bump or feature in the afterglow at red optical/IR frequencies a few days post-burst will be apparent where conditions are favourable.

GRB 130613B, a short GRB with a duration $T_{90} = 0.18$ s at a redshift $z = 0.356$, had an excess in the near-IR afterglow at ~ 7 days revealed by Hubble Space Telescope (HST) observations (Tanvir et al., 2013; Berger et al., 2013). The excess is consistent with that from a radioactively powered macro/kilo-nova following the merger of two neutron stars (Rosswog, 2013; Tanaka & Hotokezaka, 2013; Hotokezaka et al., 2013a). Excess of emission at IR frequencies has also been claimed for several other short GRBs; most notable are GRB 050709 (Jin et al., 2016) and GRB 080503 (Gao et al., 2015), plus the long-short[1] GRB 060614 (Jin et al., 2015).

Short GRBs are typically less energetic than long GRBs, and due to the natal kicks that a compact-binary system may receive (Bray & Eldridge, 2016), the location within the host galaxy can have a low density, these result in a fainter afterglow (Berger, 2014). However, not all long GRBs have a massive star association and not all short GRBs have a compact merger progenitor. The nearby long GRBs 060614 and 060605 both lack an accompanying SN (Gehrels et al., 2006; Gal-Yam et al., 2006;

---

[1] This GRB has a long total duration - however, the prompt emission contains an initial bright flash of duration 0.32 ± 0.07 s, followed by a soft extended emission lasting 232 s. The short spike is a factor ~ 30 brighter than the extended emission, and the hardness ratio and spectral lag are more consistent with the GRB having a compact merger origin (Perley et al., 2009)

Fynbo et al., 2006; Della Valle et al., 2006b) where SNe should have been observed. This suggests that some long GRBs may have a compact merger progenitor. Alternatively, the observed population of short GRBs can be significantly contaminated by GRBs with a massive star progenitor (e.g. Virgili et al., 2011b; Bromberg et al., 2013). Bromberg et al. (2013) claim $\sim 40\%$ of *Swift* short GRBs could arise from the collapse of massive stars. GRBs with a high redshift and a rest-frame duration of < 2 s are all argued to have a massive star progenitor (Zhang et al., 2009). Equally, the short GRB 090426 at a redshift $z = 2.61$ has spectral and energetic properties that make this burst consistent with the population of long GRBs (Antonelli et al., 2009).

GRBs that have a massive star SN origin, typically long GRBs, will have a rate that follows the star formation history. However, at high-redshift, $z > 4$, the observed GRBs may indicate an excess in the high-z GRB rate above that predicted by star formation history (e.g. Kistler et al., 2008; Li, 2008; Qin et al., 2010; Virgili et al., 2011a; Robertson & Ellis, 2012). It is possible that these high-z GRBs could trace low-luminosity star-forming galaxies that have been missed by galaxy surveys (Sun et al., 2015).

For GRBs with a compact merger origin, the rate is likely to be delayed by some function from the star-formation history (Piran, 1992). The creation of the binary system will trace star-formation, however the additional time required to inspiral and eventually merge results in a delay. The final inspiral of the binary components is due to gravitational wave radiation (Peters & Mathews, 1963) but a typical merger delay timescale for compact binary systems is not known. However a functional form for the delay can be assumed and parameters derived from the best fit to data (e.g. Guetta & Piran, 2006; Virgili et al., 2011b; D'Avanzo et al., 2014; Wanderman & Piran, 2015; Sun et al., 2015; Ghirlanda et al., 2016; Paul, 2017). The leading time-delay models are either a power-law time-delay, a constant time-delay, or a lognormal

time-delay. The latter is favoured by Wanderman & Piran (2015); this lognormal time-delay results in a short GRB population from compact binary mergers that peaks at $z \sim 0.9$, with an exponential decay to higher redshifts. The detection of a host for the non-collapsar short GRB 111117A at $z = 2.211$ has been claimed to challenge the lognormal delay (Selsing et al., 2017). However, the probability of a short GRB at this redshift is ~ 2 orders lower than for at the lognormal peak redshift and still within the expected probability distribution. Constant or power-law time-delay distributions typically predict a peak rate at $z \sim 1.5 - 2$, and such a distribution would result in a high fraction of undetected short GRBs. Approximately 30% of short GRBs have a redshift measurement, with the median measured redshift being $\langle z \rangle = 0.5$ (Berger, 2014; Fong et al., 2015). The local short GRB rate estimates from each of the various time-delay models are usually similar, $\sim 3 - 8$ Gpc^{-3} yr^{-1} (e.g. Sun et al., 2015), however Ghirlanda et al. (2016) and Madau & Dickinson (2014) have suggested a local rate approximately an order of magnitude smaller.

1.2 Calculating the Afterglow from a Relativistic Fireball

GRBs are used as a trigger for the search and detection of a broadband afterglow. Afterglow localisation helps in identifying the host galaxy of the GRB. By identifying the host galaxy, and/or the afterglow itself, a redshift for the burst can be determined.

The afterglow can reveal additional properties of the GRB. This requires the fitting of afterglow models to observations. A GRB afterglow can typically be described by the standard fireball model (e.g. Rees & Meszaros, 1992; Paczynski & Rhoads, 1993; Piran et al., 1993).

Analytically the emission from the external shock of a decelerating fireball can be

estimated by considering conservation of energy. The fireball, or outflow, will begin decelerating when the swept up mass is equal to M/Γ, here M is the initial rest mass of the fireball and Γ the bulk Lorentz factor (Sari & Piran, 1995). The deceleration radius is $R_{\text{dec}} \propto (E/\Gamma^2 n)^{1/3}$, where E is the fireball energy and n is the ambient (external) medium particle number density.

The particle number and energy density behind the shock can be described by $4\Gamma n$ and $4\Gamma^2 n m_p c^2$ respectively (Blandford & McKee, 1976), where n is the ambient medium particle number density, m_p is the mass of a proton, and c the speed of light. The shock will accelerate electrons to relativistic velocities and these relativistic electrons emit synchrotron radiation in the magnetic field that is either carried from the central engine of the GRB or generated in the shocks (Piran, 2005).

The accelerated electrons are assumed to follow a power-law distribution of index p. The electron distribution is then $N_e \mathrm{d}\gamma \propto \gamma^{-p} \mathrm{d}\gamma$, where N_e is the total number of electrons. A fraction of the internal energy density goes into the accelerated electrons as

$$\varepsilon_e 4\Gamma^2 n m_p c^2 = \int_{\gamma_m}^{\infty} \gamma m_e c^2 N_e \mathrm{d}\gamma, \tag{1.1}$$

where the parameter ε_e is the fraction of the shock energy that goes into the electrons, m_e the mass of an electron, γ is the particle Lorentz factor, and γ_m the minimum particle Lorentz factor. By assuming charge neutrality the number of protons is equal to the number of electons. So the number density of protons or electrons behind the shock is

$$4\Gamma n = \int_{\gamma_m}^{\infty} N_e \mathrm{d}\gamma. \tag{1.2}$$

Substituting equation 1.2 into equation 1.1 gives an expression for the energy in the

relativistic electrons

$$\varepsilon_e \Gamma \int_{\gamma_m}^{\infty} m_p c^2 \gamma^{-p} \mathrm{d}\gamma = \int_{\gamma_m}^{\infty} m_e c^2 \gamma^{1-p} \mathrm{d}\gamma, \tag{1.3}$$

here the left side is the fraction of the shock energy density that goes into the electrons and the right side is the electron energy density. The minimum electron Lorentz factor is then

$$\gamma_m = \varepsilon_e \Gamma \frac{(p-2)}{(p-1)} \frac{m_p}{m_e}. \tag{1.4}$$

Similarly for the magnetic field, a fraction of the shock energy is converted into magnetic field strength

$$\varepsilon_B 4 \Gamma^2 n m_p c^2 = \frac{B^2}{8\pi}, \tag{1.5}$$

where the left side the fraction of the shock energy density, and the right side is the magnetic energy density. The variable ε_B is the fraction of energy that goes into the magnetic field.

The power radiated by a relativistic electron is given by Rybicki & Lightman (1979) as

$$P(\gamma) = \frac{4}{3} \sigma_T c \gamma^2 \beta^2 \frac{B^2}{8\pi} \Gamma^2, \tag{1.6}$$

where σ_T is the Thomson cross-section, $\beta^2 = 1 - \gamma^{-2}$, and the additional Γ^2 is introduced following Sari et al. (1998) to correct the emission for the observer frame.

The observed frequency of the synchrotron emission is

$$\nu(\gamma) = \Gamma \gamma^2 \frac{q_e B}{2\pi m_e c^2}, \tag{1.7}$$

where q_e is the electron charge. The minimum particle Lorentz factor will define the characteristic synchrotron frequency, or the peak of the spectrum. Substituting γ_m

from equation 1.4 for γ in equation 1.7 will give the characteristic frequency, ν_m.

Another critical frequency defines the point at which an electron will lose energy efficiently via the synchrotron process, when $\Gamma\gamma m_e c^2 = P(\gamma)t$, here t is the time in the observer frame. Then using equation 1.6 and rearranging for γ gives

$$\gamma_c = \frac{3m_e}{16\varepsilon_B \sigma_T n m_p c \Gamma^3 t}.$$

(1.8)

Using this particle Lorentz factor in equation 1.7 will give the cooling frequency, ν_c.

If $\gamma_m > \gamma_c$ then the electrons will cool quickly via synchrotron radiation, this is the case of 'fast cooling'. If $\gamma_m < \gamma_c$ then only the fraction of the electron distrubution with $\gamma > \gamma_c$ will cool efficiently, this case is called 'slow cooling'. The flux at a given frequency for each of these conditions was given by Sari et al. (1998). The maximum synchrotron flux, $F_{\max}$ is found by the product of the number of electrons $N_e = 4\pi n R^3/3$, the maximum power $P_{\max} = P(\gamma)/\nu(\gamma)$, and the surface defined by the luminosity distance $1/(4\pi D_L^2)$ where D_L is the luminosity distance. Then the flux at a given frequency is

'fast cooling'

$$F_\nu = \begin{cases} (\nu/\nu_c)^{1/3} F_{\max}, & \nu_c > \nu \\ (\nu/\nu_c)^{-1/2} F_{\max}, & \nu_m > \nu > \nu_c \\ (\nu_m/\nu_c)^{-1/2} (\nu/\nu_m)^{-p/2} F_{\max}, & \nu > \nu_m \end{cases}$$

(1.9)

'slow cooling'

$$F_\nu = \begin{cases} (\nu/\nu_m)^{1/3} F_{\max}, & \nu_m > \nu \\ (\nu/\nu_m)^{-(p-1)/2} F_{\max}, & \nu_c > \nu > \nu_m \\ (\nu_c/\nu_m)^{-(p-1)/2} (\nu/\nu_c)^{-p/2} F_{\max}, & \nu > \nu_c \end{cases}$$

(1.10)

The evolution of the flux with time depends on how these various quantities evolve. In the observer frame the point at which the outflow will begin deceleration is $t = R/(\kappa\Gamma^2 c)$, where $2 \leq \kappa \leq 16$ depending on the details of the hydrodynamic evolution (e.g. Blandford & McKee, 1976; Sari, 1997, 1998; Panaitescu et al., 1998; Rhoads, 1999).

After the deceleration time, the bulk Lorentz factor of the outflow evolves as $\Gamma \propto t^{-8/3}$. The characteristic and cooling frequency will then evolve with time as, $\nu_m \propto t^{-3/2}$ and $\nu_c \propto t^{-1/2}$, provided the jet does not start to expand sideways. The flux at times later than the deceleration time will evolve as $F_\nu \propto t^{3(p-1)/4}$ where $\nu < \nu_c$, and $F_\nu \propto t^{(3p-2)/4}$ where $\nu_c < \nu$. At lower frequencies, where $\nu < \nu_m$ then the flux evolves as $F_\nu \propto t^{1/2}$ (Sari et al., 1998, 1999).

1.3 Electromagnetic Emission from a NS/BH-NS merger

The inspiral and merger of neutron star (NS-NS) or black hole and neutron star (BH-NS) binary systems is an observational target for gravitational wave (GW) detectors e.g. Light Interferometer Gravitational Wave Observatory (LIGO), *Virgo*, and Kamioka Gravitational Wave Detector (KAGRA) (Abadie et al., 2010; Aso et al., 2013; Abbott et al., 2016a). The sensitivity of these gravitational wave detectors limits the volume within which a compact binary merger can be detected. At full sensitivity, LIGO will be able to detect NS-NS mergers out to a distance of ~ 300 Mpc, and BH-NS mergers to ~ 600 Mpc (Nissanke et al., 2013; Abbott et al., 2016a). These volumes are considered to be local in terms of cosmological distance, $z \lesssim 0.1$. Due to the poor sky-localization of GW detectors (Abbott et al., 2016a), an electromagnetic (EM) counterpart is required to pin-point their origin. The observation of EM counterparts to GW detected mergers will maximise the science returns from GW astronomy.
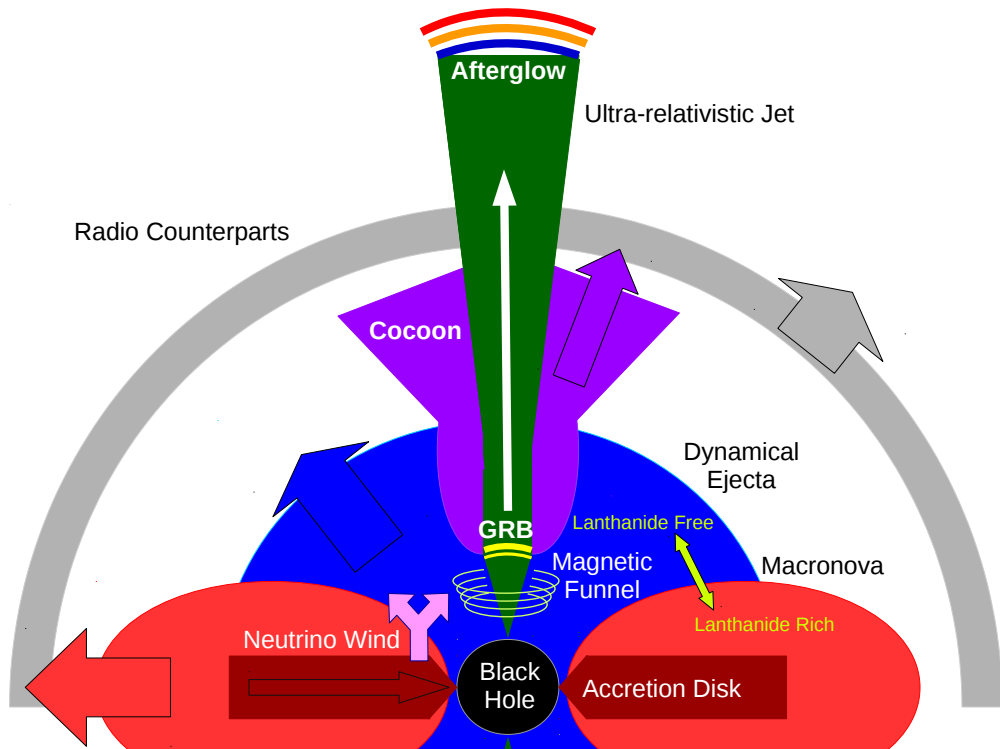
Figure 1.1: Cartoon showing the expected electromagnetic counterparts from a compact binary merger system. Bi-polar relativistic jets are formed within a magnetic funnel, while the jet may be accelerated by neutrino winds from an accretion disk. Interaction between the jet and any post-merger material may form a cocoon that can help collimate the outflow; this heated cocoon may produce an observable counterpart to favourably inclined systems. Internal shocks produce a GRB. At late times the jet decelerates in the ambient medium due to external shocks that result in an afterglow. The radio-active decay of heavy elements formed via the r-process within the dynamical ejecta produces an isotropic macronova. Depending on the neutron star equation of state, two or three components may exist; a lanthanide-free region near to the rotation axis that results in an early blue macro/kilo-nova, and a more equatorial component that produces many lanthanides resulting in a high opacity and a red, and later kilo-nova. At very late times, the dynamic ejecta will decelerate in the ambient medium resulting in an isotropic radio counterpart.

Interest in the potential EM counterparts to NS mergers has resulted in a number of scenarios to be considered, see Figure 1.1. The most commonly discussed counterparts include: short GRBs (Ghirlanda et al., 2016; Kathirgamaraju et al., 2018; Jin et al., 2017) and their afterglow (Coward et al., 2014); failed GRB afterglow (Lamb & Kobayashi, 2016); off-axis orphan afterglow (Zhang, 2013; Lamb & Kobayashi, 2017a; Lazzati et al., 2017a; Sun et al., 2017); the macro/kilo-nova (Barnes & Kasen, 2013; Tanaka & Hotokezaka, 2013; Piran et al., 2013; Metzger & Fernández, 2014; Tanaka et al., 2014, 2018; Barnes et al., 2016; Tanaka, 2016; Metzger, 2017a); radio counterparts (Nakar & Piran, 2011; Kyutoku et al., 2014; Hotokezaka & Piran, 2015; Margalit & Piran, 2015; Hotokezaka et al., 2016); cocoon emission (Kisaka et al., 2017; Lazzati et al., 2017b; Nakar & Piran, 2017; Gottlieb et al., 2018); and precursor or merger flares (Tsang et al., 2012; Kyutoku et al., 2014; Metzger & Zivancev, 2016).

1.3.1 Precursor or Merger Flares

Precursors to short GRBs have been observed for a small number of events, $\sim 8 - 10\%$ (e.g. Abdo et al., 2009; Troja et al., 2010). These precursors occur $1 - 10$ s before the GRB, when the NSs are strongly interacting. The origin of these precursors could be magnetospheric (e.g. Hansen & Lyutikov, 2001), although this would require magnetic field strengths exceeding those of magnetars (Tsang et al., 2012). As tidal deformation exceeds the breaking strain the NS crust will crack, and such a cracking could account for these precursors (Kochanek, 1992; Penner et al., 2011) although this requires the GRB emission time to be delayed by a few seconds after merger. Alternatively, the tidal mechanism can shatter the crust causing flares. This shattering is achieved by the excitation of a resonant mode due to a periodic tidal deformation (Tsang et al., 2012).

Kyutoku et al. (2014) proposed that a shock wave produced at a NS-NS collision, propagating from the heated NS core to the crust, would become ultra-relativistic at

the shock breakout from the surface. The ejected material will expand into the surrounding ambient density, where the relativistic ejecta will be decelerated resulting in synchrotron radiation. These merger-flares will be nearly isotropic with X-ray emission peaking a few ms after the merger.

If at least one of the NSs is magnetized then a pair-fireball could be created by magnetospheric interaction between NSs (Metzger & Zivancev, 2016). Such a pair-fireball occurs when the temperature of a radiation or photon fireball is high enough that electron-positron pairs are formed, these pairs increase the fireball opacity trapping the photons and resulting in a coupled photon-pair plasma which behaves as a perfect fluid. This fireball will result in nearly isotropic, quasi-thermal, hard X-ray or γ-ray emission similar to a subluminous short GRB. Such a mechanism may also lead to non-thermal radio flares, or fast radio bursts, as power not dissipated close to the binary is carried along open-field lines where reconnection occurs above the pair photosphere.

1.3.2 Jets

The ultra-relativistic collimated outflow, or jet, that gives rise to GRBs is thought to be formed in a similar way to the jets observed from other BH systems i.e. active galactic nuclei (AGN), or X-ray binaries (XRB). The details of the exact formation and acceleration mechanism are not clear; however rapid accretion, magnetic fields, and neutrinos are thought to play a role. The BH spin can generate jets via the BZ process described by Blandford & Znajek (1977), such a jet will be lepton dominated. Alternatively, a jet can be launched via the BP process decribed by Blandford & Payne (1982); these jets are formed via the co-rotation of a frozen-in magnetic field within an accretion disk and will be baryon dominated. The jets generated by either of these processes will be bipolar and extract angular momentum from either the BH or the disk. Where an accretion disk becomes sufficiently hot, neutrino cooling can play

an important role in the acceleration of a jet, and such a disk is called a neutrino-dominated accretion flow (NDAF) (Popham et al., 1999). Accreting BH systems as the central engine for GRBs have been extensively investigated (e.g. Popham et al., 1999; Lee et al., 2000; Li, 2000; Narayan et al., 2001; Kohri & Mineshige, 2002; Wang et al., 2002; McKinney, 2005; Gu et al., 2006; Chen & Beloborodov, 2007; Janiuk et al., 2007; Lei et al., 2009). The efficiency of baryon-loading for these jets by a neutrino wind can affect the jet's bulk Lorentz factor (Lei et al., 2013).

Due to the ultra-relativistic motion, the emission from these bipolar jets is highly beamed. The bipolar jets from a NS merger are defined by a half-opening angle θ_j, and the emission is beamed within an angle Γ^{-1}; for an observer at an inclination $i > \theta_j + \Gamma^{-1} \sim \theta_j$ (as typically $\Gamma^{-1} << \theta_j$), the jet emission will be undetectable at the usual cosmological distances. The probability that a merging system is inclined towards an observer is $f_b = 1 - \cos\theta_j \sim \theta_j^2/2$. For short GRBs the typical value of θ_j is poorly constrained, where estimates of the jet half-opening angle from the achromatic break in the afterglow light curve indicate angles over a broad range. The narrowest short GRB jets have $\theta_j \sim 2°$ while a non-detection of the break at a time equivalent to $\theta_j \sim 25°$ places a lower limit on the widest jet angles; the mean from the short GRB population, where an upper-limit of $33°$ is assumed, is $\sim 16 \pm 10°$ (Fong et al., 2015). Using a Markov Chain Monte Carlo analysis of the observed population of short GRBs, Ghirlanda et al. (2016) found the typical short GRB opening angle to be narrower, at $\theta_j \sim 6°$. However measurement of θ_j from the jet-break time assumes that the observer is on the jet central axis, for an observer at any inclination between the central axis and the jet edge the break time will be set by the jet edge furthest from the observer (van Eerten et al., 2010; van Eerten & MacFadyen, 2012).

The observed afterglow from a GRB is modelled assuming a homogeneous jet where the energy per steradian is constant until the jet edge where it sharply drops

(Granot, 2007). Various structured jet models have been proposed, some in an attempt to explain the diversity of GRBs as a universal structured jet viewed at different inclinations (e.g Lipunov et al., 2001; Rossi et al., 2002; Zhang & Mészáros, 2002). The universal structured jet model takes the form of a power-law distribution of energy or other parameter, typically Γ, with angle θ from the jet central axis or a narrow jet core. Other jet structures considered include a two-component, or spine and sheath jet, where a uniform core is surrounded by a sheath with lower energy and Γ (Pedersen et al., 1998; Frail et al., 2000; Berger et al., 2003; Huang et al., 2004; Peng et al., 2005; Wu et al., 2005); and Gaussian structured jets, where the parameters are described by a Gaussian function with angle (Kumar & Granot, 2003; Rossi et al., 2004; Zhang et al., 2004; Lamb et al., 2005; Granot, 2007; Salafia et al., 2015). More exotic structured jet models have also been proposed including a fan shaped jet structure (e.g. Granot, 2007; Barkov & Pozanenko, 2011), and a set of sub-jets within a wider jet cone (Toma et al., 2006). The sub-jet model can be used to explain a shallow decay phase seen during the early X-ray afterglow, whereas the other jet structure models have temporal afterglow light curve characteristics that become apparent for a system viewed at a higher inclination or for off-axis orphan afterglows.

If the jet from a NS merger has to propagate through the merger ejecta, then as the jet drills through this medium a cocoon of shocked material will form (Bromberg et al., 2011). This cocoon will collimate the jet until such a time as the jet breaks out, where the energetic jet core will be surrounded by shocked jet and cocoon material (Nagakura et al., 2014). This jet-cocoon system will appear as a structured jet to an observer at an inclination equivalent to or greater than the jet-cocoon transition (Lazzati et al., 2017c). Alternatively, the jet may fail to drill through the ejecta, resulting in a choked-jet and an energised cocoon (Gottlieb et al., 2017; Mooley et al., 2018). This energised cocoon will appear as a mildly relativistic wide-angle outflow. The cocoon models, especially

the choked-jet case, require a significant amount of ejecta material in the polar region of the compact merger system. Magnetohydrodynamic simulations of merging NS systems result in a low-density environment at the poles with a magnetic funnel, or proto-jet structure (Dionysopoulou et al., 2015; Ruiz et al., 2016). A cocoon may still form from material accelerated by a neutrino wind, however the density is expected to be much lower than that required to choke a jet (Dessart et al., 2009; Perego et al., 2014).

1.3.3 Merger Ejecta

Dynamic ejecta from the tidal disruption of a NS during the merger process can give rise to more isotropic EM counterparts. The most commonly discussed are the radioactively powered macro/kilo-nova and radio counterparts due to the interaction of the ejecta with the ambient medium.

For a macro/kilo-nova the emission mechanism is similar to that for a Type Ia SN with the exception that the ejected mass is much smaller, $\sim 0.01 M_\odot$, the expansion velocity is higher, $\sim 0.1 - 0.2c$, and the heating source is the radioactive decay energy of r-process nuclei (Tanaka, 2016). Details of the r-process in NS merger ejecta have been modelled by Lippuner & Roberts (2015, 2017). The emission will peak $\lesssim 5$ days post-merger at optical to IR frequencies, and is brightest on the polar axis (Tanaka et al., 2016, 2018; Wollaeger et al., 2017). The diversity of peak macro/kilo-nova emission for an on-axis observer i.e. in association with a short GRB, was investigated by Gompertz et al. (2017) and the possible range for the peak emission was found to cover ~ 5 magnitudes. Significant diversity in the peak brightness, that depends on inclination, NS equation-of-state, and other intrinsic qualities such as the electron fraction, is expected in the range of EM counterparts from radioactive decay of r-process nuclei in the merger ejecta (e.g. Shibata et al., 2017).

At late times, the dynamic ejecta will interact with the ambient medium resulting in radio counterparts (Nakar & Piran, 2011; Hotokezaka et al., 2016). The radio counterparts from the merger ejecta - ambient medium interaction will peak on timescales of a few years and result in a long-lasting radio remnant. These radio counterparts may be observable at distances where the optical or IR emission from a macro/kilo-nova viewed at a wider inclination is not detected (Hotokezaka et al., 2016).

1.4 Gravitational Wave Astrophysics

The merger of binary BH systems has produced the LIGO/*Virgo* detections GW 150914, 151226, 170104, 170814 as well as the $\sim 87\%$ confidence LVT 151012 (Abbott et al., 2016b, 2017a,b). BH-BH mergers are not expected to produce an electromagnetic counterpart, however see Connaughton et al. (2016); Ackermann et al. (2016); Savchenko et al. (2016); Verrecchia et al. (2017); and various scenarios have been suggested (e.g. Loeb, 2016; Perna et al., 2016; Zhang, 2016; Yamazaki et al., 2016).

On 17 August 2017, LIGO/*Virgo* detected the final inspiral and merger of a binary neutron star system at ~ 41 Mpc and an inclination $\lesssim 28°$ (Abbott et al., 2017c,e). Here inclination refers to the angle between the system rotation axis and the line-of-sight; this inclination includes a $180°$ ambiguity between a face-on (clockwise rotation) and a face-off (anti-clockwise) system. GW170817 was face-off (Abbott et al., 2017c). The gravitational wave detection was followed, at ~ 2 s, by a faint GRB (Connaughton et al., 2017; Goldstein et al., 2017b; Savchenko et al., 2017b). The One-Meter, Two-Hemisphere (1M2H) collaboration, using a 1m optical telescope, observed a fading optical transient located in an S0 galaxy, NGC 4993, 10.9 hours after the gravitational wave trigger. Continued observation of the transient showed the light curve and spectral evolution was consistent with rapidly expanding merger ejecta, $\sim 0.2c$

e.g. a macro/kilo-nova (Pian et al., 2017). A slowly rising X-ray and radio counterpart were detected from $\sim 10 - 15$ days post-merger (Hallinan et al., 2017; Troja et al., 2017); these X-ray and radio observations are consistent with either an afterglow viewed off-axis (Murguia-Berthier et al., 2017) or a mildly relativistic cocoon of material (Gottlieb et al., 2017). The continued observation of the radio counterpart over the next ~ 100 days (observations are still on-going), and X-ray observations at ~ 106 days post merger indicate a continued rise of the flux with a temporal index $\sim t^{4/5}$. This shallow rising index was predicted for an off-axis jet with a Gaussian jet structure (e.g. Lamb & Kobayashi, 2017a), see Chapter 3. Alternatively, this shallow rise is also consistent with a jet-cocoon system (Lazzati et al., 2017c), or a choked-jet energised cocoon (Mooley et al., 2018).

1.5 Thesis Outline

Within this thesis I present the diversity of potential electromagnetic counterparts from the relativistic jets of NS/BH-NS mergers. Gravitational wave detected mergers remove the requirement of a GRB trigger for afterglow detection, or the highly intensive survey requirements for the detection of a GRB untriggered afterglow. GW detected mergers can reveal the structure and dynamic qualities of merger jets as the progenitor of short GRBs. In Chapter 2 the investigation into the effect of a power-law Lorentz-factor distribution on merger-jets and the electromagnetic counterparts to failed-GRBs is presented. In Chapter 3 the effect of jet structure on the afterglow light curves of GW detected mergers are given. Chapter 4 relates the results of Chapters 2 and 3 to the NS merger GW 170817. The implication of these dynamic and structured jet models for untriggered optical surveys is shown in Chapter 5. As an aside we discuss the universal scaling of γ-ray luminosity from the relativistic jets of black hole systems regardless

of the mass scale in Chapter 6. In Chapter 7 the conclusions and an overview of future
works are given.

2. Low Γ Jets from Compact Stellar Mergers

This Chapter has been published as Lamb & Kobayashi (2016).

2.1 Introduction

Gamma-ray bursts (GRBs) are instantaneously the most luminous objects in the Universe, produced by the deceleration of ultra-relativistic outflow (Lorentz factors $\Gamma \gtrsim 100$). The core-collapse of massive stars are the progenitors of long GRBs, and the merger of binary compact stellar objects such as neutron stars (NS) and black holes (BH) are the possible progenitors of short GRBs (Woosley & Bloom, 2006; Nakar, 2007; Berger, 2014). In both cases accretion onto a compact object is likely to power the relativistic outflow and the same physical processes are involved. The outflow energy is first dissipated by internal shocks (or another form of internal dissipation) which produces the prompt γ-rays. Later the interaction of the outflow with the ambient medium produces an external shock which expands and produces the subsequent afterglow (e.g. Piran, 2004; Zhang & Mészáros, 2004).

Relativistic motion is an essential ingredient in the GRB model although the exact outflow formation process is not known. Understanding the nature of the outflow, espe-

cially the acceleration, collimation, and energy content is a major focus of international research efforts in the context of GRB and other astrophysical jets. GRB outflows are conventionally assumed to be a baryonic jet (Paczynski, 1986; Shemi & Piran, 1990), although polarization measurements imply that magnetic fields play a role in the jet acceleration (e.g. Steele et al., 2009; Mundell et al., 2013; Götz et al., 2009; Yonetoku et al., 2011). Relativistic outflows and possibly magnetic acceleration are features that GRBs, active galactic nuclei (AGN), and microquasars have in common. Stellar tidal disruption by a massive BH is also likely to produce a relativistic jet (Bloom et al., 2011; Burrows et al., 2011; Levan et al., 2011; Zauderer et al., 2011; Cenko et al., 2012). By studying and comparing the properties of these objects, we could gain an insight into the processes that govern the formation of relativistic jets (e.g. Marscher, 2006a; Nemmen et al., 2012).

In the case of blazars, we can measure apparent superluminal motion (i.e. lower limits of Γ), where reported apparent velocities are as high as $40 - 50c$ for γ-ray bright blazars (Jorstad et al., 2005; Lister et al., 2009; Piner et al., 2012; Liodakis & Pavlidou, 2015). The Lorentz factor for AGN is typically $1 < \Gamma \leq 40$ (e.g. Marscher, 2006a; Saikia et al., 2016) or $1 < \Gamma \leq 50$ (Lister et al., 2009). Blazars with a high Γ overpopulate centimetre-wave surveys of bright flat-spectrum sources because of beaming bias. Alternatively, a volume-limited sample of radio-loud AGN would be dominated by objects with more mundane jets. A power-law distribution of Lorentz factors for AGN can be assumed, $N(\Gamma) \sim \Gamma^{-a}$, where population synthesis studies show that a value of a between 1.5 and 1.75 provides a good match between a synthetic and observed distribution of apparent velocities (Lister & Marscher, 1997; Marscher, 2006b). Recent work indicates a value of $a = 2.1 \pm 0.4$ for blazars (Saikia et al., 2016).

Many observations indicate that GRBs are produced by ultra-relativistic outflows with $\Gamma \gtrsim 100$. However, GRB progenitors might not always eject such a high$-\Gamma$

flow. For example, if the outflow is baryonic, the baryon loading might not always be optimal, resulting in lower Lorentz factors. For an outflow with low Γ, the internal dissipation processes (i.e. γ-ray production) happen when the outflow is still optically thick. Since we are currently discovering GRB events through wide field monitoring of the γ-ray sky (e.g. Swift, Fermi, IPN), a population of low$-\Gamma$ outflows might be undiscovered.

Compact stellar mergers are the most promising targets for ground-based gravitational wave (GW) detectors such as advanced LIGO, Virgo and KAGRA. The merger of a binary BH system produced the advanced LIGO detection GW150914, the first direct observation of GW (Abbott et al., 2016b). EM counterparts to BH-BH mergers are not expected; Fermi Gamma-ray Burst Monitor (GBM) however, claimed a 2.9σ detection of a weak γ-ray burst 0.4 seconds after the GW detection (Connaughton et al., 2016), and if this burst is associated with GW150914 then an electromagnetic (EM) afterglow would also be present (Yamazaki et al., 2016). To maximize the science returns from further GW detections, the identification of an EM counterpart will be crucial. The γ-ray emission from short GRBs are an ideal EM counterpart to NS-NS/NS-BH mergers, and potentially BH-BH mergers. However, they occur relatively rarely within the range of GW detectors (300 Mpc for face-on NS-NS mergers), this is possibly because γ-ray emission is highly collimated, or the mis-match between short GRB peak energies and the Swift detection band can make detection more difficult. Additionally the intrinsic rate of compact object mergers within this volume is relatively low. More isotropic EM components such as macronovae are often discussed to localize a large sample of GW events (e.g. Nakar & Piran, 2011; Metzger & Berger, 2012; Gao et al., 2013; Kisaka et al., 2015a).

In this chapter, we discuss the possibility that a significant fraction of compact stellar mergers result in the production of low$-\Gamma$ jets ($\Gamma \lesssim 100$). If such jets are

common, X-ray, optical, and radio transients, i.e. on-axis orphan afterglows (Dermer et al., 2000; Huang et al., 2002; Nakar & Piran, 2003; Rhoads, 2003; Cenko et al., 2013, 2015), would be more frequent than short GRBs. Such low frequency transients would accompany a good fraction of GW events and they allow for the accurate determination of the sky positions of the GW sources. The time lag between GW signals, where we can assume that the jet launch time t_0 is coincident with the merging time when the GW amplitude becomes maximal, and EM jet emission will enable us to determine the Γ distribution of jets from compact stellar mergers and it will provide another constraint on the acceleration process of relativistic jets. In § 2.2 we discuss the background of relativistic motion in the standard GRB fireball model and the implications for the prompt γ-ray emission. In § 2.3 the case for a population of low Lorentz factor jets is made. § 2.4 details the assumptions and conditions made by the Monte Carlo model plus the numerical results. § 2.5 highlights the implications for GW rates within the LIGO/Virgo detection volume. In § 2.6 conclusions are given.

2.2   Relativistic Motion and the Prompt Gamma-Ray Emission

Observed GRBs contain a large fraction of high energy γ-ray photons, which can produce electron-positron pairs if they interact with lower energy photons. If the optical depth for this process is large, pairs will form rapidly and Compton scatter other photons, resulting in an increased optical depth. The optical depth for the pair creation is very sensitive to the Lorentz factor of the source $\tau_{\gamma\gamma} \propto \Gamma^{-6}$ (e.g. Piran, 1999; Lithwick & Sari, 2001, for the typical high energy spectral index $\beta \sim 1$). The source becomes optically thin if it is expanding with a Lorentz factor $\Gamma \gtrsim 100$.

    If there are baryons in GRB outflows, another limit on Γ can be obtained by con-

sidering the scattering of photons by electrons associated with these baryons (e.g. Lithwick & Sari, 2001). Note that high polarization results still suggest magnetized baryonic jets, rather than Poynting-flux dominated jets (Steele et al., 2009; Mundell et al., 2013). The optical depth due to these electrons at radius R is $\tau = \sigma_T E/(4\pi R^2 m_p c^2 \Gamma)$ where σ_T is the Thomson cross-section, E is the total isotropic explosion energy and m_p the proton mass. Outflows become optically thin at the photospheric radius,

$$R_\star \sim 6 \times 10^{13} E_{51}^{1/2} \Gamma_1^{-1/2} \text{cm}. \tag{2.1}$$

where $E_{51} = E/10^{51}$ergs and $\Gamma_1 = \Gamma/10$. On the other hand, the variability timescale δt in GRBs constrains the radius from which the radiation is emitted,

$$R_\gamma \sim \Gamma^2 c \delta t \sim 3 \times 10^{11} \delta t_{-1} \Gamma_1^2 \text{cm}. \tag{2.2}$$

where $\delta t_{-1} = \delta t / 0.1$ seconds. Requiring $R_\gamma > R_\star$, we obtain $\Gamma \gtrsim 80 E_{51}^{1/5} \delta t_{-1}^{-2/5}$. For outflows with a small Lorentz factor $\Gamma \lesssim 100$, the internal dissipation happens when the outflow is still optically thick. The photons will remain trapped and the thermal energy will be converted back to the kinetic form (Kobayashi & Sari, 2001; Kobayashi et al., 2002), and the prompt γ-ray emission would be suppressed (i.e. failed GRBs).

Usually outflows are assumed to have a sub-relativistic temperature after the internal dissipation, and the internal energy density is comparable to the mass energy density $e_{int} \sim e_{mass}$. If a significant fraction of the internal energy is converted to electron-positron pairs, the number density of the electrons and positrons $\lesssim e_{int}/m_e c^2$ could be larger by a factor of $\lesssim m_p/m_e$ than that of electrons that accompany baryons, where m_e is the electron mass. A more detailed discussion (Lithwick & Sari, 2001) also shows that the scattering of photons by pair-created electrons and positrons is nearly always more important than that by electrons that accompany baryons. Since

the lepton pairs create an effective photosphere further out than the baryonic one, the approximation in equation (2.1) will provide conservative estimates when we discuss failed GRB rates in § 2.4 and § 2.5.

2.3 On-Axis Orphan Afterglow

Even if a jet does not have a velocity high enough to emit γ-rays, it eventually collides with the ambient medium to emit at lower frequencies. Such synchrotron shock radiation has been well studied in the context of GRB afterglows (e.g. Rees & Meszaros, 1992; Mészáros & Rees, 1997; Sari & Piran, 1999; Kobayashi et al., 1999).

Because of relativistic beaming, the radiation from a jet can be described by a spherical model when $\Gamma > 1/\theta_j$ where θ_j is the jet half-opening angle. We here consider a relativistic shell with an energy E and an initial Lorentz factor Γ expanding into ISM with particle density n. The deceleration of the shell happens at

$$t_{\mathrm{dec}} \sim 0.48 \, E_{51}^{1/3} \, n_{-1}^{-1/3} \, \Gamma_1^{-8/3} \text{ days}, \tag{2.3}$$

where $n_{-1} = n/10^{-1}$ protons cm^{-3}, and t_{dec} is measured in the GRB rest frame (Sari & Piran, 1995). The typical frequency and the spectral peak flux of the forward shock emission at the deceleration time t_{dec} are

$$\nu_m \sim 5.3 \times 10^{11} \varepsilon_{B,-2}^{1/2} \varepsilon_{e,-1}^2 n_{-1}^{1/2} \Gamma_1^4 \text{ Hz, and} \tag{2.4}$$

$$F_{\nu,\mathrm{max}} \sim 35 D_{27}^{-2} \varepsilon_{B,-2}^{1/2} n_{-1}^{1/2} E_{51} \text{ mJy}, \tag{2.5}$$

(Sari et al., 1998; Granot & Sari, 2002) where ε_B and ε_e are the microscopic parameters, $\varepsilon_{B,-2} = \varepsilon_B/10^{-2}$, $\varepsilon_{e,-1} = \varepsilon_e/10^{-1}$, and $D_{27} = D/10^{27}$cm (i.e. the LIGO range for face-on NS-NS mergers). The optical emission, assumed to be between the peak

frequency ν_m and the cooling frequency ν_c, is expected to rise as $F_\nu \sim t^3$ and decay as $\sim t^{-1}$ after the peak $t = t_{\rm dec}$.

Self-absorption can significantly reduce synchrotron shock emission at low frequencies. The upper limit can be approximated as black body flux for the forward shock temperature (e.g. Sari & Piran, 1999), and the limit at $t_{\rm dec}$ is

$$F_{\nu,\rm BB} \sim 2.2 \times 10^2 \varepsilon_{e,-1} \nu_{10}^2 \Gamma_1^2 D_{27}^{-2} \left(\frac{R_\perp}{2.5 \times 10^{16} cm} \right)^2 \; \text{mJy}, \tag{2.6}$$

where $\nu_{10} = \nu/10\text{GHz}$ and the observable blast-wave size $R_\perp \sim 2c\Gamma t$. Equalizing the synchrotron emission and the black body limit, we obtain the self-absorption frequency $\nu_a \sim 1.5\varepsilon_{B,-2}^{1/5}\varepsilon_{e,-1}^{-1}n_{-1}^{3/5}E_{51}^{1/5}$ GHz at the deceleration time $t_{\rm dec}$. The self-absorption limit initially increases as $t^{1/2}$, and then steepens as $t^{5/4}$ after ν_m crosses the observational frequency ν. Considering that the synchrotron flux at $\nu < \nu_m$ also increases as $t^{1/2}$, if $\nu < \nu_a$ at $t_{\rm dec}$, the synchrotron emission would be reduced by the self-absorption at least until the passage of ν_m through the observational band at $t_m \sim 110\varepsilon_{B,-2}^{1/3}\varepsilon_{e,-1}^{4/3}E_{51}^{1/3}(\nu/150\ \text{MHz})^{-2/3}$ days. If the jet break happens while the flux is still self-absorbed, the light curve becomes flat $F_{\nu<\nu_a} \sim$ const (Sari et al., 1999). However, this estimate is obtained by assuming rapid lateral expansion (i.e. $R_\perp^2 \propto t$). Recent studies show that the sideways expansion is rather slow especially for mildly-relativistic jets (Granot & Piran, 2012; van Eerten & MacFadyen, 2012). We will assume that the blast-wave emission starts to decay at the jet break,

$$t_j \sim 13.5E_{51}^{1/3}n_{-1}^{-1/3}\left(\frac{\theta_j}{20°}\right)^{8/3} \text{days}, \tag{2.7}$$

even if it is in the self-absorption phase. At low frequencies $\nu \lesssim 1\,\text{GHz}$ and early times, forward shock emission would be affected by synchrotron self-absorption. However, currently most radio afterglow observations are carried out at higher frequencies (e.g.

VLA 8.5 GHz) at which self-absorption is more important for the reverse shock emission.

Just before the deceleration time t_{dec}, a reverse shock propagates through the jet and heats the original ejecta from the central engine. The reverse shock region contains energy comparable to that in the forward shock region. However, it has a lower temperature due to a higher mass (i.e. lower energy per particle). The shock temperature and the typical frequency are lower by a factor of $\sim \Gamma$ and $\sim \Gamma^2$ compared to those of the forward shock (e.g. Kobayashi & Zhang, 2003). Although reverse shocks in low Γ jets could emit photons in the radio band, the self-absorption limit is tighter due to the lower shock temperature; we find that the forward shock emission always dominates. Note that we rarely catch the reverse shock emission even for regular GRBs with detectable γ-ray emission. We will discuss only the forward shock (i.e. blast wave) emission here.

2.4 Monte Carlo Model

By using the estimates of Lorentz factors based on long GRB afterglow peak times, Hascoët et al. (2014) demonstrated that an apparent correlation between isotropic γ-ray luminosity L_γ and Lorentz factor Γ can be explained by a lack of bright bursts with low Lorentz factors. They have also predicted the existence of on-axis orphan afterglows of long GRB events. We here extend their argument to short GRBs, and we apply their formalism to cosmological (i.e. γ-ray satellite range) and local (i.e. GW detector range) events to study the on-axis orphan afterglows of failed short GRBs (i.e. low Γ events). The following assumptions are made in our simple Monte Carlo simulation of a synthetic population of merger events:

1. The redshift for each event is randomly determined using a distribution with a

constant time delay with respect to the star formation rate, where the peak rate is at $z = 0.9$ (Wanderman & Piran, 2015). The redshift limits of $0 \leq z \leq 3$ are used for the cosmological sample, and $0 \leq z \leq 0.07$ for local sample, i.e. advanced LIGO/Virgo detectable range $D \sim 1.5 \times 200$ Mpc = 300 Mpc for NS-NS mergers where the factor of 1.5 accounts for the stronger GW signal from face-on mergers (Kochanek & Piran, 1993). We use the event rate per unit comoving volume for short GRBs obtained by Wanderman & Piran (2015), which is a function of z as

$$R_{\text{SGRB}}(z) \propto \begin{cases} e^{(z-0.9)/0.39} & z \leq 0.9 \\ e^{-(z-0.9)/0.26} & z > 0.9 \end{cases}. \tag{2.8}$$

Numerical results for the cosmological cases are insensitive to the value of the maximum z as long as it is much larger than unity.

2. A power-law distribution of Lorentz factors $N(\Gamma) \propto \Gamma^{-a}$ is assumed with reasonable limits $3 \leq \Gamma \leq 10^3$. Motivated by AGN studies (e.g. Lister & Marscher, 1997; Marscher, 2006b), we choose $a = 1.75$ as our fiducial value and the cases of $a = 1.5$ and 2 will be briefly discussed.

3. The isotropic γ-ray luminosity L_γ is randomly generated in the limit 10^{50}erg/s $\leq L_\gamma \leq 10^{53}$erg/s where the limits come from observational constraints and the luminosity distribution follows the form obtained by Wanderman & Piran (2015),

$$\Phi(L_\gamma) \propto \begin{cases} L_\gamma^{-1} & L_\gamma \leq 2 \times 10^{52} \text{ erg/s} \\ L_\gamma^{-2} & L_\gamma > 2 \times 10^{52} \text{ erg/s} \end{cases}, \tag{2.9}$$

where this luminosity function is logarithmic in the interval $d\log L_\gamma$.

For each event, the dissipation radius $R_\gamma = \Gamma^2 c\delta t$ is evaluated by using a random Γ and the typical pulse width in short GRB light curves $\delta t = 0.1$ s (Nakar & Piran, 2002). γ-ray photons are assumed to be emitted at R_γ with a random γ-ray luminosity L_γ or equivalently a random isotropic γ-ray energy $E_\gamma = L_\gamma T$ where T is the duration of short GRBs. We assume $T = 0.6$ s for all bursts as this is the median value for short gamma-ray bursts (Zhang et al., 2012). The spectral peak energy in the νF_ν spectrum is known to be correlated with L_γ (Yonetoku et al., 2004; Ghirlanda et al., 2009). The correlation is consistent for both long and short GRBs (Zhang et al., 2012), and given by

$$E_p \sim 300 \left(\frac{L_\gamma}{10^{52}\text{erg/s}} \right)^{2/5} \text{keV}. \qquad (2.10)$$

The νF_ν spectrum is assumed to follow a broken power-law with low-energy index (below E_p) of $1.5 = (-\alpha + 2)$, and a high-energy index of $-0.25 = (-\beta + 2)$, where α and β are the photon number spectral indices. The mean index values for all GRBs are $\alpha = 1$ and $\beta = 2.5$ (Gruber et al., 2014) but as short GRBs are typically harder than average we use the values $\alpha = 0.5$ and $\beta = 2.25$. The spectral peak is normalized as the value integrated between 1 keV and 10 MeV giving L_γ. If the outflow is optically thin, all the photons released at R_γ are radiated away. The event is considered to be detectable if the photon flux at the detector in the Swift band (15-150 keV) is > 0.2 photons s^{-1} cm^{-2} (Band, 2006). We take into account the redshift of the spectrum when the photon flux is evaluated.

If the optical depth at the dissipation radius R_γ is more than unity, or equivalently the photospheric radius $R_\star = \sqrt{\sigma_T E/4\pi m_p c^2 \Gamma}$ is larger than the dissipation radius, the γ-ray emission would be suppressed where $E = E_\gamma/\eta$ is the explosion energy and η is the conversion efficiency from the explosion energy to γ-rays. We use $\eta = 0.2$, which is consistent with both theoretical predictions (Kobayashi et al., 1997) and the fiducial value used in other works (Liang et al., 2010; Ghirlanda et al., 2012). The

γ-ray energy injected at R_γ is adiabatically cooled, and the photons decouple from the plasma at $R_\star$. Assuming a sharp transition from optically thick to thin regimes (see Beloborodov, 2011, for the discussion of a fuzzy photosphere), we use hydrodynamic scalings to estimate the cooling factor. The internal energy density (photon energy density) decays as $e \propto R^{-8/3}$ and the Lorentz factor is constant for an outflow with a sub-relativistic temperature (Piran et al., 1993). Considering that the internal energy in the outflow shell with width Δ is $L_\gamma \Delta / c \propto eR^2 \Delta \Gamma^2$, the luminosity of photons released at R_γ is

$$L_\gamma(R_\star) \sim L_\gamma \left(\frac{R_\star}{R_\gamma}\right)^{-2/3}, \tag{2.11}$$

where we have assumed no shell spreading, $\Delta \sim$ const. The spectral peak energy is similarly shifted as $E_p(R_\star) = E_p(R_\star/R_\gamma)^{-2/3}$. The photons in the coupled plasma undergo pair production and Compton down-scattering that progressively thermalises the distribution (Hascoët et al., 2014). The electron temperature at R_γ can be approximated by a black-body temperature $\phi_{bb} \sim (L_\gamma/4\pi R_\gamma^2 \Gamma^2 ca)^{1/4}$ where a is the radiation constant. The optical depth at R_γ is given by $\tau_d \sim (R_\star/R_\gamma)^2$. The condition for efficient thermalisation is $\tau_d \gtrsim m_e c^2 / k_B \phi_{bb}$ (Pe'er et al., 2005; Thompson et al., 2007) where m_e is the mass of an electron and k_B the Boltzmann constant. The peak energy E_p for such a case is given by $3k_B \phi_{bb}$, above which the distribution is exponentially suppressed. For simplicity we assume $E_p \equiv E_{\max}$. If $\tau_d \lesssim m_e c^2 / k_B \phi_{bb}$, the photons are not efficiently thermalised. The distribution is then limited by the efficiency of pair production where the maximum energy is $E_{\max} \sim 511(\Gamma/\tau_d)$ keV. The distribution is cut off above this energy.
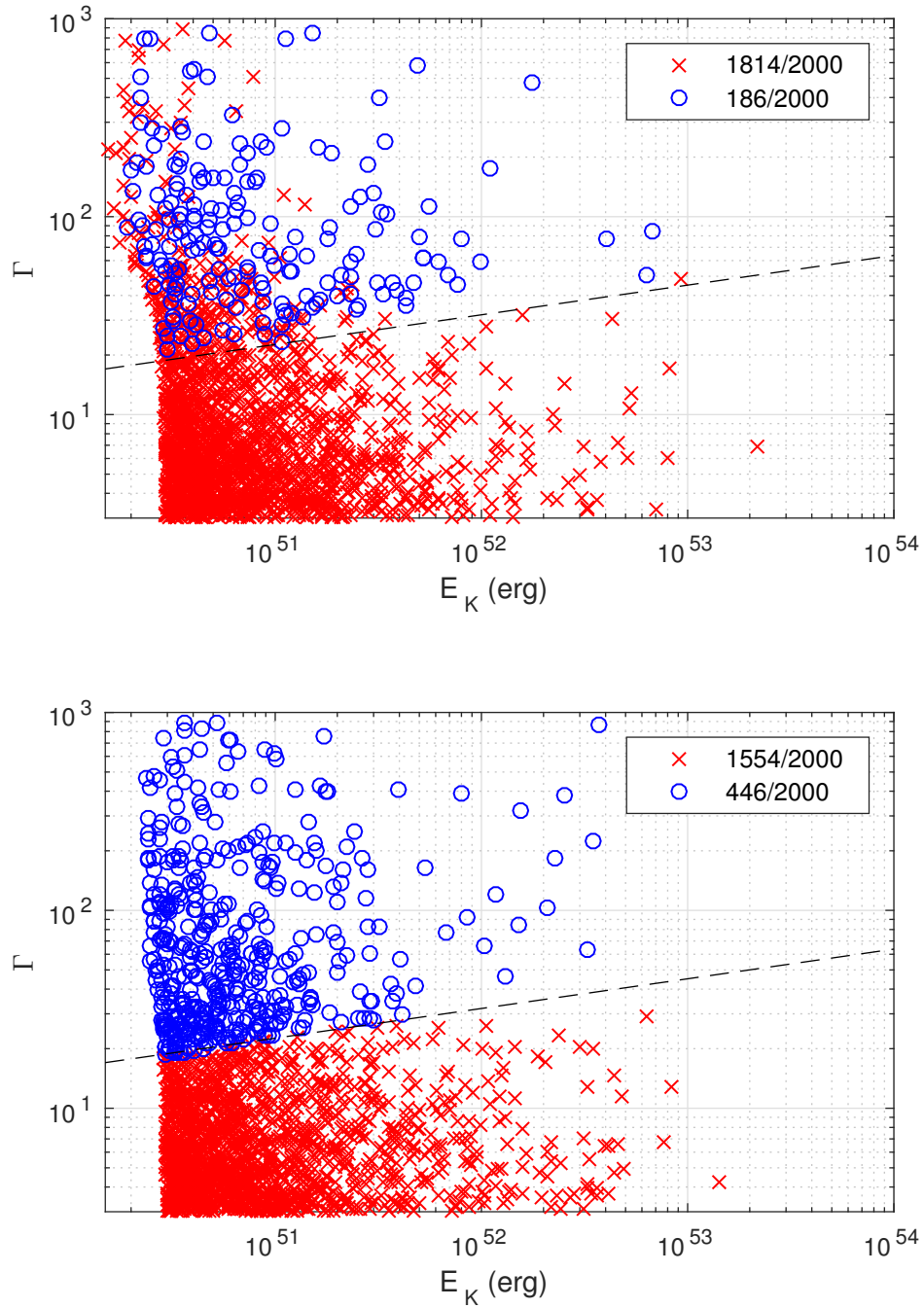
Figure 2.1: Isotropic kinetic energy E_k vs bulk Lorentz factor Γ. *Monte Carlo* generated synthetic population of bursts. Top panel: Cosmological sample of events with $0 \leq z \leq 3$. Bottom panel: Local sample of events with $0 \leq z \leq 0.07$. Bursts with prompt emission flux above the Swift sensitivity are shown as the blue circles. Failed GRBs are indicated by the red crosses. $a = 1.75$ is assumed.

2.4.1 Numerical Results

We generate a sample of 2×10^5 events and evaluate the γ-ray flux for each in the Swift band. To allow for clarity without losing the general trend, the results for a population of 2000 events are shown in Figure 2.1; the blue circles and red crosses show the events detectable and undetectable by Swift, respectively. The isotropic kinetic energy E_{k} is the energy in the blast wave after deceleration time, $E_{\mathrm{k}} = E - E_\gamma$, where E is the total isotropic explosion energy, and E_γ is the isotropic γ-ray energy at the photospheric radius $R_\star$. The Lorentz factor Γ of an outflow at $t < t_{\mathrm{dec}}$ is shown against this. The top panel shows the results with $0 \leq z \leq 3$, where we find a small fraction $\sim 9\%$ of the total population and $\sim 49\%$ of the events with $\Gamma > 30$ are detectable by Swift. For the local population $0 \leq z \leq 0.07$, these fractions are higher, at $\sim 22\%$ and $\sim 100\%$ respectively, due to the proximity (see the bottom panel). The dashed line indicates the lower limit for a successful GRB; events below this line have the prompt γ-ray emission fully suppressed. The cut off, with the parameters used, is given by $\Gamma \sim 16 \left(E_{\mathrm{k}}/10^{50}\mathrm{erg}\right)^{0.15}$.

In Figure 2.1, the low-energy limit of E_{k} is basically set by the Monte-Carlo luminosity distribution (i.e. $L_{\gamma,\mathrm{min}} = 10^{50}$ erg/s. Note that the explosion energy E is higher than the γ-ray energy $L_\gamma T$ at the dissipation radius R_γ by a factor of $1/\eta \sim 5$). If we consider the local population (the bottom panel), for the events above the dashed line (i.e. the blue circles) all of the γ-ray energy is successfully radiated away, whereas for the events below the dashed line (i.e. the red crosses), almost all of the γ-ray energy is reabsorbed into the outflow. Thus the distribution of E_{k} for the blue circles has a slightly lower limit. If we consider the cosmological population (the top panel), a fraction of events are distant and intrinsically dim. They are undetectable by Swift even if all gamma-ray energy is successfully radiated away at R_γ. This is why there are red crosses above the dashed line for the cosmological population. The fraction of the

events detectable by Swift weakly depends on $L_{\gamma,min}$. If we assume $L_{\gamma,min} = 5 \times 10^{49}$ erg/s, Swift would be able to detect $\sim 6\%$ of the total cosmological population, and $\sim 25\%$ of the total local population.

Liang et al. (2010); Ghirlanda et al. (2012) and Tang et al. (2015) report correlations between Lorentz factor Γ and the isotropic luminosity L_γ (or the isotropic energy E_γ) for long GRBs: $E_\gamma \propto \Gamma^{4.00}$; $L_\gamma \propto \Gamma^{2.15}$; and $L_\gamma \propto \Gamma^{1.92}$, respectively. However, such power-law relations could indicate a lower limit on Γ for observable long GRBs with a given burst energy (Hascoët et al., 2014). In our simulation, we find that the detectable short bursts are always located above a line $\Gamma \sim 20(E_\gamma/10^{49}\mathrm{erg})^{0.17}$ giving a lower limit relation $E_\gamma \propto \Gamma^{5.88}$.

As discussed in §2.3, the kinetic energy E_k of the failed GRBs will be released as on-axis orphan afterglows at late times. Figure 2.2 shows the distributions of the peak flux (the top panel) and peak time (the bottom panel) of such X-ray, optical, and radio transients. To estimate these distributions, we have used the Monte Carlo results for the local sample ($D < 300$ Mpc) with model parameters: $n = 10^{-1}$ protons cm^{-3} (Berger, 2014; Metzger & Berger, 2012), $\varepsilon_B = 10^{-2}$, $\varepsilon_e = 10^{-1}$ (Panaitescu & Kumar, 2002; Yost et al., 2003; Berger, 2014), the index of the power-law distribution of random electrons accelerated at shock $p = 2.5$ (Sari et al., 1996; Daigne et al., 2011; Metzger & Berger, 2012), and the jet half-opening angle $\theta_j = 20°$ ensures $t_j > t_\mathrm{dec}$ for our sample and is within the limits $16 \pm 10°$ found by Fong et al. (2015) for short GRB. The jet opening angle plays a role only when we estimate the jet break time.

The dotted green lines in Figure 2.2 indicate the distributions for X-ray transients. The typical frequency of the blast wave emission ν_m is sensitive to the Lorentz factor $\nu_m \propto \Gamma^4$. Since, for the local population the on-axis orphan afterglows are produced by low Γ jets ($\Gamma \lesssim 30$), the typical frequency ν_m is expected already to be below the X-ray and optical bands at the deceleration time t_dec. The X-ray and optical light
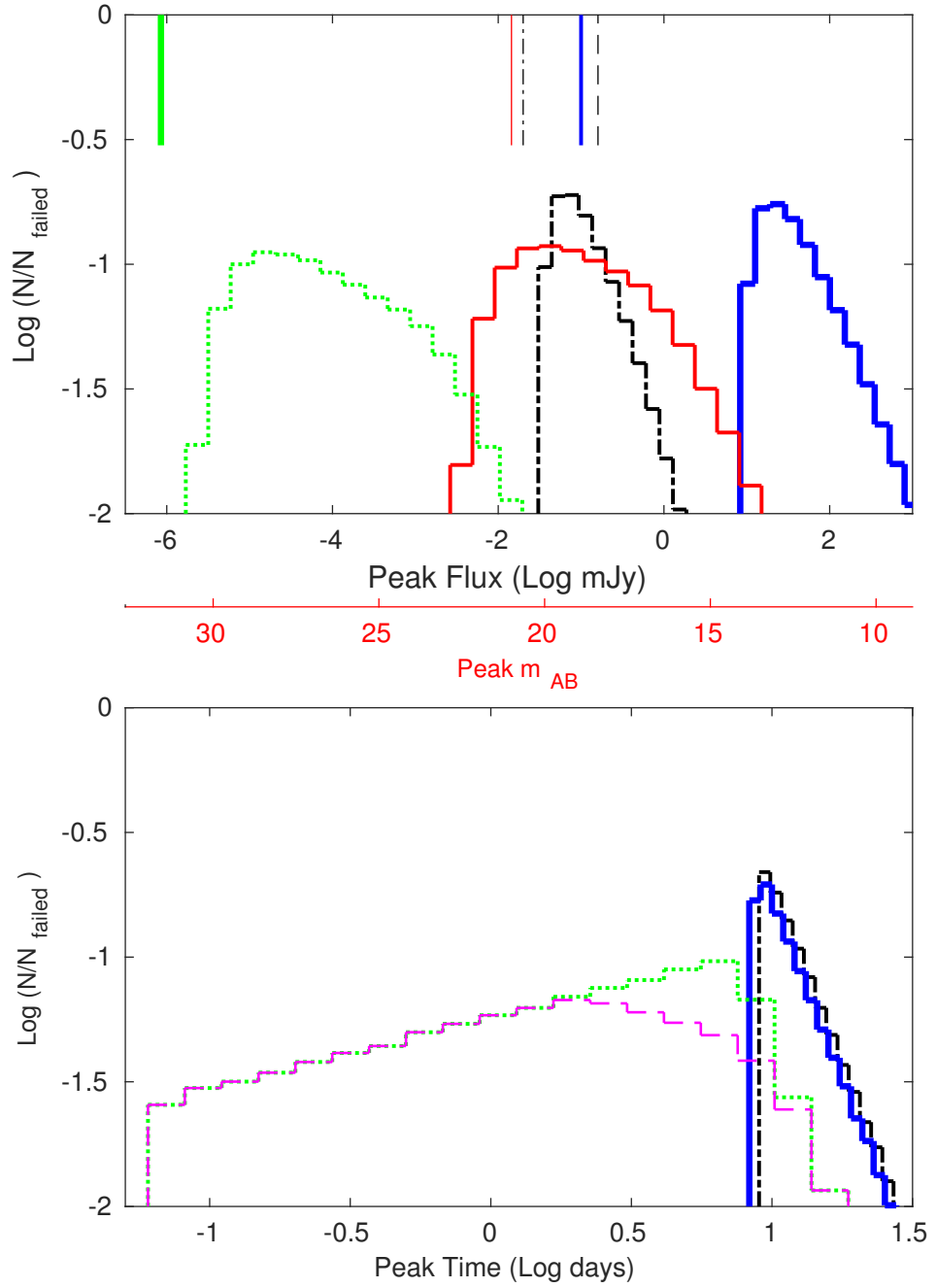
Figure 2.2: The peak-flux (top panel) and peak-time (bottom panel) distributions of on-axis orphan afterglows from failed GRB events within 300 Mpc. The distributions are normalized by the total number of failed GRBs, and show X-ray (dotted green line), optical (thick solid red line), radio 10 GHz (thick solid blue line) and radio 150 MHz (thick dash-dotted black line) distributions. The vertical lines in the top panel indicate the sensitivity limits of telescopes (thick green XRT, thin red optical ~ 2 m, dash-dotted SKA1-Low, and dashed 48 LOFAR), and the dashed magenta line in the bottom panel shows the distribution of bright events $m_g \leq 21$ (see the main text for details).

curves should peak at t_{dec} and they have the same peak time distribution. Considering that the deceleration time $t_{\mathrm{dec}} \propto E_{\mathrm{k}}^{1/3}\Gamma^{-8/3}$ is mainly determined by Γ, we can roughly estimate the peak-time distribution $dN \propto \Gamma^{-a}d\Gamma \propto t_{\mathrm{dec}}^{3(a-1)/8}d(\log t_{\mathrm{dec}})$. For $a \gtrsim 1$, the distribution is wide and a large fraction of the events have the peak-time t_{dec} around several days after the merger event. If a minimum Lorentz factor $\Gamma_{min} = 2$ is assumed, the peak-time distribution would achieve the peak around a few weeks after the merger event. The distribution of the peak X-ray flux, where the frequency is above the cooling frequency $\nu_x > \nu_c$, is $F_p = (\nu_c/\nu_m)^{-(p-1)/2}(\nu_x/\nu_c)^{-p/2}F_{\nu,\mathrm{max}} \propto \Gamma^{2(3p-2)/3}E_{\mathrm{k}}^{2/3}$, is shown in the top panel. Given good localisation, all of the X-ray peak afterglow flux is above the minimum sensitivity of the Swift XRT 2.4×10^{-14} erg cm^{-2} s^{-1} for 10^4 seconds (the vertical green thick solid line). The X-ray afterglows are below the trigger sensitivities of Swift BAT and MAXI; and too faint to be detectable by the Swift BAT survey.

The solid red line in the top panel and the dotted green line in the bottom panel of Figure 2.2 indicate the distributions for optical (*g*-band) transients. The AB magnitude m_{AB} axis is shown below the top panel to indicate the optical flux. For optical transients, peak flux is $F_p = (\nu_{opt}/\nu_m)^{-(p-1)/2}F_{\nu,\mathrm{max}} \propto \Gamma^{2(p-1)}E_{\mathrm{k}}$, and 85% of the optical orphan afterglows are brighter than $m_g = 21$ (the vertical solid red line indicates this typical limit for mid-sized (~ 2 m) telescopes). The peak-time distribution for the bright events ($m_g < 21$) is shown as the dashed magenta line in the bottom panel. The difference between the dotted green (representing both X-ray and optical in peak time) and dashed magenta line corresponds to the dim event population ($m_g > 21$). Since these events tend to have low Γ, their typical frequencies are much lower than the optical band, and they peak at late times.

The solid blue lines give the distributions for radio (10 GHz) transients. The typical frequency ν_m is expected to be above 10 GHz at the deceleration time t_{dec}.

The light curve peaks when the typical frequency $\nu_m \propto t^{-3/2}$ crosses the observational band: $t_p \propto E_{\mathrm{k}}^{1/3}$. Since the dynamics of the blast wave at $t > t_{\mathrm{dec}}$ depends only on the Sedov length[1] $\propto E_{\mathrm{k}}^{1/3}$ and not on the initial Lorentz factor Γ, the peak-time distribution should be narrowly clustered, compared to the distribution of the optical transients. The Monte Carlo results actually give a narrow peak around $t_p \sim 10$ days. The peak flux $F_p = F_{\nu,\mathrm{max}} \propto E_{\mathrm{k}}$ is bright: typically $10 - 100$ mJy. VLA (the vertical solid blue line) can easily detect the transients.

The dash-dotted black lines indicate the distribution for radio (150 MHz) transients. As we have discussed, this low frequency emission is suppressed by self-absorption, and the jet break is likely to happen before it becomes optically thin. The peak-time of the light curve is determined by the jet break time $t_p \propto E_{\mathrm{k}}^{1/3}\theta_j^{8/3}$. For the fixed $\theta_j = 20°$, we find that the peak-time distribution is similar to that for 10 GHz transients and it peaks around $t_p \sim 10$ days. However, since the emission is still suppressed by the self-absorption at the peak time, the peak flux is much lower: $F_p \sim 0.1$ mJy. Approximately 30% of the 150 MHz transients are brighter than the sensitivity limit of 48 LOFAR stations (the vertical dashed black line), and all are brighter than the sensitivity limit for SKA1-Low (the vertical dash-dotted black line).

Typical afterglow light curves for a selection of on-axis orphan afterglows are shown in Figure 2.3. An average luminosity distance for NS-NS GW detectable mergers from our sample is used of ~ 220 Mpc. X-ray, optical, and radio (10 GHz) are shown for 4 combinations of Γ and E_{k}. The vertical dashed line in each panel represents the deceleration time t_{dec}, and as this is most sensitive to Γ (see equation 2.3) the lower Lorentz factor cases (top two panels) have a significantly later deceleration time. The vertical dotted line in each panel represents the jet-break time t_j, a jet half-opening

---

[1] The Sedov length is defined as the radial distance l where the blast energy E is equal to the rest energy of the enclosed volume, $E = 4\pi l^3 n m_p c^2 / 3$, where l is the Sedov length and we assume spherical symmetry
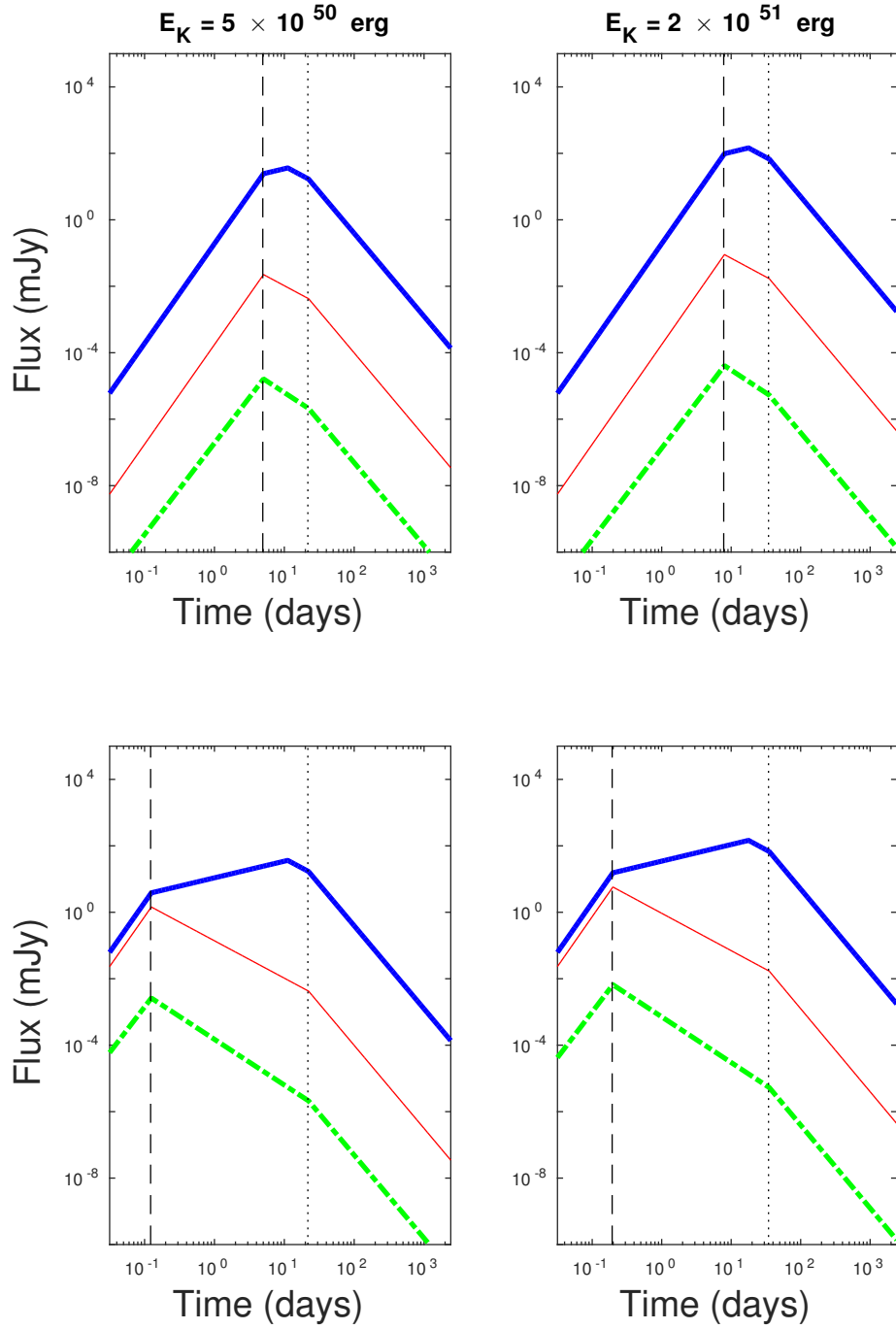
Figure 2.3: The light curves of on-axis orphan afterglows at 220 Mpc with various bulk Lorentz factors Γ and isotropic kinetic energies $E_{\rm k}$. The top (bottom) two panels have a $\Gamma = 5(20)$, and the left(right) panels have an energy $E_{\rm k} = 0.5(2) \times 10^{51}$ erg. X-ray afterglows are shown as dashed green lines, optical are shown as red thin solid lines, and radio (10 GHz) are shown as blue thick solid lines. The vertical black dotted lines represent the deceleration time $t_{\rm dec}$ and the jet-break time t_j (assuming $\theta_j = 20°$)

angle $\theta_j = 20°$ is used throughout, and for narrower (wider) jet half-opening angles the break time will be at earlier (later) times. The jet-break time is only weakly dependent on the kinetic energy (see equation 2.7). In all cases the X-ray (green dash-dotted line) and the optical (thin red line) peak at the deceleration time, while the 10 GHz emission (thick blue line) is shown to peak at a later time t_m when the typical frequency $\nu_m(t)$ crosses the radio frequency. In all cases at times earlier than $t_{\rm dec}$ the flux is $\propto t^3$, while for the X-ray and optical the flux at $t_{\rm dec} < t < t_j$ is $\propto t^{-3(p-1)/4}$. At 10 GHz the flux is $\propto t^{1/2}$ at $t_{\rm dec} < t < t_m$, and $t^{-3(p-1)/4}$ after t_m and before t_j. In all cases at $t > t_j$ the flux is $\propto t^{-p}$.

2.5 Event Rates and On-axis Probability

The Swift satellite has been detecting short GRBs at a rate of ~ 10 yr^{-1} since the launch in 2004, and $\sim 1/4$ of the detected events have measured redshifts (Swift GRB catalogue). Unfortunately no Swift short GRB with known redshift has been detected within the advanced LIGO/Virgo range for face-on NS-NS mergers $D \sim 300$ Mpc, and only three (061201, 080905A, and 150101B) have occurred within the face-on NS-BH range $D \sim 600$ Mpc (Abadie et al., 2010). Metzger & Berger (2012) estimate that $\lesssim 0.03$ (0.3) short GRBs per year, with redshift measurements, are currently being localized by Swift within $D \sim 300$Mpc (600Mpc). Considering that the field of view of the Swift BAT is ~ 2sr, the all-sky rate of detectable short GRBs with or without redshift information is higher by a factor of ~ 25.

If the distribution of Γ is described by the power-law $N(\Gamma) \propto \Gamma^{-a}$, when we consider the rate of jets from mergers regardless of inclination or detectability, the rate for failed GRBs would be higher than the short GRB rate. For local population $D \lesssim 300$ Mpc, we find that the fraction of failed events is about 66% for $a = 1.5$, 78%

for 1.75, and 87% for 2 (the same rates are obtained for a population of $D \lesssim 600$Mpc). If $a = 1.75(2)$, the failed GRB rate is higher by a factor of $\sim 3.5(6.7)$ than the short GRB rate (i.e. the ratio of failed to successful GRBs). The all-sky rate of the failed GRBs with or without redshift information is about 2.6(5.1) per year for the NS-NS range and 26(51) per year for the NS-BH range. Here we assumed the jet opening angle distribution does not depend on the Lorentz factor of the jets (i.e. GRB and failed GRB jets have the same opening angle).

The jet half-opening angle is not well constrained for short GRB jets (the median value for 248 long GRBs is $\theta_j \sim 13°$; e.g. Fong et al., 2015). Using four short GRBs which have temporal steepenings on timescale of $\sim 2 - 5$ days, the median value is estimated as $\sim 6°$ (Fong et al., 2015). However, the majority of short GRBs do not have a detected jet break, and the inclusion of these bursts is essential in understanding the true opening angle distribution. Based on a probability argument, Fong et al. (2015) obtain the median value $\theta_j \sim 16°$ and $33°$ if the maximum possible angle is $30°$ and $90°$, respectively.

If the typical jet half-opening angle of short GRBs is $\theta_j \sim 16°$, the beaming factor is $f_b \equiv 1 - \mu \sim 4 \times 10^{-2}$ where $\mu = \cos\theta_j$, only a small fraction of short GRB jets point toward us (see the black dashed line in Figure 2.4). However, since the GW polarization components $h_+ \propto (1 + \cos^2 i)$ and $h_\times \propto 2\cos i$ depend on the inclination angle i of the binary, mergers emit GWs much more strongly along the polar axis than in the orbital plane. Considering that the jets from the mergers are also likely to be directed along the polar axis, Kochanek & Piran (1993) show that when a GRB is associated, the GW amplitude h is stronger by a factor of $A \equiv (1 + 11\mu/16 + 11\mu^2/16 + \mu^3/16 + \mu^4/16)^{1/2}$ than the amplitude averaged over the sky (as seen from the source). The distances out to which GW detectors could detect the binary increases by a factor of A if the jet points toward us (we define an on-axis event
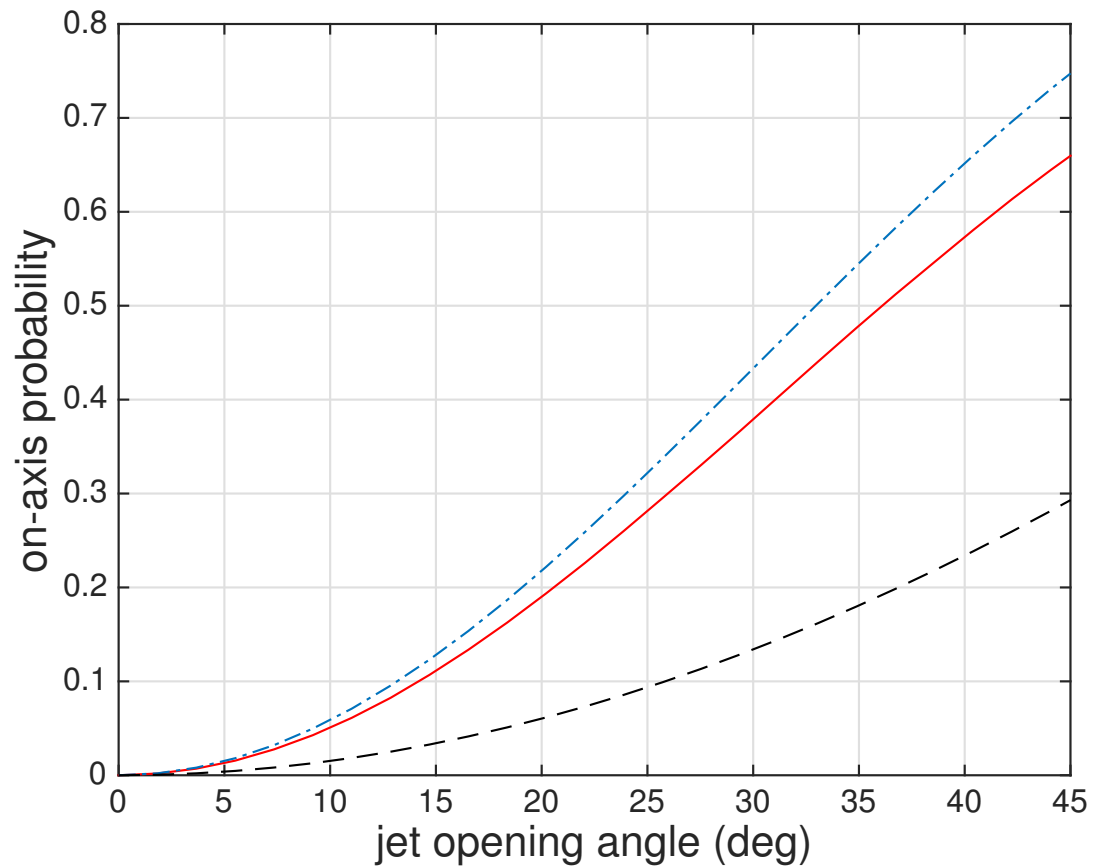
Figure 2.4: On-axis probability as a function of a jet half-opening angle θ_j. The beaming factor $f_b = 1 - \cos\theta_j$ (black dashed line), the simple approximation $A^3 f_b$ (blue dash-dot line), and the Monte Carlo results (red solid line).

as any jet where the inclination is within the half-opening angle, $i \leq \theta_j$).

When we consider a sample of merger GW events detected by a GW detector with sensitivity h_c, their jets would tend to be directed to us. This is because on-axis events are detectable at a larger distance. The on-axis probability could be higher by roughly the volume factor of A^3 (the blue dash-dotted line, figure 2.4) than the simple geometric estimate f_b (i.e. our line-of-sight falls within the opening angle of the jet with a higher probability). We also conduct a Monte Carlo simulation to estimate the on-axis probability. In the simulation, mergers are uniformly distributed in space, with a random inclination angle, and they emit GWs with amplitude $h \propto \sqrt{h_+^2 + h_\times^2}/D$. After selecting the events detectable by a GW detector: $h > h_c$, we evaluate the fraction of the events which have an inclination angle smaller than a given jet half-opening angle θ_j; we assume uniform jets with a top hat distribution throughout [2]. The result (the red solid line) does not depend on the detector sensitivity as long as the merger distribution is homogeneous. If we consider GW trigger events, the on-axis probability (the red solid line; 13% and 44% for $\theta_j = 16°$ and $33°$, respectively) is much higher than the beaming factor (the black dashed line). Although isotropic EM counterparts such as macronovae could be ideal to localize a large sample of GW events, $> 20\%$ of GW events would still be associated with the on-axis orphan afterglow of failed GRBs especially when they have wider jet opening angles compared to short GRB jets. For long GRB jets, observational results indicate such a correlation $\Gamma \propto \theta_j^{-\kappa}$ with $0.3 \leq \kappa \leq 2.7$ (Panaitescu & Kumar, 2002; Salmonson & Galama, 2002; Kobayashi et al., 2002; Ghirlanda et al., 2013). The failed GRB rates could be higher than those discussed at the beginning of this section.

---

[2] If the property of the jet depends on the angle θ from the jet symmetry axis (e.g. $\Gamma \propto \theta^{-b}$ outside of some core angle), only the central part could have Lorentz factors high enough to produce γ-rays. Although the detailed study is beyond the scope of this study, the failed GRB rate could be even higher for structured jets.

2.6 Conclusions

We have shown that failed GRBs are much more frequent than short GRBs when the Lorentz factors of jets from compact stellar mergers follow a similar power-law distribution to those observed for AGN. For most events the internal dissipation process happens when the jet is still optically thick, and the photons produced by the dissipation process will be converted back to the kinetic energy of the jet. By using a simple Monte Carlo model, we have shown that even for the local merger population within the LIGO/Virgo range, the γ-ray emission from jets with $\Gamma \lesssim 30$ will not be detected by γ-ray satellites (e.g. Swift). For a power-law distribution of the jet Lorentz factors $N(\Gamma) \propto \Gamma^{-1.75}$, 78% of compact object mergers that have jets result in a failed GRB. The failed GRB events will produce on-axis orphan afterglows at late times. Using the local short GRB rate as normalization, the all-sky rate of the on-axis orphan afterglows is about 2.6 and 26 per year for the NS-NS range (300 Mpc) and NS-BH range (600 Mpc), respectively. The opening angle of jets for long GRBs was found to be a function of Γ (e.g. Ghirlanda et al., 2013), and if low Γ jets from compact-binary mergers have wider half-opening angles θ_j than those of short GRBs then the real rate would be higher than these.

We have evaluated the peak time and peak luminosity of the on-axis orphan afterglows in X-ray, optical, and radio bands. Although it is usually difficult to model observational data for orphan afterglow candidates when the explosion time is unknown (i.e. the t_0 issue), for GW trigger events the GW signals will provide the explosion time t_0. The peak time distribution in the X-ray and optical band is rather wide $0.1 - 10$ days after the GW signals. Although the sky localization of sources by GW detectors is not accurate enough for follow-up observations by most conventional telescopes (Abbott et al., 2016a), 85% of the on-axis orphan afterglows are brighter than $m_g = 21$. The current and upcoming optical transient searches (e.g. iPTF/ZTF, Pan-STARRS,

GOTO, BlackGEM, Kiso, SkyMapper, Subaru HSC, LSST) should be able to detect the optical transients. The X-ray and/or optical detection can be followed by radio observations (e.g. VLA), also several radio instruments have the potential to be leading transient detectors due to their large FoV (e.g. SKA, LOFAR, APERTIF, MWA). Radio emission is expected to peak around 10 days after the merger events. Optical and radio observations will constrain the opening angle of low- and high- Γ jets.

Since merger jets from GW trigger events tend to be directed to us, the on-axis probability (e.g. 13% and 44% for $\theta_j = 16°$ and $33°$, respectively) is much higher than the beaming factor $f_b = 1 - \cos\theta_j$. A significant fraction of GW events could be associated with on-axis orphan afterglows. Observations of on-axis orphan afterglows and GRB afterglows will enable us to determine the Γ distribution of jets (e.g. clustered at high Γ, a power-law or a lognormal distribution, or multiple populations), and it will provide constraints on the acceleration process of relativistic jets.

3. Electromagnetic Counterparts to Structured Jets from Gravitational Wave Detected Mergers

This Chapter has been published as Lamb & Kobayashi (2017a).

3.1 Introduction

The mergers of binary neutron star (NS) systems or black-hole (BH) neutron star systems are thought to be the progenitors of short gamma-ray bursts (GRB) (Narayan et al., 1992; Mochkovitch et al., 1993; Bogomazov et al., 2007; Nakar, 2007; Berger, 2014). The rapid accretion of a merger debris disc onto a compact object can power relativistic bi-polar jets. Jet energy is initially dissipated internally producing the prompt γ-rays of a GRB. The jet interacts with the ambient medium at later times and develops an external shock which expands and produces a broadband afterglow (e.g. Piran, 2004; Zhang & Mészáros, 2004).

The inspiral and merger of a NS-NS or BH-NS system is caused by the emission of gravitational waves (GW). Such GWs are a target for ground-based GW detectors such as advanced LIGO, Virgo, and KAGRA (Abbott et al., 2016a; Aso et al., 2013). The

merger of binary BH systems produced the advanced LIGO detections GW150914, 151226, 170104, 170608, 170814 and the 87% confidence LVT151012 (Abbott et al., 2016b, 2017a). BH-BH mergers are not expected to produce an EM counterpart, however see Connaughton et al. (2016); Ackermann et al. (2016); Savchenko et al. (2016); Verrecchia et al. (2017); and various scenarios have been suggested (e.g. Loeb, 2016; Perna et al., 2016; Zhang, 2016; Yamazaki et al., 2016). To maximize the science returns from GW astronomy the detection of an EM counterpart is essential. GWs from a NS-NS merger were detected with GW170817 (Abbott et al., 2017c), and NS-NS and BH-NS mergers should be detected more frequently within the next few years. GW detections of BH/NS-NS mergers will trigger a broad-band search for electromagnetic (EM) counterparts. However, short GRBs rarely occur within the range of GW detectors, ~ 300 Mpc for face-on NS-NS mergers (Abadie et al., 2010); this is possibly due to the high collimation of the prompt γ-ray emission, where $\sim 0.5\%$ of jets with a half-opening angle $\theta_j \sim 6°$ would be inclined towards an observer, or a mis-match between short GRB peak energies and the *Swift* detection band makes detection more difficult. However, the afterglows from the merger jets may be observable as 'off-axis' orphans. Alternatively a large fraction of the jets from such mergers may have no bright prompt emission due to a low bulk Lorentz factor (Lamb & Kobayashi, 2016). More isotropic EM counterparts are often discussed to localize a large sample of GW events (e.g. Nakar & Piran, 2011; Metzger & Berger, 2012; Nissanke et al., 2013; Gao et al., 2013; Metzger et al., 2015; Kisaka et al., 2015a; Hotokezaka et al., 2016).

Other than the bi-polar jets, numerical simulations of NS-NS and BH-NS mergers show sub- and mildly- relativistic ejecta (e.g. Rosswog et al., 2000; Ruffert & Janka, 2001; Yamamoto et al., 2008; Kiuchi et al., 2010; Foucart et al., 2012; Deaton et al., 2013; Hotokezaka et al., 2013b; Dietrich et al., 2015; Kawaguchi et al., 2016; Dietrich & Ujevic, 2017; Ciolfi et al., 2017). Such ejecta is more isotropic in the case of

a NS-NS merger and highly anisotropic for BH-NS mergers (Kyutoku et al., 2015). This merger ejecta can produce macronovae (also called kilonovae) from the decay of r-process nucleosynthesis products (e.g. Li & Paczyński, 1998; Tanvir et al., 2013; Berger et al., 2013). Macronovae typically peak at red wavelengths with $\gtrsim$ 22 magnitude for a source at 200 Mpc (Tanaka, 2016). Radio flares are expected at much later times; 1-4 years and $\sim$ 1 mJy (Nakar & Piran, 2011; Hotokezaka et al., 2016). Aditionally, the jet must propagate through the merger ejecta, forming a cocoon that can collimate the outflow (Bromberg et al., 2011; Nagakura et al., 2014). A resultant cocoon-ejecta shock may give rise to X-ray or UV/optical emission (Nakar & Piran, 2017; Lazzati et al., 2017a). The jet will break out of the merger ejecta and continue to propagate into the ambient medium where the collimating pressure from the cocoon is lost. This transition can result in the jet becoming structured i.e. the energy ϵ and bulk Lorentz factor Γ vary across the jet cross-section (e.g. Lipunov et al., 2001; Zhang & Mészáros, 2002; Rossi et al., 2002). Low Γ components of a structured jet will give rise to EM counterparts to a NS-NS or BH-NS merger without the bright prompt γ-ray emission. Given a GW detection from a NS-NS or BH-NS merger, jet external shock EM counterparts will be able to reveal the jet structure.

In §3.2 we describe the jet structures considered in this chapter; in §3.3 we give details of the model used to estimate the observable emission at any inclination and show the results of our Monte Carlo; in §3.4 we discuss the various afterglow peak flux and peak time distributions; and in §3.5 we give concluding remarks and comment on the implications of these results for EM counterpart searches for GW detected compact stellar mergers.

3.2   Jet Structure

Jet structure refers to the opening angle and energy distribution within a relativistic jet; the jets in GRBs are usually assumed to have a simple 'top-hat' or homogeneous jet structure where the energy per unit solid angle ϵ and the bulk Lorentz factor Γ are uniform until a sharp edge at the jet opening angle. Structured jets, where the energy distribution varies with angle from the centre, have been discussed in relation to long GRBs; The structure is a result of the jet breaking out from the stellar envelope (e.g. Lyutikov & Blandford, 2002; Levinson & Eichler, 2003; Zhang et al., 2003, 2004; Lazzati & Begelman, 2005; Morsony et al., 2010; Pescalli et al., 2015). Alternatively, the structure can be a result of the jet formation mechanism (e.g. Vlahakis et al., 2003; van Putten & Levinson, 2003), where an accretion disc forms that can launch a relativistic jet, either by the Blandford-Znajek (BZ) mechanism (Blandford & Znajek, 1977) or neutrino annihilation (e.g. Popham et al., 1999). If the jet from a NS-NS or BH-NS merger propagates through an outflow at early times, then upon break-out some structure can be expected; similarly, if the jet is formed and accelerated by either BZ or neutrino annihilation, or a combination of both, then the structure can arise from the various components i.e. spine and sheath. Such jet structure could enhance the GW-GRB association probability (e.g. Jin et al., 2017; Kathirgamaraju et al., 2018).

Other than homogeneous jets, there are three alternative jet structures that are commonly discussed (e.g. Granot et al., 2002; Wei & Jin, 2003; Panaitescu, 2005):

(i) A two-component or spine and sheath jet; a fast, narrow core and a slower, wider sheath (e.g. Vlahakis et al., 2003; Peng et al., 2005; Jin et al., 2007). Also see Barkov & Pozanenko (2011) where the wider component is faster. Alternatively, baryon loading of the jet edges where a structured magnetic field prevents charged baryon drift into the jet core, will create a jet with uniform energy but a

wider low Γ component (Lei et al., 2013). The general two-component jet ϵ and Γ follow

$$\epsilon(\theta) = \begin{cases} \epsilon_c & \theta < \theta_c, \\ \epsilon_s & \theta > \theta_c, \end{cases} \qquad \Gamma(\theta) = \begin{cases} \Gamma_c & \theta < \theta_c, \\ \Gamma_s & \theta > \theta_c, \end{cases} \tag{3.1}$$

where the subscript c indicates the jet core parameter, and the subscript s indicates the uniform sheath parameter.

(ii) A structured jet where the energy and Lorentz factor are a function of the jet angle outside a uniform core (e.g. Zhang & Mészáros, 2002; Rossi et al., 2002, 2004; Kumar & Granot, 2003). The jet ϵ and Γ follow

$$\epsilon(\theta) = \begin{cases} \epsilon_c & \theta < \theta_c, \\ \epsilon_c \left(\frac{\theta}{\theta_c}\right)^{-k_e} & \theta > \theta_c, \end{cases} \qquad \Gamma(\theta) = \begin{cases} \Gamma_c & \theta < \theta_c, \\ \Gamma_c \left(\frac{\theta}{\theta_c}\right)^{-k_\Gamma} & \theta > \theta_c, \end{cases} \tag{3.2}$$

where θ is the angle from the jet axis, and we assume uniform baryon loading where $k_e = k_\Gamma = k \geq 0$.

(iii) A Gaussian jet (e.g. Kumar & Granot, 2003; Zhang & Mészáros, 2004; Rossi et al., 2004). The jet ϵ and Γ follow

$$\epsilon(\theta) = \epsilon_c e^{-\left(\theta^2/2\theta_c^2\right)}, \qquad \Gamma(\theta) = \Gamma_c e^{-\left(\theta^2/2\theta_c^2\right)}. \tag{3.3}$$

In all cases $\theta < \theta_j$, where θ_j is the maximum jet half opening angle. The existence of a jet edge is motivated by numerical simulations of compact stellar mergers (e.g. Rezzolla et al., 2011) where resistive-magnetohydrodynamics simulations result in a jet-like magnetic structure with a half-opening angle of $\sim 25°$ (Dionysopoulou et al., 2015). The jets are assumed to be symmetric about the central axis. Observed emission from the various components of a jet depends on the viewing angle $\theta_{\rm obs}$, measured from

the jet axis.

3.3 Method and Results

The jet energy dissipated by internal processes (e.g. Rees & Meszaros, 1994; Zhang & Yan, 2011) is radiated as γ-rays via the synchrotron process. The radius of this internal dissipation from the central engine can be estimated using the minimum variability timescale of the prompt emission, typically $\delta t \sim 0.1$ s (Nakar & Piran, 2002),

$$R_\gamma \simeq \Gamma^2 c \delta t \simeq 3 \times 10^{13} \delta t_{-1} \Gamma_2^2 \quad \text{cm}, \tag{3.4}$$

where c is the speed of light, $\delta t_{-1} = \delta t / 0.1$ s and $\Gamma_2 = \Gamma/100$.

The optical depth τ of the relativistic jet plasma is less than unity at radii greater than the photospheric radius $R_\star$. A conservative estimate for the minimum photospheric radius can be made by considering the electrons that accompany baryons in the jet. By considering the scattering of photons by these electrons the optical depth can be estimated (e.g. Lithwick & Sari, 2001). At a radius R the optical depth would be $\tau = \sigma_T E / \left(4\pi R^2 m_p c^2 \Gamma\right)$, where σ_T is the Thomson cross-section, $E = 4\pi\epsilon$ is the isotropic equivalent blast energy, and m_p is the mass of a proton. The radius where $\tau = 1$ is the photospheric radius

$$R_\star \simeq 6 \times 10^{13} E_{52}^{1/2} \Gamma_2^{-1/2} \quad \text{cm}, \tag{3.5}$$

where $E_{52} = E/10^{52}$ erg.

For a jet element with low Γ the initial dissipation happens well inside the photosphere; due to the relativistic beaming effect the dynamics and emission for the element can be evaluated in the spherical model with isotropic equivalent energy $4\pi\epsilon$ and

Γ. The γ-rays of the prompt emission are injected into an optically thick medium and the photons can remain trapped. The thermal energy of these trapped photons will be converted back to jet kinetic energy (Kobayashi & Sari, 2001; Kobayashi et al., 2002) and the prompt γ-rays from this jet region would be suppressed. For an observer looking 'on-axis' at such a region, all the prompt emission could be suppressed, resulting in a failed GRB (Rossi et al., 2002).

For γ-rays injected below the photosphere, the energy density is adiabatically cooled until the photons de-couple at the photospheric radius. The decoupling/emission time for these photons will be delayed from the dissipation or energy injection time t_0. Dissipation occurs during the coasting phase of the jet where Γ is constant and temperatures are sub-relativistic (Piran et al., 1993). As the energy density e evolves as $e \propto R^{-8/3}$, and the injected luminosity evolves as $L_\gamma \Delta / c \propto e R^2 \Delta \Gamma^2$, where L_γ is the injected γ-ray luminosity and Δ is the shell width, the emitted γ-ray luminosity at the photosphere $L_{\gamma,p}$ will be

$$L_{\gamma,p} \simeq L_\gamma (R_\star / R_\gamma)^{-2/3} \quad \text{erg s}^{-1}. \tag{3.6}$$

Additional to the adiabatic cooling, the prompt photons will be Compton downscattered and thermalized; the efficiency of the thermalization depends on the depth below the photosphere and therefore the optical depth (Pe'er et al., 2005; Thompson et al., 2007). The high energy spectrum will steepen and pair-production will determine a maximum spectral energy. The low energy spectral slope will steepen due to Compton scatterings as the thermalization becomes more efficient.

A relativistic jet propagating into an ambient medium will decelerate when the swept-up mass is equivalent to M_0/Γ, where $M_0 = 4\pi\epsilon/\Gamma$ is the explosion rest mass. A forward and reverse shock form and synchrotron radiation produces the observed

afterglow of GRBs (e.g. Rees & Meszaros, 1992; Mészáros & Rees, 1997; Kobayashi et al., 1999; Sari & Piran, 1999). The deceleration radius is $R_d \propto l/\Gamma^{2/3}$ where l is the Sedov length $l = (3E/4\pi m_p c^2 n)^{1/3}$. The observed deceleration time is then $t_d \propto E^{1/3} n^{-1/3} \Gamma^{-8/3}$ (Sari & Piran, 1995).

A reverse shock will propagate through the ejecta from the central engine at the beginning of the decelerating blastwave phase. The reverse shock contains energy comparable to the forward shock but due to a higher mass, the peak frequency is lower by a factor $\sim \Gamma^2$ (Kobayashi & Zhang, 2003). High polarization measurements in the afterglow of long GRBs suggests magnetized jets (Steele et al., 2009; Mundell et al., 2013). These observations still support a baryonic jet rather than a Poynting flux dominated jet, although a strong magnetic field can suppress the reverse shock. The reverse shock emission associated with short GRBs is rarely observed, either due to the early time of the peak, the typical frequency being well below optical, or due to magnetic suppression. We consider only the forward shock emission in this analysis.

3.3.1 Numerical Model

Jet parameters used throughout this chapter are; bulk Lorentz factor $\Gamma = 100$, ambient number density $n = 0.1$ cm^{-3}, microphysical parameters $\varepsilon_B = 0.01$, $\varepsilon_e = 0.1$, γ-ray efficiency $\eta = 0.1$, and minimum variability timescale $\delta t = 0.1$ s; the isotropic equivalent jet kinetic energy is $E_k = E_{iso}(1-\eta)$. We have used an isotropic equivalent blast energy of $E_{iso} = 4\pi\epsilon_c = 2 \times 10^{52}$ erg s^{-1}; this value is taken from the peak of the $E_{\gamma,iso}$ distribution in Fong et al. (2015), and assuming our γ-ray efficiency. The blast energy value is consistent with that found for jets from mergers by Shapiro (2017) and for the break-point in the luminosity function for short GRBs found by Wanderman & Piran (2015).

To estimate the observed intensity of the emission from a relativistic source at a

generic viewing angle, we consider the Lorentz invariant quantity I_ν/ν^3, where I_ν is the specific intensity and ν the frequency (Rybicki & Lightman, 1979). As $\nu = \delta \, \nu'$, where $\delta = [\Gamma(1 - \beta\cos\alpha)]^{-1}$ is the relativistic Doppler factor, $\Gamma = (1 - \beta^2)^{-1/2}$ the bulk Lorentz factor and β the velocity as a fraction of the speed of light, α the inclination to the line of sight of the bulk motion; then $I_\nu = I'_{\nu'}\delta^3$ where primed quantities are in the co-moving frame. By considering the observed on-axis emission, the specific flux to an off-axis observer will be a factor a^3 times the on-axis value, where $a = \delta(\alpha)/\delta(\alpha = 0) < 1$, i.e. $F_\nu(t, \alpha) = a^3 F_{\nu/a}(at, \alpha = 0)$ for a point source (Granot et al., 2002).

We model the prompt and afterglow emission from compact stellar merger jets by dividing the jet structure into $N \times M$ segments defined using spherical co-ordinates; the angle from the jet central axis is defined as $0 < \theta_i < \theta_j$ and the rotation around the jet central axis as $0 < \phi_k < 2\pi$. A segment has an opening angle of $\Delta\theta = \theta_j/N$ and an angular width $\Delta\phi = 2\pi/M$. The normal of each segment surface is θ_i from the central axis, where $\theta_i = (i - 1/2)\Delta\theta$, and i is an integer in the range $1 \le i \le N$. Similarly, the rotation position is $\phi_k = (k - 1/2)\Delta\phi$, where k is an integer in the range $1 \le k \le M$.

A segment has a bulk Lorentz factor and energy consistent with the jet structure model used; where for the jet structure models considered here, $\theta << \theta_c$ (i.e. the segment next to the jet axis) is used to normalize the energy distribution. Each segment has an energy per unit solid angle $\epsilon_{i,k}$ and a bulk Lorentz factor $\Gamma_{i,k}$. The energy dissipated as γ-rays at the radius $R_\gamma \propto \Gamma_{i,k}^2$ is $L_{\gamma,i,k} \sim 4\pi\eta \, \epsilon_{i,k}/t_{\rm in}$, where $t_{\rm in}$ is the energy injection timescale i.e. the pulse duration of γ-ray emission from a segment. We assume that $t_{\rm in} \equiv \delta t$; short GRBs often have multiple pulses, and in such a case the duration of the prompt emission is longer than the variability timescale $t_{\rm in} > \delta t$, the choice of $t_{\rm in} = \delta t$ results in bright GRBs and it gives conservative estimates for the

orphan afterglow rates. The energy dissipated by each segment is then $t_{\rm in} L_{\gamma,i,k} \Omega_{i,k}/4\pi$.

Prompt emission: The $EF_E \equiv \nu F_\nu$ spectrum for the injected photons is assumed to be a broken power-law that peaks at E_p with a spectral index of 1.5 below the peak and -0.25 above the peak. The spectral peak follows the $L_\gamma - E_p$ relation $E_{p,i,k} \sim 300 \, (L_{\gamma,i,k}/10^{52} \, {\rm erg})^{2/5}$ keV (Yonetoku et al., 2004; Ghirlanda et al., 2009; Zhang et al., 2012), where $L_{\gamma,i,k}$ is the isotropic equivalent γ-ray energy in the segment. For each segment the optical depth at R_γ is $\tau_{i,k} = (R_\star/R_\gamma)^2$; if $\tau_{i,k} > 1$ then the photons will be coupled to the jet plasma out to a radius $R_\star$ when $\tau_{i,k} = 1$ (Beloborodov, 2011; Hascoët et al., 2014; Lamb & Kobayashi, 2016). For cases where $\tau_{i,k} > 1$ at R_γ, the photon energy will be adiabatically cooled as $L_{\gamma,i,k}\tau_{i,k}^{-1/3}$; and the spectral peak energy will similarly reduce by a factor $\tau_{i,k}^{-1/3}$. The condition for efficient thermalization is, $\tau_{i,k} \geq m_e c^2/k_B T_{BB}$ (Pe'er et al., 2005; Thompson et al., 2007) where m_e is the mass of an electron, k_B is the Boltzmann constant, and the electron blackbody temperature $T_{BB} = (L_{\gamma,i,k}/4\pi R_\gamma^2 \Gamma_{i,k}^2 c \, a_c)^{1/4}$, where a_c is the radiation constant. If this condition is met then the spectral peak energy is given by $\sim 3k_B T_{BB}$ and the spectrum is exponentially suppressed above this energy. If thermalization is not efficient, then the maximum spectral energy is limited by pair-production; a cut-off in spectral energy occurs at $511(\Gamma_{i,k}/\tau_{i,k})$ keV.

For each segment, the luminosity and timescales for an on-axis observer are determined using the fireball model. The on-axis luminosity and time are corrected for the angle from the segment to the observer's line-of-sight. The emission time t_e for each segment depends on the point at which the photons decouple from the plasma. For segments where $\tau_{i,k} \leq 1$ this occurs at t_0; for segments where $\tau_{i,k} > 1$ then the emission is delayed so $t_e(\alpha = 0) = t_0 + (R_\star - R_\gamma)/2\Gamma_{i,k}^2 c$. For an observer at $\theta_{\rm obs}$ and $\phi_{\rm obs}$, the angle is $\alpha_{i,k}$. The emission time for segments at an angle $\alpha_{i,k}$ is delayed, so $t_e(\alpha) = a^{-1} t_e(\alpha = 0)$. Since the dissipated energy is radiated over an area $D_L^2 \Omega_{{\rm e},i,k}$,

the on-axis flux is given by,

$$F_{\nu,i,k}(t, \alpha = 0) = \frac{L_{\nu,i,k}}{4\pi D_L^2} \frac{\Omega_{i,k}}{\Omega_{e,i,k}}, \qquad (3.7)$$

where $\Omega_{e,i,k} = \max[\Omega_{i,k}, \Omega_{\Gamma,i,k}]$; and $\Omega_{\Gamma,i,k}(t_{i,k}) = 2\pi(1 - \cos 1/\Gamma_{i,k})$ is the beaming solid angle defined by the instantaneous segment bulk Lorentz factor. Similarly, the frequency of the emission is lowered, and the duration will be longer, by the factor a. The flux from each segment for an off-axis observer is given by,

$$F_{\nu,i,k}(t, \alpha_{i,k}) = a^3 \, F_{\nu/a,i,k}(at, \alpha = 0) \, \cos \alpha_{i,k}, \qquad (3.8)$$

where $\cos \alpha_{i,k}$ is the correction for the emission area projection (Salmonson, 2003). The spectral peak is normalized as the value integrated between 1 keV and 10 MeV giving $L_{\gamma,i,k}$. The prompt emission is then the sum of each segment's emission in a time bin between t_0 and the maximum emission time $a^{-1}(t_e + t_{in})$. The burst is detected if the number of photons at the detector is > 0.2 ph s^{-1} cm^{-2} in the *Swift* Burst Alert Telescope (BAT) band, 15-150 keV (Band, 2006).

Afterglow emission: Jet energy that is not radiated away by the prompt emission drives a relativistic outflow into the interstellar medium. The kinetic energy per unit solid angle of a jet segment is $\epsilon_{k,i,k} = \epsilon_{i,k} - t_{in}L_{\gamma,i,k}/4\pi$. We assume no sideways expansion so each jet segment evolves independently (van Eerten & MacFadyen, 2012); the lateral expansion of homogeneous and structured jets is discussed by Salmonson (2003). The value of $\Gamma_{i,k}$ is considered constant, $\Gamma_{0,i,k}$, before the deceleration radius R_d and will evolve as $\Gamma_{0,i,k}(R_{i,k}/R_d)^{-3/2}$ with distance $R_{i,k}$ when $R_{i,k} > R_d$. The on-axis flux from each segment at a given observer time t can be evaluated by using the standard synchrotron shock model. The on-axis characteristic frequency ν_m and cooling frequency ν_c are calculated in the same way as discussed in Sari et al.

(1998). The peak flux of the afterglow is obtained by considering the total number of electrons in the segment $N_e = nR^3\Omega_{i,k}/3$. The total energy per unit time per unit frequency emitted by these electrons is proportional to $N_e \propto \Omega_{i,k}$ and is distributed over an area $D_L^2\Omega_{e,i,k}$ at a distance D_L from the source. Since the on-axis peak flux density $F_{\nu,\mathrm{max}}$ is proportional to $\Omega_{i,k}/\Omega_{e,i,k}$, we obtain the on-axis flux from a segment $F_{\nu,i,k}(t, \alpha = 0) = F_\nu(t)\,\Omega_{i,k}/\Omega_{e,i,k}$, where $F_\nu(t)$ indicates the flux from a blast wave with the isotropic energy $4\pi\epsilon_{\mathrm{k},i,k}$ (Sari et al., 1998, 1999). For an off-axis observer the flux from a segment is given by equation 3.8; the sum of flux from each segment at time t gives a total afterglow light-curve. Using this model the emission from a decelerating jet can be estimated at various observation angles.

3.3.2 Homogeneous Jets: approximations

Here we give an approximation for the peak flux and peak time of an orphan afterglow from a homogeneous jet; the estimates will be compared with the numerical results. The afterglow emission from a decelerating relativistic collimated blastwave is beamed within the angle $\theta_j + 1/\Gamma$. For observers outside this angle the emission becomes much fainter as the inclination of the system increases. Assuming slow cooling with $\nu_m < \nu < \nu_c$, and the Doppler correction for an off-axis observer, the observed peak flux is approximately,

$$F_p = C(p)\, f(\theta_{\mathrm{obs}}, \theta_j)\, [\theta_{\mathrm{obs}} - \theta_j]^{2(1-p)}\, \nu^{(1-p)/2}\, E_{\mathrm{k}}\, n^{(1+p)/4}\, \varepsilon_B^{(1+p)/4}\, \varepsilon_e^{p-1}\, D^{-2}\ \ \mathrm{erg\ s^{-1}\ cm^{-2}\ Hz^{-1}},$$

$$(3.9)$$

where $C(p)$ is a constant that depends on the particle index p and all the relevant physical parameters[1], $f(\theta_{\mathrm{obs}}, \theta_j)$ accounts for the jet opening angle θ_j, viewing angle

---

[1] $C(p) = (32\pi)^{(1+p)/4}\, (12\pi)^{-1}\, (2\pi)^{(1-p)/2}\, m_p^{(5p-7)/4}\, m_e^{(5-3p)/2}\, q_e^{(p-3)/2}\, c\, \sigma_T\, [(2p - 4)/(7 - p)]^{p-1}\, [(7 - p)/(5 + p)]^{(5+p)/2}$, where m_e is the electron mass, c the speed of light, σ_T the Thomson cross-section, q_e an electron charge, m_p the proton mass

$\theta_{\rm obs}$ and the relativistic beaming, and ν is the observed frequency. The factor $f(\theta_{\rm obs}, \theta_j)$ is,

$$f(\theta_{\rm obs}, \theta_j) = \cos(\theta_{\rm obs} - \theta_j) \left[\frac{1 - \cos\theta_j}{1 - \cos([(7-p)/(2p-2)]^{1/2} \theta_{\rm obs})} \right], \quad (3.10)$$

where $\cos(\theta_{\rm obs} - \theta_j)$ corrects for the surface area projection, and the second term accounts for the emission solid-angle.

For $p = 2.5$, the peak flux is,

$$F_p \sim 2 \times 10^{-3} f(\theta_{\rm obs}, \theta_j) [\theta_{\rm obs} - \theta_j]^{-3} \nu_{14}^{-3/4} E_{52} n_{-1}^{7/8} \varepsilon_{B,-2}^{7/8} \varepsilon_{e,-1}^{3/2} D_{\rm 200Mpc}^{-2} \quad \text{mJy}, \tag{3.11}$$

where we use the convention $N_x = N/10^x$. Angles are in radians, frequency is in Hz, E is the isotropic jet kinetic energy $E_{\rm k}$ in erg, ambient number density n in cm^{-3}, and the distance is normalized to 200 Mpc.

The peak flux occurs at a time given by,

$$t_p \sim 195 \left[\frac{(5+p)(7-p)^{1/3}}{(p-1)^{4/3}} \right] [\theta_{\rm obs} - \theta_j]^{8/3} n_{-1}^{-1/3} E_{52}^{1/3} \quad \text{days}. \tag{3.12}$$

The expressions in equation 3.11 and 3.12 give an approximation for the peak flux and time from an off-axis orphan afterglow to a relativistic jet with homogeneous structure in a uniform density ambient medium.

3.3.3 Monte Carlo Results

Given a GW detection from a NS-NS or BH-NS merger, the fraction of events that have detectable EM counterparts from the relativistic jet depends on the jet structure and opening angle. Using a Monte Carlo method we estimate the fraction of merger
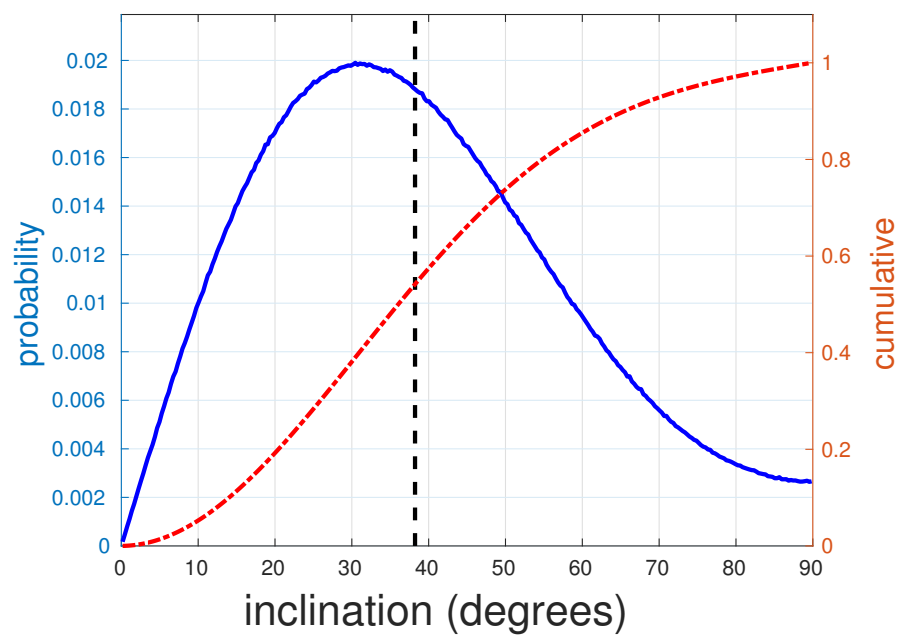
Figure 3.1: By considering the GW strain from a merger as a function of inclination the distribution of system inclinations can be determined. For all GW detected mergers at a fraction of the maximum detectable luminosity distance the probabilty of a system being inclined at given angle is shown with the blue solid line. The mean system inclination for this distribution is the dashed black line. The red dash-dotted line is the cumulative distribution.

jets, with a given jet structure, that result in EM counterparts with r-band magnitude $m_r \leq 21$. A population of 10^5 mergers within the face-on detection limit for a NS-NS merger by advanced LIGO ~ 300 Mpc is generated. The luminosity distance D_L to a merger is randomly determined using the redshift distribution for non-collapsar short GRBs found by Wanderman & Piran (2015). The inclination i follows a random isotropic distibution. By considering that GW signals are stronger along the system rotation axis for binary mergers with a random orientation, the average inclination for a distribution of GW detected mergers can be determined. Mergers with a GW strain $h \propto (h_+^2 + h_\times^2)^{1/2}/D_L$, where $h_+ \propto 1 + \cos^2 i$ and $h_\times \propto 2\cos i$, are GW detected if $h > h_c$, the limiting detectable strain (e.g. Kochanek & Piran, 1993; Lamb & Kobayashi, 2016); for a more detailed investigation of the detectable gravitational waves from compact binary mergers see Kobayashi & Mészáros (2003); Nissanke et al. (2010); Schutz (2011). The distribution of merger inclinations is shown in figure 3.1; the peak of the probability distribution is $i \sim 31°$, and the mean $\langle i \rangle \sim 38°$. The blue solid line is the probability of a merger with a given inclination; the red dash-dotted line is the probability that a merger will have an inclination equal or less than a given value.

The peak magnitude for an observer at the mean GW detection inclination angle of $\sim 38°$ from a homogeneous jet depends on the half-opening angle of the jet. By considering a homogeneous jet with a constant isotropic equivalent blast energy, or a constant geometrically corrected jet energy, the peak magnitude of the orphan afterglow for an observer at 200 Mpc and $38°$ can be estimated. Using the isotropic equivalent energy $E_{\text{iso}} = 2 \times 10^{52}$ erg, or the geometrically corrected energy $E = E_{\text{iso}}\Omega/4\pi = 1.5 \times 10^{50}$ erg, giving E_{iso} for a $\theta_j = 10°$, the peak magnitude for jet half-opening angles $2° \leq \theta_j \leq 30°$ are shown in figure 3.2. The thick red line is for constant E_{iso}, and the thick blue dotted line for constant geometrically corrected

jet energy. Three optical bands are shown, *g*-, *r*-, and *i*-band and the equivalent peak macronova flux, black dashed line, for a NS-NS merger (Tanaka et al., 2014). BH-NS mergers would result in brighter macronova, $\sim 23.8,\ 23.2,\ 22.8$ respectively, although the ejecta in these cases is not isotropic. The macronova estimates should be considered as upper limits, for the adopted model, as the peak flux depends on the inclination where the brightest emission coincides with the polar axis (the jet axis) (Tanaka, 2016; Wollaeger et al., 2017); however, macronovae may be brighter than the adopted model i.e. Jin et al. (2016). The frequency dependence for the afterglow flux is shallower than that of a macronova which peaks sharply in the red to radio with a thermal spectrum and exponential decay at higher frequencies. The non-thermal spectrum of a GRB afterglow, where the higher frequency is typically $F_\nu \propto \nu^{-(p-1)/2}$ or $F_\nu \propto \nu^{-p/2}$ where $p \sim 2.5$, ensures that for an off-axis observer the afterglow is at a similar amplitude in a range of detection bands.

In figure 3.2 we see that the peak flux for an orphan afterglow viewed at $38°$ is brighter for homogeneous jets with wider jet half-opening angles. The point at which the peak flux for constant isotropic equivalent blast energy and constant geometrically corrected jet energy are equal indicates the normalization angle. For jets normalized to this value with narrower half-opening angles, the peak afterglows are brighter than the equivalent constant isotropic blast energy case; this is due to the jet having a higher energy density in these cases, and for jets wider than this normalization, a reduction in jet energy density is apparent. The shape of the curve is dominated by the effective angle to the jet for wide θ_j i.e. $(\theta_{\rm obs} - \theta_j)^{-3}$ (equation 3.11); and for narrower θ_j, by the fill factor i.e. the second part of the expression in equation 3.10. For a jet with a given opening angle, inclination, distance, and observation frequency the peak orphan afterglow flux is $F_p \propto E_{\rm k} n^{7/8} \varepsilon_B^{7/8} \varepsilon_e^{3/2}$. The degeneracy in ε_B and n can make determination of these parameters difficult, and the change in peak flux for a one order of
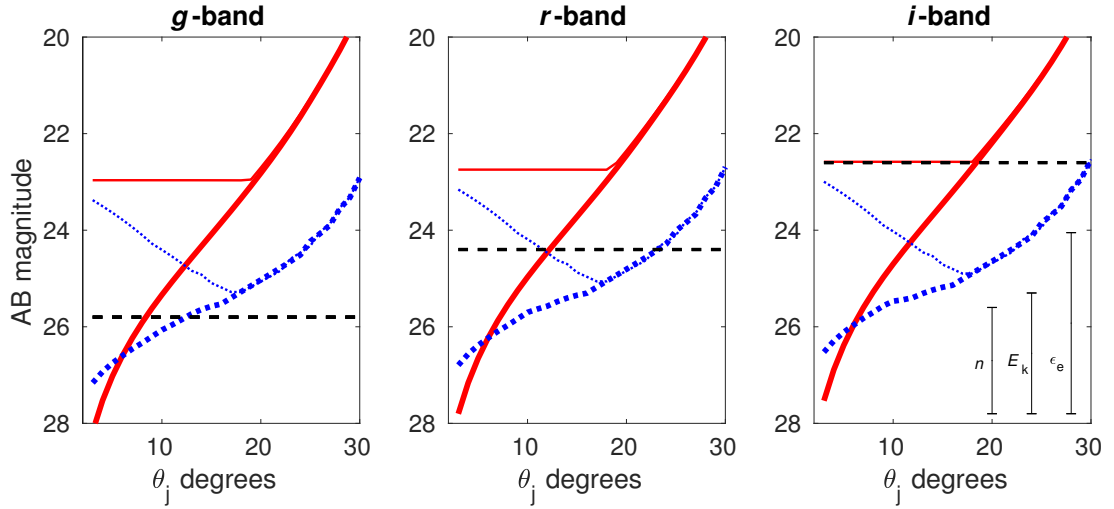
Figure 3.2: The peak magnitude for the off-axis afterglow at $38°$ from a homogeneous merger jet with opening angle θ_j at 200 Mpc. Red thick line indicates a jet with constant isotropic equivalent energy, $E_{\mathrm{iso}} = 2 \times 10^{52}$ erg, and the blue thick dashed line indicates a jet with constant geometrically corrected jet energy (normalized to a $\theta_j = 6°$ jet with $E_{\mathrm{iso}} = 2 \times 10^{52}$ erg). The thin lines indicate a two-component jet where θ_j defines the core angle (θ_c in equation 3.1) and the wider component extends to $30°$ (equivalent to θ_j described in §3.2). The energy and Lorentz factor of the wide component are fixed at 5% the core values. All jets have a core Lorentz factor of $\Gamma = 100$ and are in an ambient medium with a particle density of 0.1 cm^{-3}. The full sizes of the errorbars in the righthand panel indicate the magnitude of change in peak flux for a one order of magnitude change in the respective parameter (note that n is degenerate with ε_B). The black dashed horizontal lines indicate the peak macronova emission for a NS-NS merger; assuming isotropic emission from a soft equation-of-state model e.g. Tanaka et al. (2014) at 200 Mpc

magnitude change in any of these parameters is indicated by the length of the errorbars in the third panel. Short GRBs often occur in low-density environments, a reduction in n by an order of magnitude would result in a peak that is $\Delta m_{AB} \sim 2.2$ dimmer.

Within figure 3.2 the peak flux for the orphan afterglow of a two-component jet is shown as a thin red and a thin blue dotted line. In each case the wider jet structure extends to $30°$ (equivalent to θ_j in §3.2) with energy and Lorentz factor at 5% the value for the core region, defined by the x-axis in the figure. For the thin red line the jet has an isotropic equivalent blast energy for an on-axis observer $\theta_{\mathrm{obs}} < \theta_c$ of 2×10^{52} erg; the thin dotted blue line has a constant geometrically corrected jet energy normalized to a homogeneous jet with an opening angle of $6°$. As the two-component jet always has a wide sheath that extends to $30°$, beyond the core angle defined by θ_j on the plot x-axis, the peak flux for jets with a core narrower than $\sim 20°$ is constant and approaches the homogeneous jet case for half-opening angles wider than this. By considering equation 3.11 for two homogeneous jets, one with fixed energy and undefined θ_j and the second with $\theta_j = 30°$ and 5% the energy of the first, the θ_j for the more energetic jet that results in the same peak orphan afterglow for an observer at θ_{obs} is $\theta_j \sim \theta_{\mathrm{obs}} - 20^{1/3}(\theta_{\mathrm{obs}} - 30)$ degrees. The wide sheath with 5% of the core energy and Lorentz factor is the dominant contributer to the off-axis emission for jets with a core $\lesssim 20°$. Where the jet energy is fixed at the geometrically corrected value for a $6°$ homogeneous jet, the reduction in the energy content of the wider component as the core width is increased leads to a dimmer afterglow. When the off-axis emission from the jet core becomes brighter than the off-axis emission from the sheath, the peak off-axis flux follows the homogeneous jet. Two-component jets are described in §3.2 and their afterglows discussed below.

The Monte Carlo distribution of mergers for each structure model have identical values of the core opening angle $\theta_c = 6°$. Hydrodynamic simulations indicate a range

of jet core half-opening angles that are dependent on the initial conditions, $3° \lesssim \theta_c \lesssim$ $13°$ (Nagakura et al., 2014). The core value is significantly wider than the core values used in other structured jet models (e.g. Rossi et al., 2002; Salmonson, 2003). The two-component jet has ϵ_s and Γ_s at 5% of the core values, while the power-law jet has an index $k = 2$ for $\theta > \theta_c$. The effect of jet structure on the observed jet-break is discussed below. For the extended structure the minimum Γ is 2, and the maximum half-opening angle is $25°$, and all other parameters are as previously used.

Examples of the afterglow light-curves for each model from a jet at 200 Mpc and viewed at inclinations from $0°$ to $40°$, in $5°$ intervals, are shown in figure 3.3; each jet structure has 120×120 segments. The light curve produced using $N = M = 120$ in the model is identical for values of N, $M > 120$; where N, $M < 120$ the peak flux and time for afterglows are consistently reproduced although the shape of the early afterglow before the peak is inaccurate. Light curves for inclinations $i >> \theta_c$ are less sensitive to the choice of segment number, and N, $M \gtrsim 25$ reproduce well the higher resolution light curves. The blue lines indicate the afterglow for a *Swift*-detectable GRB, $\theta_{\text{obs}} \leq 10°$; the red dashed lines indicate the afterglow for a jet viewed within the half-opening angle but without a *Swift* detectable GRB, a failed-GRB, $\theta_{\text{obs}} \leq \theta_j$; the black dash-dotted lines indicate an off-axis orphan afterglow, $\theta_{\text{obs}} > \theta_j$. For the homogeneous jet, the analytic peak magnitude and time from equations 3.11 and 3.12 are shown as blue crosses; the analytic expressions overestimate the peak flux, and underestimate the peak time when $\theta_{\text{obs}} \lesssim 3\theta_j$. Additional light curves are shown in the top-left panel for an observer at $0°$ and $10°$, by blue dashed and black dotted lines respectively. Here the ambient number density is lower by a factor 10; for an on-axis observed afterglow, this parameter change results in a peak flux that is ~ 1.2 magnitudes fainter and for off-axis observed afterglow the peak flux is ~ 2.2 magnitudes fainter. A similar change in magnitude, $1.2 \lesssim \Delta m_r \lesssim 2.2$, is observed for all light
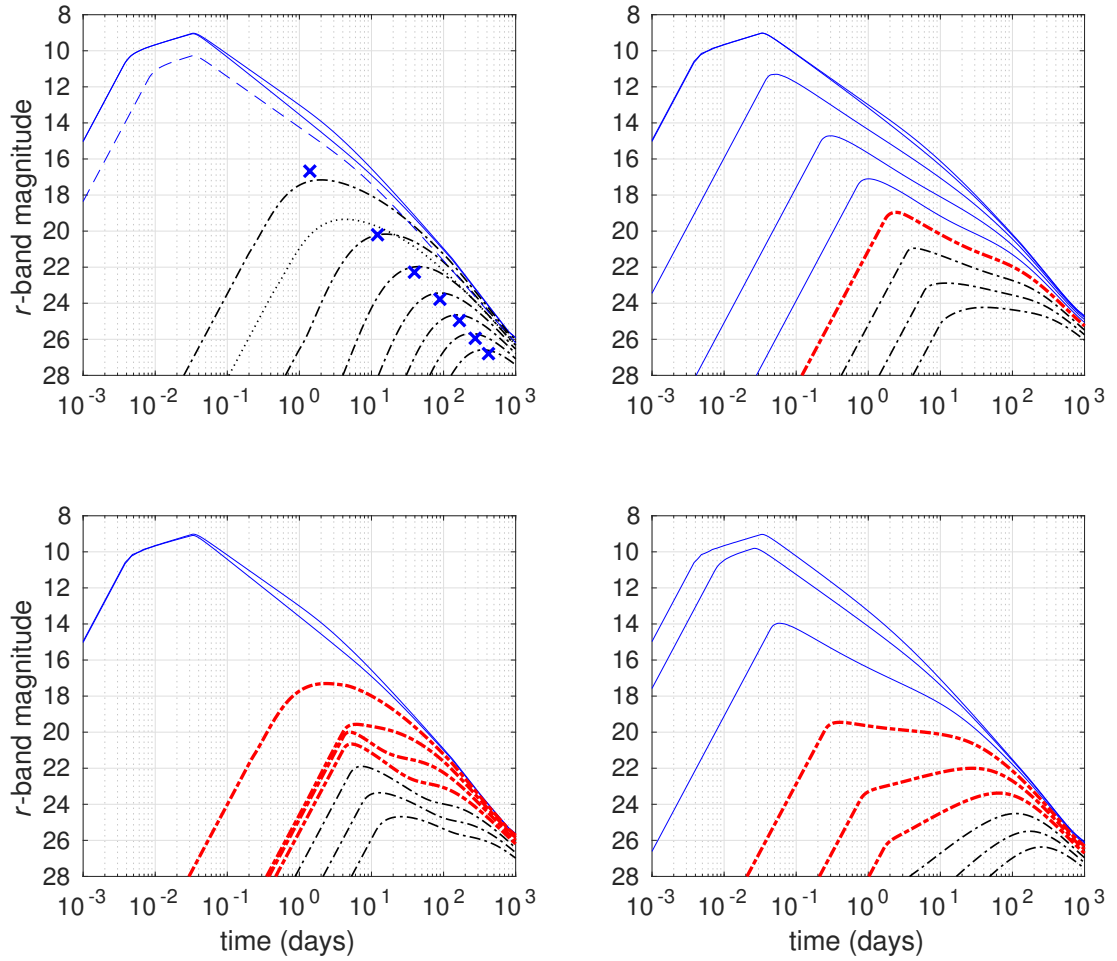
Figure 3.3: Afterglow *r*-band light curves for jets at 200 Mpc. Light curves are plotted for an observer at 5° increments in the range $0° \leq \theta_{\rm obs} \leq 40°$. The model values used in each case are: (top left) $\theta_c = \theta_j = 6°$ for the homogeneous jet; (bottom left) $\theta_c = 6°$ for the two-component jet where the second component extends to $\theta_j = 25°$ with 5% of the core energy and Lorentz factor; (top right) $\theta_c = 6°$ for the power-law jet with an index $k = 2$ for $\theta_c < \theta \leq 25°$; and (bottom right) $\theta_c = 6°$ for the Gaussian jet with a maximum $\theta_j = 25°$. Jets have an isotropic equivalent blast energy of 2×10^{52} erg, a bulk Lorentz factor $\Gamma = 100$, and an ambient medium density of $n = 0.1$. Blue lines indicate the afterglow of a GRB; red dashed lines indicate an on-axis orphan afterglow i.e. within the wider jet opening angle but with suppressed prompt emission; black dash-dotted lines indicate an off-axis orphan afterglow. The blue dashed and black dotted lines in the top left panel indicate the afterglow for an observer at 0° and 10° respectively where the ambient medium has a particle density $n = 0.01$ cm^{-3}; the change in magnitude for an 'on-axis' observer is $\Delta m_r \sim 1.2$, and for an 'off-axis' observer $\Delta m_r \sim 2.2$ for each order of magnitude change in the n parameter.

curves where the ambient density is lower by a factor 10.

The light-curves in figure 3.3 have afterglows which in each case are similar for an observer on the jet axis with respect to the deceleration time, peak flux, and peak time. The jet has a soft break that is determined by either the difference between the observation angle and the jet half-opening angle for a homogeneous jet, or the core angle for a jet with structure. A second break may be observed at later times, which is associated with the opening angle of the extended structure. A GRB afterglow for a homogeneous jet observed at the jet edge θ_j is half as bright and has a jet-break determined by the width of the jet $\sim 2\theta_j$; for the other structures, the afterglow characteristics depend on the local jet energetics ϵ and Γ parameters.

Light curves for the jet structure models tested show that, where no sideways expansion is assumed and the jet-break is caused by the increase in the beaming angle beyond the jet edge, the break seen in short GRB afterglows depends on the inclination. We expect a sharp break at very late times when the outflow becomes Newtonian, but this is not included in our model. Fong et al. (2015) list four short GRBs with measured half-opening angles $3° \lesssim \theta_j \lesssim 8°$, and a further seven with lower limits; the narrowest of these lower limits is $\gtrsim 4°$, and the widest $\gtrsim 25°$. The average θ_j for short GRBs can be inferred by assuming a maximum jet half-opening angle; $\bar{\theta}_j = 16°\,^{+11}_{-10}$ for $\theta_{\max} = 30°$, and $\bar{\theta}_j = 33°\,^{+38}_{-27}$ at the limit $\theta_{\max} = 90°$; alternatively, Ghirlanda et al. (2016) found the short GRB population to be consistent with a jet opening angle of $3 \leq \theta_j \leq 6°$. We use a $\theta_j = 6°$ for homogeneous jets, consistent with both estimates, and fix this as the core angle for jets with extended structure. In these examples the jet half-opening angle was inferred using $\Gamma^{-1}(t_j) \equiv \theta_j$. If the observed jet-break time t_j depends on inclination, as in our model for GRB afterglows, the break time cannot limit the full extent of jet structure. By assuming a range of jet parameters, the range of jet-break times can be reproduced by our model.

Additional features in the afterglow light-curves for jets with extended structure appear at wider angles. For our parameters, these appear where the prompt emission is suppressed and the afterglow would be from a failed-GRB. Afterglows for the two-component model at angles $\theta_{\mathrm{obs}} > \theta_c$ have an early peak flux and time determined by the local jet energy ϵ and Γ respectively; a late bump is due to emission contribution from the bright core, the time of the bump is determined by the inclination, with higher inclinations resulting in a later bump time. A similar feature can be seen in the power-law structured jet but as the energetics and Lorentz factor for the wider component are not uniform with angle, the early peak flux and time are unique. The afterglow for the Gaussian-structured jet at comparable angles is dominated by the bright core emission at late times. For orphan afterglows in each structured jet case, the early rise time and peak are due to the contribution from the wide extended structure; a more energetic wide component leads to a brighter and more pronounced peak, while for a less energetic wide component, the orphan afterglow is dominated by the core emission at later times. As the observation angle increases, the contribution from the various components becomes indistinguishable; here we only show orphan afterglows up to an observation angle of $40°$.

In all cases we have assumed uniform baryon loading; if the baryon loading is more efficient towards the edge of a jet then ϵ and Γ will not have the same distribution. If the structure in a jet is due to baryon loading only, then the energy will be uniform; the afterglow for the various viewing angles will be brighter than the equivalent shown here as the peak flux depands on the energy. The peak time for the afterglow will be later for lower-Γ components; the prompt emission will be similarly suppressed.
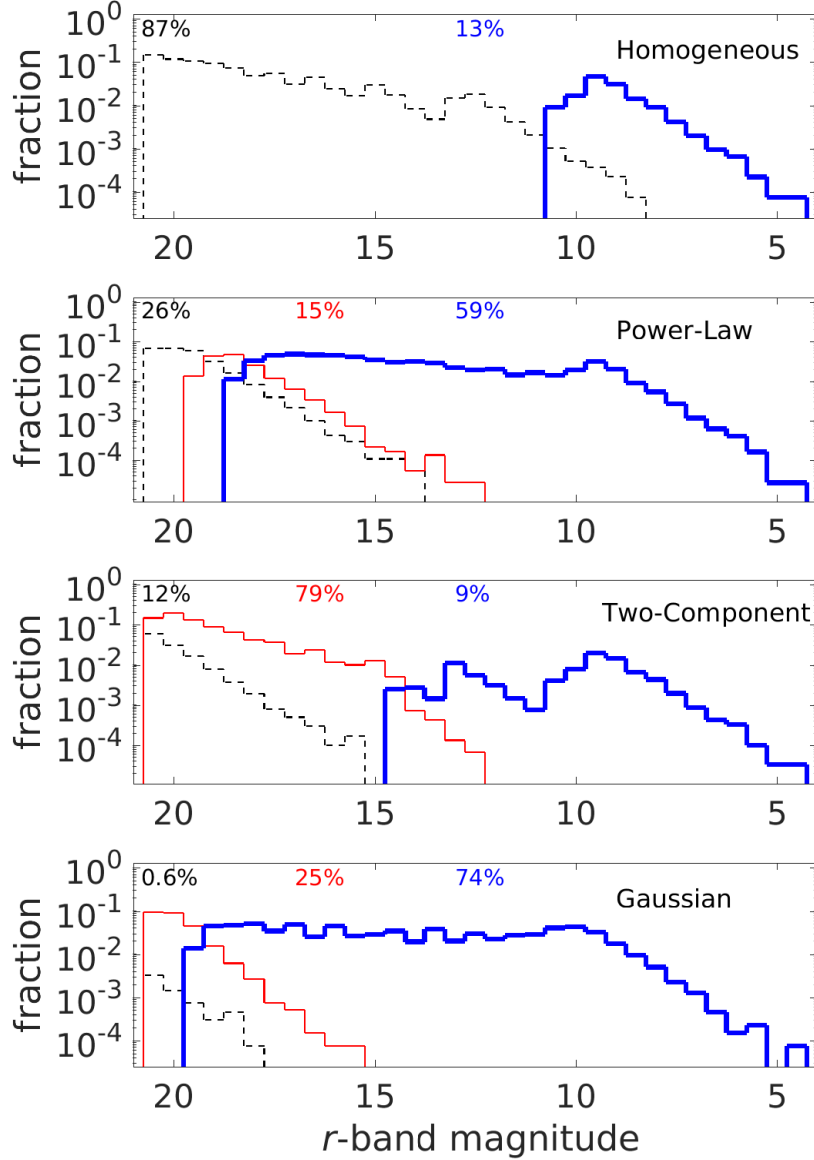
Figure 3.4: Peak magnitude for the afterglow brighter than 21 for a population of 10^5 GW detected mergers; the percentage of the total detected merger population for each type is: homogeneous jets 13.6%; power-law structured 36.9%; two-component 30.0%; and Gaussian 13.3%. The blue thick line histogram is a GRB afterglow, red thin line histogram is an on-axis orphan (failed GRB) afterglow $\theta_{\mathrm{obs}} < \theta_j$, and black dashed line is an off-axis orphan afterglow $\theta_{\mathrm{obs}} > \theta_j$. Percentages are the fraction of events brighter than magnitude 21 in each case.

3.4 Peak Flux/Time

The 10^5 Monte Carlo distribution has a randomly determined inclination and distance given a GW detection where the same distributions are used with each jet structure model. The afterglow from each jet structure model is evaluated at one degree intervals $0° \leq \theta_{\mathrm{obs}} \leq 90°$, and for efficiency, the model uses $N = 25$ and $M = 100$ ensuring jet structure is resolved. The peak magnitude for the light-curve that corresponds to the jet structure at the randomly determined inclination is then selected and scaled for the distance. A histogram of the peak magnitude for jet EM counterparts brighter than magnitude 21, for GW detected mergers $\lesssim 300$ Mpc is shown in figure 3.4; the thick blue line is a GRB afterglow, the thin red line is a failed-GRB orphan afterglow, and the black dashed line is an off-axis orphan afterglow. The fractions of each jet counterpart type i.e. GRB afterglow, failed GRB afterglow, orphan afterglow, of the total number of $m \leq 21$ events are shown.

In figure 3.4 the peak of the distribution for GRB afterglows is that for a face-on NS-NS merger at the maximum detection distance ~ 300 Mpc. The structured jets have an extended distribution to fainter magnitudes when compared with the homogeneous jets, which is due to the lower energetics for observers $\theta_c < \theta_{\mathrm{obs}}$. For the failed-GRB orphan afterglows from jets with structure, the distribution for power-law structured and Gaussian structured jets has a wide plateau for the peak magnitudes due to the non-uniform energetics of the wider jet component. The two-component jet structure has a uniform energy distribution in the wide component, which gives a single sharp peak to the failed-GRB orphan afterglows.

From the Monte Carlo analysis the fraction of afterglow counterparts brighter than magnitude 21 depend on the jet structure model. For jets with extended structure to the limit of 25°, we show that compared to a population of homogeneous jets with $\theta_j = 6°$ the fraction of bright jet counterparts is higher for two-component jets (equation

3.1) and power-law structured-jets (equation 3.2). GRB-producing jets result in bright afterglows, with peak *r*-band magnitude $20 \gtrsim m_r \gtrsim 5$. Orphan afterglows brighter than magnitude 21, both from failed-GRBs and off-axis observations, are produced in $\sim 12\%$ of cases for homogeneous jets; $\sim 27\%$ for two-component jets; $\sim 15\%$ of cases for power-law structured-jets; and $\sim 3.4\%$ for Gaussian jets. The brightest of these counterparts is $m_r \gtrsim 8$. The peak brightness depends on the jet kinetic energy and the fraction of events depends on the jet opening angle. For mergers that are close by, the prompt photon flux at angles $> \theta_c$ can be above the detection threshold; for two-component jets, where the ϵ distribution is generally flat in this region, a noticable fraction of the counterparts will accompany faint GRBs. This can be seen by three peaks in the flux distribution for GRB afterglows.

The total fraction of EM counterparts brighter than magnitude 21 from the jet of GW-detected mergers depends on the jet structure: for homogeneous jets we find $\sim 13.6\%$; for two-component jets $\sim 30\%$; for structured jets the fraction is $\sim 37\%$; and Gaussian jets $\sim 13\%$. The fractions for an isotropic distribution to a distance of ~ 200 Mpc, the maximum for edge-on NS-NS GW detection, are $\sim 4.5\%, 11.8\%, 13.5\%,$ and 4.1% respectively (homogeneous, two-component, power-law, and Gaussian); here GRB afterglows account for $\sim 4.4\%, 3.4\%, 43.7\%,$ and 53.7% of the $m_r \leq 21$ counterpart fraction. In all cases we consider the same structure parameters. The fraction of events brighter than magnitude 10, in each case, is dominated by GRB afterglows.

A corresponding histogram showing the peak time for each of the counterpart distributions is shown in figure 3.5. The colour and line style are the same as figure 3.4. The peak time distribution shows that for structured jets the GRB afterglows have a broader range of peak times than the homogeneous jet case. This is due to the non-uniform distribution of Lorentz factor for GRB producing jet components $> \theta_c$.

The jet counterparts $m_r \leq 21$, to GW detected mergers, typically peak at $t_p \lesssim 100$
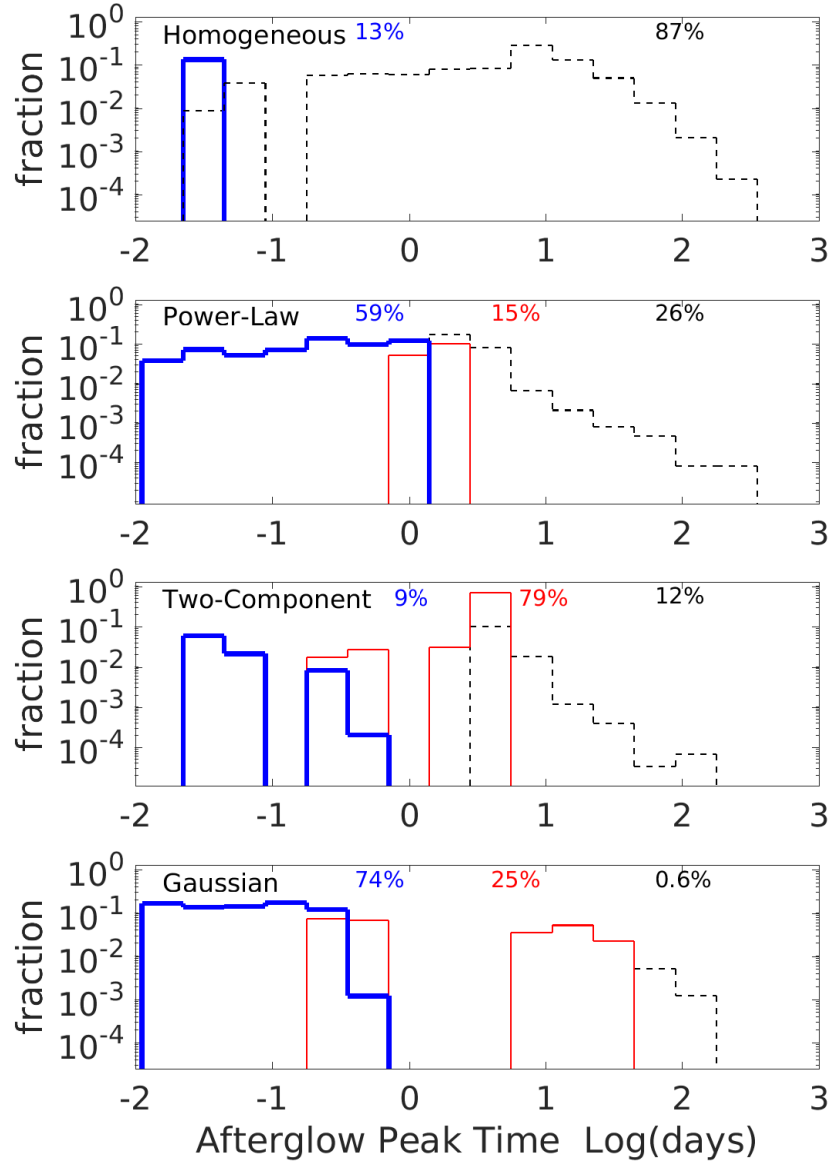
Figure 3.5: Peak time for the afterglows brighter than 21 for a population of 10^5 GW detected mergers. Blue thick line histogram is a GRB afterglow; red thin line histogram is an on-axis orphan (failed GRB) afterglow $\theta_{\rm obs} < \theta_j$; black dashed line is an off-axis orphan afterglow $\theta_{\rm obs} > \theta_j$. Percentages are the fraction of events brighter than magnitude 21 in each case.

days. The brightest counterparts peak very early, $0.01 \lesssim t_p \lesssim 0.1$ days; orphan afterglows for a homogeneous jet peak typically at $t_p \sim 10$ days; failed-GRB and off-axis orphan afterglows typically peak at $t_p \sim 1$ day for power-law structured-jets and two-component jets; and Gaussian jets exhibit a bimodal distribution, due to the wide low Γ extended jet structure, that peaks at $t_p \sim 0.25$ days and $t_p \sim 20$ days. The bimodal feature in the GRB afterglow distribution for two-component jets is due to the stepped boundary between the spine and sheath; detectable GRBs are produced outside of the core region $\theta_c = 6°$. These GRBs near the core edge have significantly lower Γ than those observed within the core angle, which the second split in peak times for the two-component jets is due to the dominance of the off-axis core emission over the on-axis sheath emission, where on-axis emission will peak earlier. The apparent bimodality of the bright orphan afterglows for a homogeneous jet is a result of the sharp jet edge and uniformity of θ_j for the population as well as the numerical precision for changes of inclination $< 1°$; the bimodality would vanish for a population of jets with a distribution of θ_j or higher numerical resolution.

3.5 Conclusions

For jets from compact-stellar-mergers with a homogeneous structure we have shown that wide opening angles $\theta_j \gtrsim 10°$ result in optical orphan afterglows, when viewed at the average GW detected merger inclination of $\sim 38°$, that are brighter than the estimates for the equivalent peak flux from macronovae; note that this depends on the ambient density and jet energetics. We show that where jets have an extended structure to a limit of $\theta_j = 25°$, similar to the limit predicted by numerical simulations, the fraction of EM counterparts brighter than magnitude 21 can be 2-3 times that from a narrower homogeneous jet population. GW triggered searches for EM counterparts

could reveal a hidden population of failed-GRB orphan afterglows associated with wider jet structure where the low energetics and Lorentz factor could suppress the prompt γ-rays; we show light curve features in orphan afterglows that could indicate the presence of extended jet structure. Jet EM counterparts to GW detected NS-NS or BH-NS mergers will reveal the jet structure, Lorentz-distribution, and opening angle for short GRB jets.

We assumed a jet central axis observed isotropic blast energy of 2×10^{52} erg s^{-1}. A jet with a higher blast energy will result in an afterglow with a brighter peak magnitude. The various structured jet models naturally predict a range in observed total energetics that have a maximum at 2×10^{52} erg s^{-1}. The observed energetics of a jet, inferred from the prompt fluence and the peak of the afterglow, will appear lower for GRB afterglows seen at the jet edge for homogeneous jets or outside the jet core for jets with a variable structure. Jets viewed at inclinations where most of the prompt emission is suppressed may appear as X-ray flashes or low-luminosity GRBs; in both cases the afterglow will appear dimmer and peak at later times than for the on-axis afterglow. For jets observed at inclinations comparable to the point where γ-rays become suppressed, the duration of the prompt emission will be longer due to the delayed emission of the prompt photons from the low Γ segments; the spectra will have a strong thermal contribution. The longer duration of such a GRB could result in misclassification as $T_{90} \gtrsim 2$ s.

The rate of NS-NS mergers within the advanced LIGO detection volume is not known but values range from $0.2 - 200$ yr^{-1} (e.g. Aasi et al., 2013; Abbott et al., 2016a). Metzger & Berger (2012) made an estimate for the *Swift*-detected short GRB with redshift rate within this volume for NS-NS, of 0.03 yr^{-1}; similarly, Coward et al. (2012); Petrillo et al. (2013); Siellez et al. (2014) found a consistent rate for GW-GRBs within the aLIGO volume, although the limits vary, and Fong et al. (2015) found

Table 3.1: The GW-detected NS-NS rate given an all-sky GRB rate, within the LIGO detection limit, $0.27 \leq R_{NS-NS} \leq 1.1$ yr^{-1}. The first column showns the jet structure model, the second column gives the fraction of GRBs in the Monte-Carlo analysis, the third column shows the fraction of the Monte-Carlo population that resulted in an optical counterpart $m_{AB} \leq 21$, the fourth column shows the fraction of these that are associated with a *Swift*-detectable GRB, and the last column gives the predicted rate for GW-detected NS-NS mergers.

Jet Model	f_{GRBs}	$f_{m_{AB} \leq 21}$	$f_{\leq 21, \text{GRBs}}$	R_{NS-NS} yr^{-1}
Homogeneous	1.7%	13%	13%	$15.9 - 63.5$
Two-component	2.7%	30%	9%	$10 - 40$
Power-law	22%	37%	59%	$1.2 - 4.9$
Gaussian	9.6%	13%	74%	$2.8 - 11.3$

a merger-rate of 8^{+47}_{-5} yr^{-1} which results in the same rate for *Swift*/BAT short GRBs from jets with an opening angle of $16°$ and the *Swift*/BAT field of view. The *Swift*/BAT field of view is ~ 1.4 sr, therefore the all-sky rate of short GRBs within the NS-NS detection volume is ~ 0.27 yr^{-1}; or by assuming that all *Swift*/BAT GRBs have the same redshift distribution, the rate becomes ~ 1.1 yr^{-1} as only $1/4$ of *Swift*/BAT short GRBs have a measured redshift. For each of our jet models we find the fraction that have peak afterglows brighter than $m_r \leq 21$, and of this fraction we find the percentage that are associated with GRBs. If the all-sky rate of short GRBs within the NS-NS LIGO detection volume is $0.27 \leq R_{SGRB} \leq 1.1$ yr^{-1} then the merger rate for each model is shown in Table 3.1.

If we consider the number of potential counterparts with $m_r \leq 21$ for each of these models with our parameters, we find that homogeneous jets will result in $\sim 2 - 8$ yr^{-1}, two-component jets will result in $\sim 3 - 12$ yr^{-1}, power-law jets $\sim 0.4 - 1.8$ yr^{-1}, and Gaussian jets $\sim 0.4 - 1.5$ yr^{-1}. Note, however that Bromberg et al. (2013) demonstrated that $\sim 60\%$ of *Swift* short GRBs are non-collapsar in origin, which would reduce the estimated merger rates presented here by this factor.

Here we have considered NS-NS mergers, if short GRBs are from BH-NS mergers only, then the rate will be a factor ~ 10 larger, given that the maximum GW detection

distance is approximately twice that for NS-NS mergers. As the merger ejecta from a BH-NS is not isotropically distributed, a larger fraction of the ejecta is on the rotational plane, and the jet may not propagate through the merger ejecta; no significant cocoon phase will result in a wider jet. Any jet structure will be the result of the acceleration/formation mechanism. The fraction of bright EM jet counterparts to wide homogeneous jets from BH-NS mergers will be higher than those indicated here for NS-NS mergers; a homogeneous jet with $\theta_j \sim 25°$ will produce GRBs in $\sim 27\%$ of GW detected mergers, whilst orphan and GRB afterglows with peak flux $m_r \leq 21$ will accompany $\lesssim 45\%$ of GW detected mergers within the BH-NS GW detection limit ~ 600 Mpc. If the population is all BH-NS mergers with a $25°$ homogeneous jet, the merger rate will be $10 \leq R_{BH-NS} \leq 40$ yr^{-1}, and the number of bright GW-EM counterparts is $4.5 - 18$ yr^{-1}. GW-EM counterparts from the jet will be detectable for a significant fraction of BH/NS-NS GW detected mergers; bright counterparts will typically peak $\lesssim 100$ days after the merger.

Electromagnetic follow-up of a GW trigger requires broadband monitoring of the GW localization region; a bright optical transient from the jet afterglow, with these models, is expected within ~ 14 days. Optical telescopes with a limiting magnitude of ~ 21 (e.g. ZTF, Black GEM, GOTO) in joint observations with X-ray and γ-ray telescopes (e.g. *Swift*, *Fermi*, MAXI, Chandra) should perform intensive searches/monitoring within the first few weeks. At later times, any search or monitoring should be conducted by mid- to large-sized telescopes with higher sensitivity (e.g. Subaru HSC, LSST, LT) and radio/infrared observatories (e.g. VLA, ALMA), although high-energy monitoring could also reveal a late transient from an off-axis afterglow. For GW detected mergers that are significantly closer than 200 Mpc, the search timescales should be extended as any transients from structured or off-axis orphan afterglows will be brighter than the limiting detection thresholds for longer.

Given one well sampled GW-EM counterpart, the presence of extended jet structure could be revealed if the system is favourably inclined. An 'on-axis', within the jet core angle, afterglow would not reveal any signature of jet structure. However, afterglows at higher inclinations, or orphan afterglows, could reveal the presence of jet structure; an achromatic re-brightening would indicate a two-component, or a power-law structured jet. A shallow decline or slowly brightening afterglow with a soft peak would indicate a Gaussian type jet structure observed at relatively high inclination (within the jet opening angle). For an off-axis orphan afterglow, either a sharp peak followed by a weak decay until a break or a shallow rise to a late peak can be used to indicate the existence of extended jet structure. Where the prompt emission has been fully suppressed, with no X-ray flash or low-luminosity γ-ray burst, differentiating between an afterglow from within the jet opening angle and a genuine off-axis orphan in the cases of extended jet structure may not be possible.

4.   GRB 170817A as a jet counterpart to gravitational wave trigger GW 170817

This Chapter has been published as Lamb & Kobayashi (2017b).

4.1   Introduction

Short γ-ray bursts (GRBs) are thought to be due to internal energy dissipation (e.g. Meszaros & Rees, 1993; Kobayashi et al., 1997; Daigne & Mochkovitch, 1998; Zhang & Yan, 2011) in an ultra-relativistic jet launched when rapid accretion of material by a compact merger object occurs following a binary neutron star (NS-NS) or neutron star black hole (NS-BH) merger (e.g. Eichler et al., 1989; Paczynski, 1990; Kluźniak & Lee, 1998). The NS-NS/BH merger is due to the loss of orbital energy and angular momentum via gravitational radiation (e.g. Phinney, 1991). This makes such systems a candidate for gravitational wave (GW) detection by advanced LIGO/*Virgo* (Abbott et al., 2016a). The detection of a GRB in association with a GW signal is key to confirming the neutron star binary merger scenario as the progenitor for short GRBs.

GRB 170817A, with an isotropic equivalent γ-ray energy $E_\gamma = (4.0 \pm 0.98) \times 10^{46}$

erg at ~ 40 Mpc, a duration for 90% of the γ-ray energy $T_{90} \sim 2 \pm 0.5$ s, and a νF_ν spectral peak energy $E_p = 185 \pm 62$ keV (Connaughton et al., 2017; Goldstein et al., 2017a,b; Savchenko et al., 2017a,b) was detected by *Fermi*/GBM and INTEGRAL as a potential electromagnetic (EM) counterpart to the binary NS merger GW 170817 (Abbott et al., 2017c,f) with a delay of ~ 2 s from the GW detection to the GRB. From the GW signal, the system is inclined with an angle $0 \leq i \leq 36°$ from the line-of-sight (Abbott et al., 2017d), where the inclination i gives the angle between the rotational axis and the observer. Using known constraints on H_0 the inclination is $3 \leq i \leq 23°$ with the Planck $H_0 = 67.74 \pm 0.46$ km s^{-1} Mpc^{-1} (Planck Collaboration et al., 2016), and $14 \leq i \leq 32°$ using the Type Ia supernova distance scales from SHoES $H_0 = 73.24 \pm 1.74$ km s^{-1} Mpc^{-1} (Riess et al., 2016); more recently, an inclination of $i = 18 \pm 8°$ using H_0 from the Dark Energy Survey was found by Mandel (2018).

The Swope Supernova Survey detected an optical counterpart (SSS17a) in association with the galaxy NGC4993, 10.9 hours post-merger (Coulter et al., 2017). The counterpart was consistent with a blue kilo/macro-nova from the dynamical merger ejecta (e.g. Tanaka et al., 2014; Metzger et al., 2015; Tanaka, 2016; Barnes et al., 2016; Wollaeger et al., 2017). See also (Arcavi et al., 2017; Covino et al., 2017; Cowperthwaite et al., 2017; Drout et al., 2017; Evans et al., 2017a; Gall et al., 2017; Kilpatrick et al., 2017; Nicholl et al., 2017; Pian et al., 2017; Smartt et al., 2017; Tanaka et al., 2017; Tanvir et al., 2017; Valenti et al., 2017, etc). If GRB 170817A was from internal dissipation within a compact merger jet then the GRB would be accompanied by an afterglow. In this chapter we calculate the expected flux at various frequencies from a forward and reverse shock. We model the afterglow from a low-luminosity GRB jet, a low Lorentz factor (Γ) jet, structured jets with either a two-component, power-law, or Gaussian structure, and a GRB seen off-axis from a homogeneous jet with typical

parameters.

In §4.2 the jet models and parameters used to predict the afterglows are described. In §4.3 we discuss the results and their implications for GRB 170817A, and in §4.4 we give final comments. The work and discussion of this chapter focuses on the days immediately after the GW and GRB detection in August 2017 and therefore assumes no knowledge of the subsequent afterglow evolution. An update that includes radio, optical and X-ray afterglow from $\sim 10 - 110$ days has been added at the very end of §4.4.

4.2 Afterglow Prediction

Energy dissipation within an ultra-relativistic jet that results in a GRB will be followed by a broadband afterglow as the jet decelerates in the ambient medium; depending on the jet parameters, the peak magnitude and timescale at various frequencies can vary significantly. By assuming that GRB 170817A was from a compact-merger jet viewed either within or outside the jet opening angle we can make reasonable predictions for the expected afterglow. A forward shock afterglow is expected to accompany all on-axis GRBs, although a reverse shock may also be present at early times and typically at low frequencies.

In the following section we calculate the afterglow from forward and reverse shocks for a high Lorentz factor, low kinetic energy GRB jet (e.g. Sari et al., 1998, 1999; Kobayashi & Sari, 2000), and for low Lorentz factor, low and high kinetic energy jets (e.g. Lamb & Kobayashi, 2016). We also calculate a forward shock afterglow for various jet structure models viewed off the central axis, and a homogeneous jet viewed outside the jet half-opening angle (e.g. Lamb & Kobayashi, 2017a).

4.2.1 High Γ, Low Kinetic Energy Jet

Using the isotropic γ-ray energy reported by *Fermi* for GRB 170817A, $E_\gamma = (4.0 \pm 0.98) \times 10^{46}$ erg, and making reasonable assumptions for the afterglow parameters, a prediction can be made for the expected flux from the afterglow at various frequencies. The typical parameters for a sample of short GRBs are given by Fong et al. (2015) who find that the ambient density is $n \sim (3 - 15) \times 10^{-3}$ cm^{-3}, and the γ-ray efficiency[1] is $0.4 \lesssim \eta \lesssim 0.7$. As the γ-ray luminosity of GRB 170817A is well below the typical values for a short GRB, we extend the efficiency range to a lower limit of 0.1; for a jet with an efficiency lower than 0.1, see the discussion at the end of §4.2.2. From the efficiency and γ-ray energy the jet kinetic energy can be determined, $E_k = E_\gamma(1/\eta - 1)$; the jet kinetic energy drives the afterglow. The accelerated particle distribution index for short GRBs is $p = 2.43^{+0.36}_{-0.28}$ (Fong et al., 2015), we use $p = 2.5$ as our fiducial value. Other assumed jet parameters are the jet bulk Lorentz factor, $\Gamma = 80$, and the microphysical parameters, $\varepsilon_B = 0.01$, and $\varepsilon_e = 0.1$. Note that these parameters are assumed throughout unless otherwise stated.

The duration of the GRB can be used to indicate the width of the relativistic shell, $\Delta_0 \sim cT_{90}$ (Kobayashi et al., 1997), where we assume that the GRB is from internal dissipation processes and c is the speed of light. If the bulk Lorentz factor is below a critical value $\Gamma_c = (3E_k/32\pi n m_p c^2 \Delta_0^3)^{1/8}$, then the reverse shock cannot effectively decelerate the shell; here m_p is the mass of a proton. For short GRBs the reverse shock is typically described by the thin shell case. The shell crossing time for such

---

[1] The efficiency of the prompt-emission from an internal shock origin is usually given by $\eta \sim f_{\rm dis}\varepsilon_e f_{\rm rad}$ where the fraction of energy dissipated is $f_{\rm dis} \lesssim 0.5$, and the fraction of energy radiated is $f_{\rm rad} \sim 1$. Using $\varepsilon_e = 0.1$, the value of the efficiency should be $\eta \lesssim 0.05$. However, the value estimated from an internal shock efficiency can be much higher if we consider the collision of multiple shells with a broad range of Lorentz factors (Kobayashi & Sari, 2001). The resultant light curve would appear smoother and broader for a large number of shells. We base our estimates first on the central observed values of η found for short GRBs by Fong et al. (2015) where the range of observed efficiencies is $10^{-3} \lesssim \eta \lesssim 0.98$.
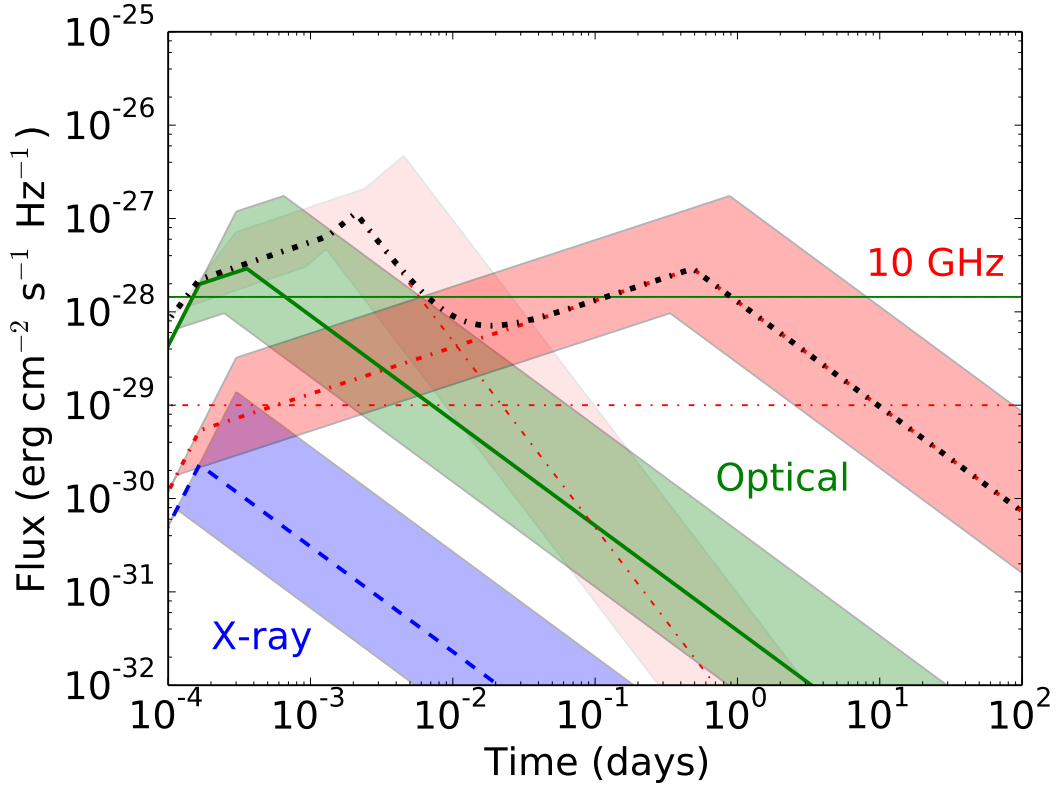
Figure 4.1: Afterglow light curves for a jet with an isotropic γ-ray energy of 4.0×10^{46} erg, a γ-ray efficiency of $\eta = 0.4$, a jet bulk Lorentz factor $\Gamma = 80$, in an ambient medium of $n = 0.009$ cm^{-3} with microphysical parameters $\varepsilon_B = 0.01$ and $\varepsilon_e = 0.1$, and a luminosity distance of 40 Mpc. The blue dashed line shows the X-ray afterglow, the green solid line shows the optical afterglow, and the red dash-dotted line shows the 10 GHz radio afterglow. The shaded regions indicate the light curve for an efficiency $0.1 \le \eta \le 0.7$. The reverse shock is important at radio frequencies, the 10 GHz reverse shock is shown as a thin dash-dotted red line and faint shaded region for the range of jet energies considered; the forward and reverse shock light curve at 10 GHz is shown as a thick black dash-dotted line. The red dashed horizontal line indicates the 1μJy limit, the green horizontal solid line indicates $m_{AB} \sim 21$ magnitude, and lower-limit of the y-axis is the X-ray sensitivity $\sim 0.4 \ \mu$Crab at 4 keV
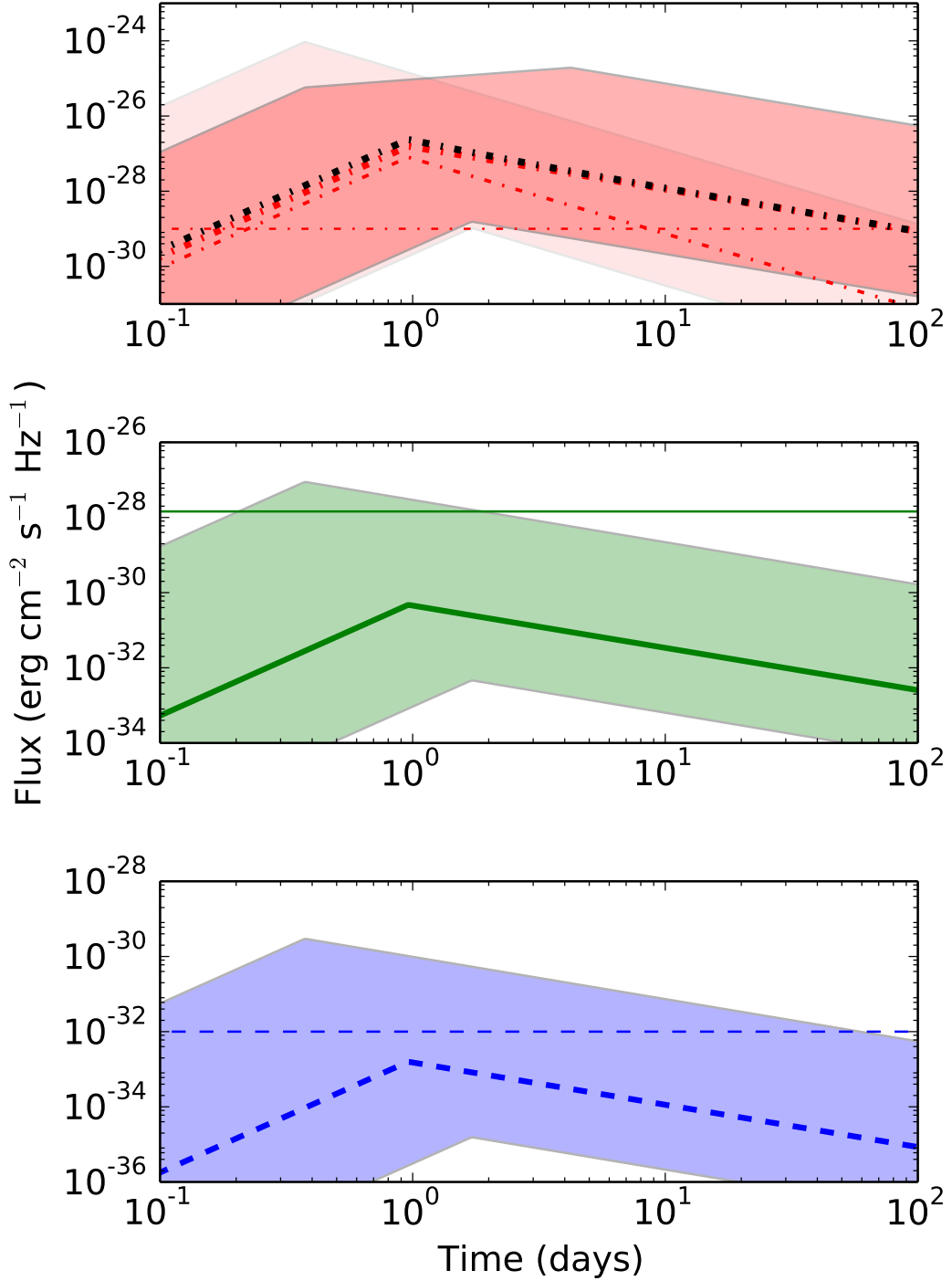
Figure 4.2: Afterglow from a low-Γ jet with an isotropic γ-ray energy of 4.0×10^{46} erg, a γ-ray efficiency of $0.001 \leq \eta \leq 0.7$ and a luminosity distance 40 Mpc. The jet bulk Lorentz factor is estimated from the delay time as $2.2 \lesssim \Gamma \lesssim 10.0$, all other parameters are as Figure 4.1. The lines show the afterglow for a jet with $\Gamma \sim 3.9$, the shaded regions indicate the uncertainty in the kinetic energy and the Lorentz factor. Colours are as for figure 4.1. **Top** panel: 10 GHz emission where the thin dash-dotted line and faint shaded region indicate the reverse shock; the thick dash-dotted line and shaded region indicate the forward shock; the sum of reverse and forward shock light-curves is shown as a black dash-dotted line. The red horizontal dashed line indicates the 1 μJy limit. **Middle** panel: optical afterglow. The green solid line shows the optical magnitude 21. **Bottom** panel: X-ray afterglow. The blue horizontal dashed line is ~ 0.4 μCrab at ~ 4 keV

a reverse shock is $\sim (\Gamma/\Gamma_c)^{-8/3}T_{90}$ and the characteristic frequency for the reverse shock is $\nu_{m,RS} \sim \nu_{m,FS}/\Gamma^2$ (Kobayashi, 2000), where subscripts RS and FS indicate reverse and forward shocks respectively and $\nu_{m,FS}$ is the forward shock characteristic frequency. The spectral peak flux at the characteristic frequency is proportional to the number of electrons, the magnetic field, and the bulk Lorentz factor. The mass in the shell is a factor Γ larger than the heated and swept up ambient density of the forward shock region. The spectral peak flux for the reverse shock is then $F_{\nu,\mathrm{max},RS} \sim \Gamma F_{\nu,\mathrm{max},FS}$. The forward and reverse shock regions can have a different pre-shock magnetization parameter ε_B, for simplicity we assume that they are the same.

At low frequencies synchrotron self-absorption becomes important; for the reverse shock, synchrotron self-absorption will limit the flux more efficiently than for the forward shock because the effective temperature of the electrons in the reverse shock region is lower by a factor $\sim \Gamma$. The limiting flux, at a given frequency ν and observer time t, for the reverse shock is (e.g. Kobayashi & Sari, 2000)

$$F_{\nu,\mathrm{BB}} \sim 2\pi m_p \Gamma^3 \left(\frac{\nu c t}{D}\right)^2 \varepsilon_e \left(\frac{p-2}{p-1}\right) \left(\frac{e}{\rho}\right) \max\left[\left(\frac{\nu}{\nu_m}\right)^{1/2}, 1\right], \qquad (4.1)$$

where e is internal energy density and ρ is the mass energy density in the reverse shock region. At the shock crossing time $(e/\rho) \sim 1$, and $(e/\rho) \propto t^{-2/7}$ after the shock crossing. For the forward shock, the limiting flux is a factor Γ larger at the shock crossing time.

If the ejecta from the central engine is magnetized, ε_B in the reverse shock region would be higher than that in the forward shock region. The higher ε_B will make the reverse shock peak slightly later and brighter. At early times and low frequencies, synchrotron self-absorption limits the reverse shock emission. As the reverse shock region expands, the emitting surface becomes larger, and the flux limit grows as
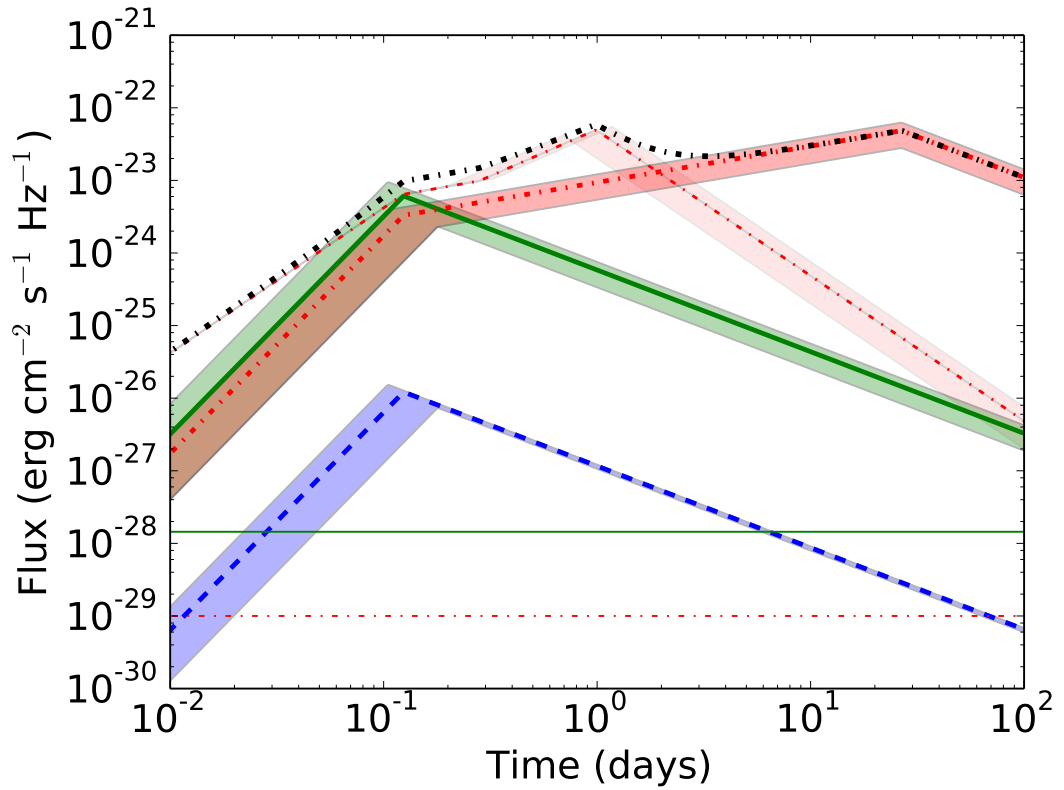
Figure 4.3: Afterglow from a low Γ jet with a jet kinetic energy of 10^{52} erg, and a luminosity distance 40 Mpc. The jet bulk Lorentz factor is estimated from the delay time as $\Gamma \sim 30$. Shaded regions represent the range of ambient densities $(3 \lesssim n \lesssim 15) \times 10^{-3}$ cm^{-3}, all other parameters are as Figure 4.1. The reverse shock at 10 GHz is shown as a thin dash-dotted red line and faint shaded region. Colours are as for Figure 4.1. The green horizontal solid line is optical $m_{\mathrm{AB}} = 21$, and the red horizontal dash-dotted line indicates the 1 μJy limit

$F_{\nu,\mathrm{BB}} \propto t^{1/2}$ (see Kobayashi & Sari, 2000; Kopač et al., 2015, for the black body approximation) where $\nu < \nu_{m,RS}$. When this limit becomes higher than the synchrotron flux $F_\nu \propto \varepsilon_B^{1/3} t^{-1/2}$ (Kobayashi, 2000), the reverse shock component peaks. Note that the self-absorption limit does not depend on ε_B, but the synchrotron flux does. By equalizing the two flux estimates, we find that the peak time and peak flux of the reverse shock emission are scaled as $\varepsilon_B^{1/3}$ and $\varepsilon_B^{1/6}$ respectively. If $\nu > \nu_{m,RS}$, these scalings are $F_{\nu,\mathrm{BB}} \propto t^{9/7}$, and $F_\nu \propto \varepsilon^{(p+1)/4} t^{-2}$. We find the peak time and flux are scaled as $\varepsilon_B^{(p+1)/4}$ and $\varepsilon_B^{(p+1)/10}$ respectively. For low Γ outflows, synchrotron self absorption is less important and the reverse shock will peak at the time when the shock crosses the shell. If $\nu_{m,RS} < \nu$ at peak time, then the peak time and flux are proportional to $\varepsilon_B^{(p-1)/4}$ and $\varepsilon_B^{3(p-1)/4}$, (e.g. Zhang & Kobayashi, 2005; Kobayashi et al., 2007). The forward shock light curve will evolve as $t^{-3(p-1)/4}$ after the peak.

A jet viewed on-axis will exhibit a light curve break when $\Gamma^{-1} < \theta_j$ (Sari et al., 1999), where θ_j is the jet half-opening angle. As $\Gamma \propto E^{1/8} n^{-1/8} t^{-3/8}$, the break time should occur at

$$t_j \sim 10 \, E_{\mathrm{k},50}^{1/3} n_{-2}^{-1/3} (\theta_j/0.31)^{8/3} \text{ days}, \tag{4.2}$$

where subscripts follow the convention $N_x = N/10^x$, θ_j is in radians and we normalise to a jet with $\theta_j = 0.31$ rad, or $\sim 18°$. Note that for GRB 170817A to be on-axis i.e. within the jet opening angle, the value of θ_j should be larger than the system inclination. For jets where the kinetic energy is $\lesssim 10^{48}$ erg, or the half-opening angle is $\lesssim 6°$, then the jet will break at ~ 1 day. Where the energy is low and the jet is narrow, then the break will occur at ~ 0.1 days. The jet half-opening angle is unknown, however as the inclination is $\sim 18°$ (Mandel, 2018) this can be used to indicate a wide jet if the GRB is observed on-axis. The jet-break is not included in the analysis.

The afterglow light curve for a jet viewed on-axis is shown in Figure 4.1; the ambient density is set as the mean of the Fong et al. (2015) sample, $n = 0.009$ cm^{-3}.

Before the deceleration time, when Γ is constant, the forward shock flux and characteristic frequency depend on the ambient density as $[F_{\nu,\mathrm{max}}, \nu_m] \propto n^{1/2}$. The deceleration time depends on the number density as $t_{dec} \propto n^{-1/3}$. After the deceleration time, $\nu_m \propto t^{-3/2}$ and the dependence on the ambient density vanishes. Where $\nu < \nu_m$ at the deceleration time, the light curve will continue to increase as $F_\nu = F_{\nu,\mathrm{max}}(\nu/\nu_m)^{1/3}$ until $\nu = \nu_m$, the peak here is therefore $F_\nu \propto n^{1/2}$ as ν_m no-longer depends on n.

Afterglow light curves are shown for 10 GHz, optical, and X-ray frequencies. The shaded regions represent the uncertainty in the γ-ray efficiency $0.1 \leq \eta \leq 0.7$. The bold afterglow lines show the light curve for a γ-ray efficiency $\eta = 0.4$, where the dash-dotted red line is 10 GHz, the solid green line is optical (5×10^{14} Hz), and the dashed blue line is X-ray (10^{18} Hz). The reverse shock emission is shown as a thin dash-dotted red line with a faint shaded region; and the reverse and forward shock afterglow at 10 GHz assuming the mean efficiency is shown as a thick black dash-dotted line. The forward shock dominates emission for optical and X-ray frequencies. As a reference, the horizontal dash-dotted line shows $1~\mu$Jy, horizontal solid line shows $m_{\mathrm{AB}} = 21$, and the approximate *Swift*/XRT (X-Ray Telescope) limit is given by the lower-limit of the y-axis at 10^{-32} erg cm^{-2} s^{-1} Hz^{-1}.

4.2.2 Low Γ Jets

The minimum radius at which the prompt γ-ray photons can be emitted is the photospheric radius, where the outflow becomes optically thin. The photospheric radius is given by

$$R_p = \left[\frac{\sigma_T E_{\mathrm{k}}}{4\pi m_p c^2 \Gamma} \right]^{1/2} \sim 1.9 \times 10^{13} E_{\mathrm{k},50}^{1/2} \Gamma_1^{-1/2} \text{ cm}, \qquad (4.3)$$

where σ_T is the Thomson cross-section.

Considering the relatively high E_p despite the low L_γ we assume that the prompt

γ-ray photons are emitted near the photosphere. The observed delay time between the GW signal and the GRB is equivalent to the travel time for a constant Lorentz factor flow to a radial distance equivalent to the photospheric radius, $\Delta t \sim R_p/2\Gamma^2 c$. The bulk Lorentz factor is then

$$\Gamma = \left[\frac{(\sigma_T E_{\mathrm{k}})^{1/2}}{4\Delta t c^2 (\pi m_p)^{1/2}} \right]^{2/5} \sim 12 \, E_{\mathrm{k},50}^{1/5} \left(\frac{\Delta t}{2 \, \mathrm{s}} \right)^{-2/5}, \qquad (4.4)$$

where Δt is the measured delay time.

The prompt γ-ray emission is predicted to be suppressed for a jet with a low Lorentz factor, the higher energy emission will be suppressed due to pair production and the total energy in the photons reduced due to adiabatic cooling before decoupling from the expanding plasma at the photosphere,[2] (e.g. Hascoët et al., 2014; Lamb & Kobayashi, 2016). GRB 170817A had a thermal component (Goldstein et al., 2017b) that would be expected from photospheric emission (e.g. Pe'er et al., 2006a). To reflect the possible prompt suppression we extend the lower limit of the γ-ray efficiency range[3]. The Lorentz factor for a jet with $0.001 \leq \eta \leq 0.7$, and the observed E_γ, from equation 4.4, is $10.0 \gtrsim \Gamma \gtrsim 2.2$. The afterglow light curves from low Γ jets are shown in Figure 4.2; we use an efficiency of $\eta = 0.1$ for the light curve. The shaded region indicates the afterglow for the limits of the efficiency.

The low-Γ value for the outflow gives a relatively long deceleration time (t_{dec}) for the jet, where $t_{\mathrm{dec}} \propto \Gamma^{-8/3}$. The reverse shock will cross the shell at $\sim 0.4 - 1.7$ days for $10 \gtrsim \Gamma \gtrsim 2.2$ respectively. At radio frequencies the reverse shock emission will dominate over the forward shock light curve at t_{dec} for $\Gamma \gtrsim 5$. This will result

---

[2] This suppression results in the fraction of energy radiated being $f_{\mathrm{rad}} < 1$ while the assumed value for ε_e remains unchanged.

[3] Where the efficiency is high, the jet kinetic energy will be low and suppression of dissipated energy within a low Γ outflow reduced (see Lamb & Kobayashi, 2016). Such low-energy, low-luminosity, and low Γ jets may form a distinct population (e.g. Siellez et al., 2016)

in a brightening of the light curve before the forward shock peak due to the reverse shock. The reverse shock is only important at early times and for the upper limits of the parameter space; the reverse shock is shown for the 10 GHz light curves in Figure 4.2.

The level of suppression of the prompt emission is unknown; if all jets from binary neutron star mergers produce jets with a similar kinetic energy (e.g. Shapiro, 2017), then the afterglow would appear brighter than a low-luminosity jet afterglow with a typical η value. Using a jet kinetic energy of $E_k = 10^{52}$ erg, the bulk Lorentz factor from equation 4.4, would be $\Gamma \sim 30$ and the prompt emission significantly suppressed (e.g. Lamb & Kobayashi, 2016). The prompt efficiency for such a jet would be very low, $\eta \sim 10^{-6}$, where the observed GRB had energy equivalent to GRB 170817A. The afterglow for such a jet is shown in Figure 4.3; as the jet kinetic energy is fixed, here the limits of the shaded regions represent the uncertainty on the ambient medium number density, $n \sim (3 - 15) \times 10^{-3}$ cm^{-3}. A reverse shock is apparent at 10 GHz, peaking at ~ 2 days with a flux ~ 10 Jy; the reverse shock is shown in the figure as a thin red dash-dotted line with the associated uncertainty in the ambient number density. A black dash-dotted line indicates the sum of the 10 GHz light curve from the forward and reverse shocks.

4.2.3 Structured Jet

GRBs are usually assumed to have a homogeneous, or 'top-hat', structure i.e. the energy and Lorentz factor are uniform in a jet cross-section and the jet has a sharp edge defined by the jet half-opening angle. However, jets may have some intrinsic structure either due to the formation and acceleration processes or as a result of jet breakout from merger ejecta. Here we use the structured jet models from Lamb & Kobayashi (2017a); see also Xiao et al. (2017) for a similar analysis or Jin et al. (2017) and Kathirgamaraju
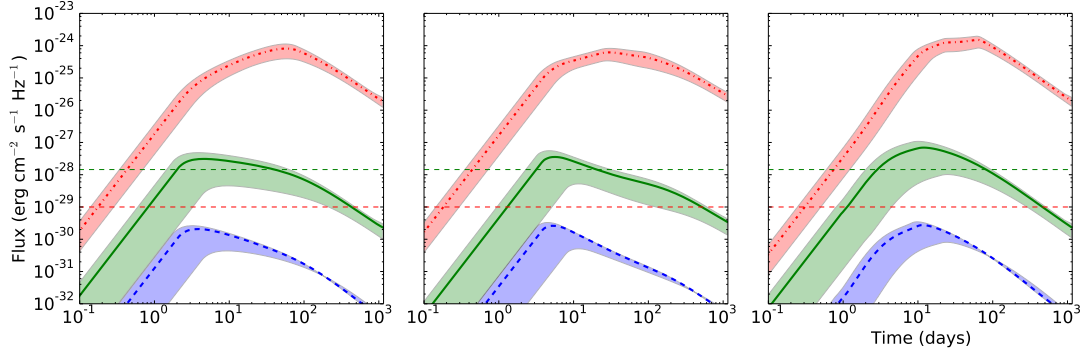
Figure 4.4: Afterglows from jets with structure; jet core parameters are $E_{\mathrm{iso}} = 10^{52}$ erg, $\eta = 0.4$, $\Gamma = 80$, and $\theta_c = 6°$, all other parameters are as previously used. The jet structure extends to $25°$ in each case. **Left**: Gaussian structure, a Gaussian function on E and Γ with angle from the centre. Jet inclined to the observer at $18.5°$. **Middle**: Power-law structure with a decay index outside of the core of $k = -2$. Jet inclined to the observer at $25.5°$. **Right**: Two-component structure, where the second component has 5% of the core parameters. Jet inclined to the observer at $11°$.

et al. (2018) for discussion of the prompt emission from a structured jet. For each of the three models used the total isotropic equivalent jet core energy is fixed at 10^{52} erg, and the core extends to an angle of $6°$ from the central axis. The jet parameters, E and Γ, vary according to the model: for a two-component jet, E and Γ are at 5% of the core values between $(6-25)°$; for a power-law jet, E and Γ vary with angle outside the core following a power-law index -2; and for a Gaussian structured jet the parameters E and Γ depend on angle following a Gaussian function from $(0-25)°$. The detected prompt emission in a 50-300 keV band is determined for each jet model at observation angles from $(0-25)°$ and a distance 40 Mpc. The observation angle values are selected for each jet structure where the detected prompt photon flux is comparable to the observed *Fermi*/GBM and INTEGRAL. The afterglow from each model for the determined inclination is then generated following the method in Lamb & Kobayashi (2017a).

The Gaussian jet model, shown in Figure 4.4 left panel, has an inclination of $18.5°$. For the power-law jet model, shown in Figure 4.4 central panel, the inclination angle is

$25.5°$. For the two-component model, shown in Figure 4.4 right panel, the inclination angle is $11°$; note that for the two-component model the γ-ray emission is that seen off-axis from the core jet region, the wider sheath component has a low-Γ value such that the prompt emission is fully suppressed. In the figure the afterglow at 10 GHz is shown in red with a dash-dotted line, optical is shown in green with a solid line, and X-ray is shown in blue and with a dashed line. The shaded region represents the uncertainty in the ambient medium number density, with the line indicating the afterglow for the mean $n = 0.009\ \mathrm{cm}^{-3}$.

For each model the first break in the light curve is due to the deceleration time for the jet component inclined towards the observer, i.e. the jet-component at the inclination angle. At radio frequencies, the light curve will peak when the characteristic frequency crosses the observation band, $\nu_m = \nu$. At optical and X-ray frequencies, and at radio frequencies for the two-component jet, a late-time excess or a shallow decay is due to the off-axis emission from the bright core of the jet. Any late-time break in the light curve is due to the edge of the jet becoming visible i.e. the jet-break, equation 4.2.

For the structured jet models the photon flux at the detector from the prompt emission approximates, without fine-tuning, the observed parameters: for the Gaussian jet the prompt fluence is $\sim 3.8 \times 10^{-7}\ \mathrm{erg\ cm}^{-2}$; for the power-law jet the prompt fluence is $\sim 7 \times 10^{-7}\ \mathrm{erg\ cm}^{-2}$; and for the two-component jet the prompt fluence is $\sim 2.1 \times 10^{-7}\ \mathrm{erg\ cm}^{-2}$. The *Fermi*/GBM measured fluence is $(2.8 \pm 0.2) \times 10^{-7}\ \mathrm{erg\ cm}^{-2}$ (Goldstein et al., 2017b; Abbott et al., 2017f). The difference in fluence between the jet models and the observed value is due to the choice of numerical resolution. The fluence for each jet model was calculated in $0.5°$ steps from $0 - 28°$ and the inclination for the jet determined by the angle for which the fluence was closest to the observed value.
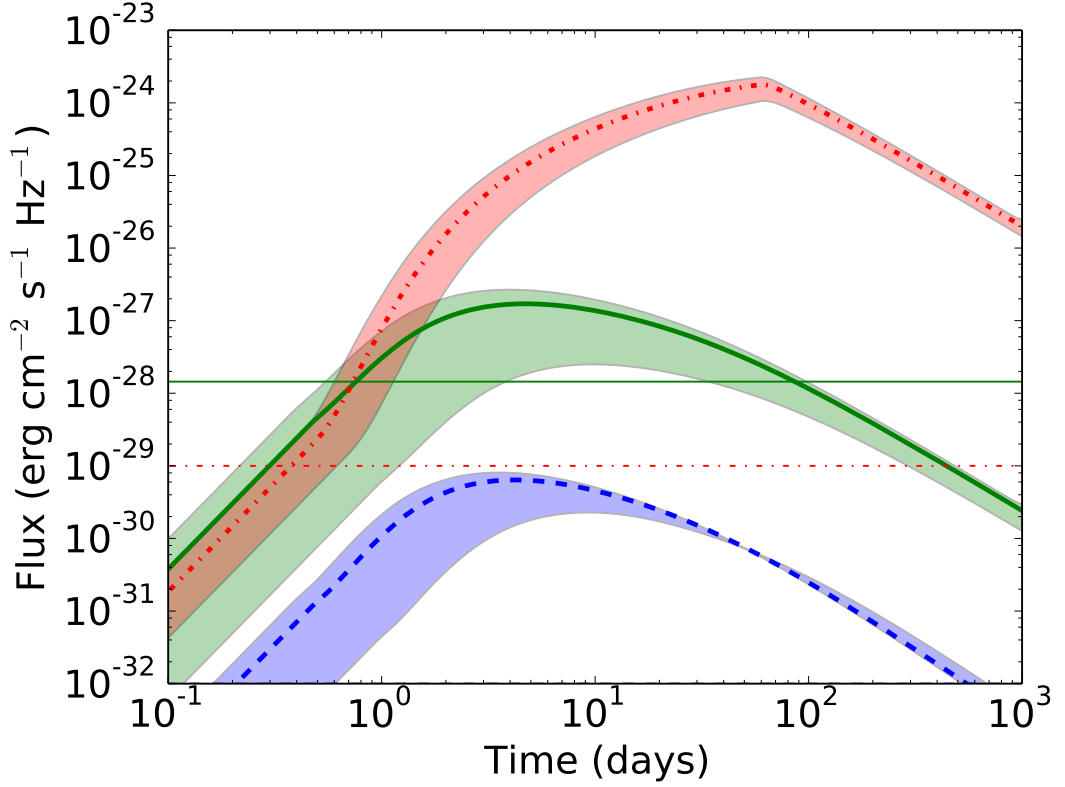
Figure 4.5: Off-axis afterglow from a homogeneous jet with $E_{\mathrm{iso}} = 10^{52}$ erg, $\eta = 0.4$, $\Gamma = 80$, and a half-opening angle $\theta_j = 6°$. The observed γ-ray fluence in the 50-300 keV band is 2.1×10^{-7} erg cm^{-2}; the inclination from the jet central axis is $11°$ and the ambient density is in the range $0.003 \leq n \leq 0.015$ cm^{-3}.

4.2.4 Off-Axis Afterglow

The T_{90} duration of GRB 170817A is longer than the typical value of ~ 0.6 s (Zhang et al., 2012), although still within the usual period for short GRB classification $\lesssim 2$ s. The delay time between the GW signal and the detected prompt emission, and the duration and low-luminosity of the γ-rays could be due to the jet inclination to the line-of-sight; where for an off-axis observer the time until emission and the duration are lengthened from that for an on-axis observer by the relativistic Doppler factor, $t \propto \delta^{-1}$ where t is the observed time, $\delta = [\Gamma(1 - \beta \cos\theta_{\mathrm{obs}})]^{-1}$ is the Doppler factor and β the velocity as a fraction of c, and the observed fluence is $\propto \delta^3$ (e.g. Ioka & Nakamura, 2001). The

off-axis prompt emission will also appear to be brighter in X-rays (e.g. Yamazaki et al., 2002).

If the jet is inclined in such a way that the observer's line-of-sight is outside of the jet edge i.e. $\theta_{\mathrm{obs}} > \theta_j$, then the prompt and afterglow emission will be delayed and suppressed when compared to that seen by an on-axis observer i.e. $\theta_{\mathrm{obs}} \to 0$. In considering an observer at various angles from the jet central axis, we use the method in Lamb & Kobayashi (2017a) which includes the jet geometry and emission surface to determine the inclination at which the prompt γ-ray photons have a similar fluence[4]. At an inclination of $11°$ for a jet with $\theta_j = 6°$, $E_{\mathrm{iso}} = 10^{52}$ erg, an efficiency $\eta = 0.4$, and a $\Gamma = 80$, the simplest estimate of the fluence in a T_{90} period from our model is 2.1×10^{-7} erg cm^{-2}. The corresponding afterglow in an ambient medium $0.003 \leq n \leq 0.015$ cm^{-3} is shown in Figure 4.5 where the colours are as previous figures. Note that as $\nu_a < \nu < \nu_m$ at the deceleration time for the 10 GHz light curve, then the synchrotron self-absorption frequency $0.25 \lesssim \nu_a \lesssim 0.75$ GHz at this time will not affect the light curve (Sari et al., 1999).

Given an observed $E_p \sim 185$ keV, and the inclination, jet half-opening angle and Γ used, the 'on-axis' spectral peak energy would be a few MeV. Short GRBs with a spectral peak of a few MeV include GRB 061006, 070714, and 090510; where the $E_p = [955 \pm 267, \ 2150 \pm 1113, \ \mathrm{and} \ 8370 \pm 760]$ keV respectively (e.g. Zhang et al., 2012; Piron, 2016). All of these GRBs have high luminosities for short GRBs, where $L_\gamma > 10^{52}$ erg s^{-1}. The high on-axis E_p value applies to the two-component jet discussed in §4.2.3, where the wider sheath component has no detectable γ-ray emission and only contributes to the afterglow light curve.

---

[4] We do not change any of the prompt energy parameters from the model in Lamb & Kobayashi (2017a) except the total isotropic energy, efficiency, and bulk-Lorentz factor, where we use $E = 10^{52}$ erg, $\eta = 0.4$ and $\Gamma = 80$ instead of $E = 2 \times 10^{52}$ erg, $\eta = 0.1$ and $\Gamma = 100$. This maintains consistency with earlier scenarios and avoids fine-tuning.

4.3 Discussion

By assuming that the observed GRB is from a compact merger jet we have shown the expected afterglow light curves for various jet models. If GRB 170817A was a low-luminosity GRB viewed on-axis, the afterglow in X-ray and optical would peak within seconds of the GRB. A reverse shock in the radio, typically fainter than $\lesssim 1$ mJy at 10 GHz, may be visible peaking on a timescale of minutes; this will be followed by the radio forward shock afterglow peak with flux $\lesssim 0.1$ mJy at ~ 1 day i.e. Figure 4.1. The predicted optical afterglow is fainter than $m_{\mathrm{AB}} \lesssim 19$, and the X-ray afterglow is detectable by *Swift*/XRT but will fade rapidly. The X-ray afterglow will peak within seconds and typically last ~ 15 minutes before becoming too faint for *Swift*/XRT, where we assume an X-ray limit of $> 10^{-32}$ erg cm^{-2} s^{-1} Hz^{-1}. Such a fast and faint transient would be challenging to detect.

By considering the delay time from GW signal to GRB, constraints can be put on the jet bulk Lorentz factor, if the jet is inclined within the half-opening angle i.e. on-axis. The energy dissipated will decouple from the jet when the optical depth becomes unity, at the photospheric radius. By using an assumed γ-ray efficiency, the jet kinetic energy can be estimated and from this and the delay time a value for Γ found. The bulk Lorentz factor found using an efficiency $0.001 \leq \eta \leq 0.7$ is $10.0 \geq \Gamma \geq 2.2$ respectively. This is consistent with the low-Γ jet model of Lamb & Kobayashi (2016) where the prompt emission is expected to be significantly suppressed. The forward shock afterglow from such a jet is shown in Figure 4.2; the afterglow peak in all bands is $\lesssim 1$ day and optical and X-ray are faint. Radio emission at 10 GHz is typically $\lesssim 1$ mJy, and would be detectable for $\gtrsim 1 - 100$ days.

If the γ-ray efficiency is very low i.e. the jet kinetic energy is $E_{\mathrm{k}} >> E_{\gamma}$ then the derived bulk Lorentz factor, using $E_{\mathrm{k}} = 10^{52}$ erg, is $\Gamma \sim 30$. This value is consistent with the low-Γ jet model, predicting suppression of the prompt emission resulting in

a low-luminosity GRB. The afterglow for such a jet is shown in Figure 4.3; the peak afterglow is typically a few hours after the GRB at optical and X-ray frequencies. Radio, optical, and X-ray emissions are bright in all cases. The 10 GHz afterglow remains at the ~ 1 Jy level for $\sim 10 - 1000$ days, while optical and X-ray fade rapidly.

A jet with extended structure may naturally produce low-luminosity GRBs at wider angles where the jet energetics are lower. By following the structured jet models of Lamb & Kobayashi (2017a), we show the expected afterglow from a jet with these models where the observed γ-ray flux is equivalent to the detected *Fermi* value. The afterglows from a Gaussian jet viewed at $i = 18.5°$, a power-law jet viewed at $i = 25.5°$, and a two-component jet viewed at an inclination $i = 11°$ are shown in Figure 4.4. Radio, optical and X-ray emissions are bright in all cases with optical and X-ray light curves peaking $\sim 3 - 100$ days, and 10 GHz at $\sim 20 - 100$ days at the 0.1-1 Jy level. Various features are distinct for each jet model: the Gaussian jet has an early peak with a shallow rise or decline in optical and X-ray emission for ~ 100 days before breaking to a more rapid decline. In addition the radio typically peaks at the break. For an observer at a wider inclination, the afterglow light curve will show a slow rise from a few days to a peak at $\gtrsim 100$ days at all frequencies (e.g. Lamb & Kobayashi, 2017a). The power-law jet has a sharp early peak at optical and X-ray frequencies whilst the 10 GHz afterglow has a later peak with a slower increase in flux after the deceleration time. Finally the two-component jet has a softer peak and shows a slight rebrightening at late times, especially at radio frequencies, before a rapid decline.

An observer at an inclination just higher than the jet's half-opening angle will see the relativistically beamed prompt and afterglow emission at a later time and at a lower frequency and intensity. The observed delay in the prompt emission, and the low-luminosity can be explained by the jet inclination; the afterglow in such a case would be similarly delayed and fainter. We show the afterglow for an observer at $11°$

from the jet central axis, where the jet has a half-opening angle $\theta_j = 6°$, an isotropic equivalent blast energy 10^{52} erg, a γ-ray efficiency of $\eta = 0.4$, and $\Gamma = 80$. The X-ray afterglow, at ~ 4 keV, rises slowly to a peak flux $\lesssim 10^{-30}$ erg cm^{-2} s^{-1} Hz^{-1} at ~ 30 days; optical afterglow has a similar rise index and peak time with a $m_{\mathrm{AB}} \lesssim 16$; while the 10 GHz afterglow has a steeper rise rate, breaking to a soft peak from 70 days, the 10 GHz afterglow is brighter than 1 μJy from $\gtrsim 1 - 2$ days and peaks at ~ 1 Jy.

A neutron star binary merger is expected to produce a kilo/macro-nova that will peak with a thermal spectrum at optical to near-infrared frequencies during the first 10 days (e.g. Tanaka et al., 2014; Metzger et al., 2015; Tanaka, 2016; Barnes et al., 2016; Wollaeger et al., 2017). For the structured or off-axis jet afterglows, the optical emission may peak on a similar timescale to the expected kilo/macro-nova. However X-ray and radio emission will reveal the afterglow in such a case. Non-detections by X-ray and/or radio searches for an afterglow from GRB 170817A at early, < 10 days, times can be used to rule out the various structured, and high kinetic energy with low-Γ jet scenarios presented here.

The prompt emission for GRB 170817A was fit by an exponential cut-off power-law, the Comptonization spectrum model (e.g. Yu et al., 2016), with a νF_ν spectral peak energy at $E_p \sim 185 \pm 62$ keV and an index $\alpha \sim -0.62 \pm 0.40$ (Abbott et al., 2017f; Connaughton et al., 2017; Goldstein et al., 2017a,b; Savchenko et al., 2017b). Due to the sparsity of high-energy photons, the requirement for an ultra-relativistic bulk Lorentz factor is relaxed. Additionally, with this E_p and low luminosity, the GRB does not fit on the $E_p - L_\gamma$ correlation for all GRBs (e.g. Yonetoku et al., 2010; Zhang et al., 2012). A structured jet where the photospheric emission is treated more precisely could explain the GRB (Meng et al., 2018), or the γ-rays could be due to inefficient particle acceleration, wider angle Comptonized emission, or scattered jet internal prompt emission (Kisaka et al., 2015b, 2017). Alternatively the detected γ-

ray flux may not have been from a jet but a more isotropic outflow (e.g. Salafia et al., 2018); a cocoon or shock-breakout (Pe'er et al., 2006b; Nakar & Piran, 2017; Lazzati et al., 2017a; Gottlieb et al., 2018), or a flare due to fragmentation of a viscous disc (Perna et al., 2006).

4.4 Conclusions

We have modelled the afterglow from various jet dynamical scenarios given the observed γ-ray flux detected by *Fermi* and INTEGRAL for GRB 170817A in association with the GW signal GW 170817. Four scenarios were considered: (i) an on-axis low-luminosity GRB with typical high Lorentz factor; (ii) low-Γ jets viewed on-axis; (iii) jets with extended structure where the prompt emission would have an energy similar to that observed; (iv) and an off-axis jet where the prompt emission is geometrically corrected to give the observed γ-ray fluence. In all cases an afterglow is expected on various timescales and with a range of peak fluxes. Where the kinetic energy is typical for a GRB jet, the afterglow for either a low-Γ jet or from a structured jet where the prompt γ-ray emission is suppressed or low, will result in a bright afterglow, easily detectable at all frequencies. If GRB 170817A is from within a relativistic jet then the jet must be either:

- A low energy jet with either a low- or high- Γ, and a high γ-ray efficiency $\eta \gtrsim 0.4$

- A GRB jet viewed off-axis

If the jet is the first of these, then a large population of low-luminosity, low-energy jets from neutron star mergers could exist resulting in a high GW detection rate for neutron star mergers.
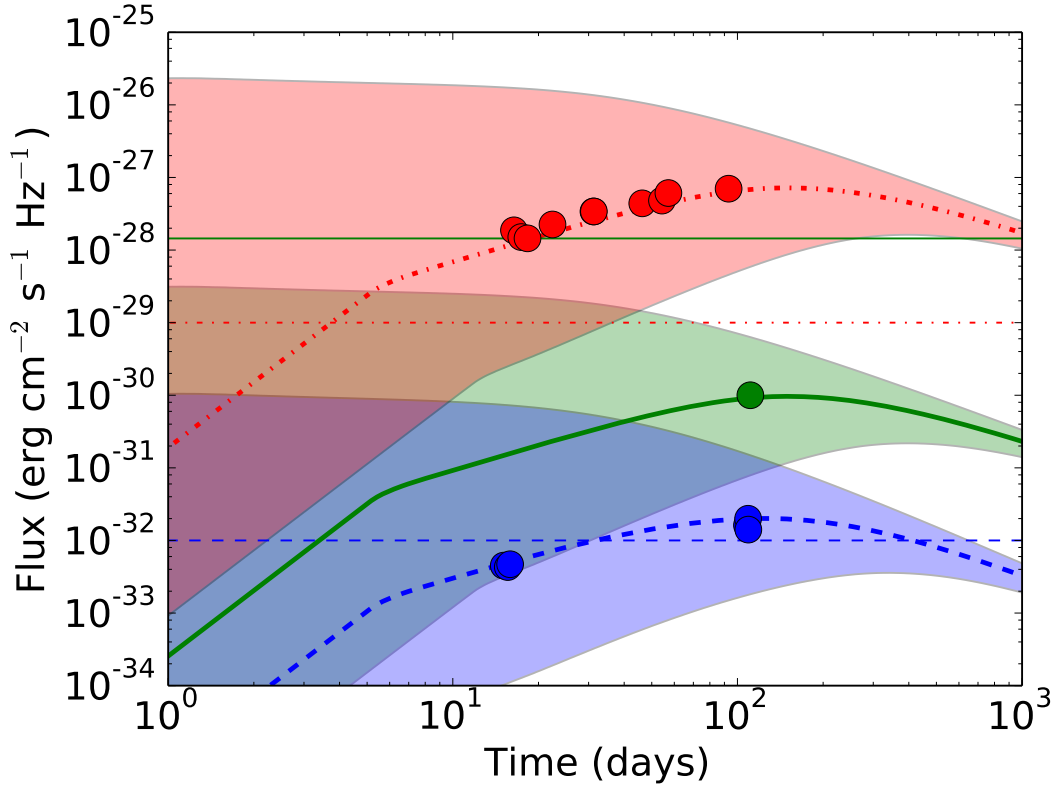
Figure 4.6: Afterglow from a Gaussian structured jet with parameters tuned to recreate the observed radio, optical and X-ray observations if viewed at $20°$. The afterglow range indicates the light curve for an inclination $10 \leq i \leq 26°$. X-ray at 1 keV is shown in blue, optical with green, and 3 GHz in red. Markers indicate observations from Hallinan et al. (2017), Haggard et al. (2017), Lyman et al. (2018), Margutti et al. (2017), Mooley et al. (2017), Ruan et al. (2017), and Troja et al. 2017; errorbars are typically smaller than the markers and not included.

4.4.1 An Evolving Counterpart

X-ray and radio counterparts were initially reported from $\sim 9 - 18$ days post-merger (Corsi et al., 2017; Hallinan et al., 2017; Margutti et al., 2017a; Mooley, Hallinan & Corsi, 2017; Troja et al., 2017). Electromagnetic observations continue to follow the evolution of the afterglow to GW170817-GRB 170817A.

Radio counterparts are expected from the merger ejecta at late times (e.g. Hotokezaka et al., 2016), however, the X-ray and radio observations from $\sim 10 - 100$ days (Haggard et al., 2017; Hallinan et al., 2017; Margutti et al., 2017a; Mooley et al.,

2018; Ruan et al., 2018) and recent optical data (Lyman et al., 2018) are consistent with a Gaussian structured jet. One phenomenological fit is for an observer at $\sim 20°$, and with the parameters used in §4.2.3 tuned (e.g. Lyman et al., 2018; Margutti et al., 2018) ; where energy follows an angular distribution $\propto e^{-\theta^2/\theta_c^2}$ and the bulk Lorentz factor $\propto e^{-\theta^2/2\theta_c^2}$. The parameters for the afterglow shown in Figure 4.6 are $E_k = 10^{52}$ erg, $\Gamma = 80$ for the jet core with an angle $\theta_c = 4.5°$, microphysical parameters $\varepsilon_e = 0.01$ and $\varepsilon_B = 0.01$, $p = 2.1$, and ambient number density $n = 1.3 \times 10^{-3}$ cm^{-3}; where the range indicates an observer between $10 \leq i \leq 26°$ (Mandel, 2018) and the thick lines indicate $20°$. The GRB emission is not directly reproduced by this model, however the contribution from scattered prompt emission of the jet core (Kisaka et al., 2017) or other higher latitude effects have not been considered. Alternatively a jet-cocoon structure can explain the observed afterglow (Lazzati et al., 2017c), or a choked-jet cocoon (Mooley et al., 2018).

The afterglow models presented here can be used with future EM jet-counterparts to GW detected NS mergers. For a Gaussian structured jet, the rising broadband emission of the afterglow from ~ 10 days depends on the inclination and the jet parameters, whereas for a cocoon model it should be fairly consistent for a wide range of observation angles. Failed GRB afterglows, or other jet structures could be revealed by further GW-EM detections.

5. Transient Survey Rates for Orphan Afterglows from Compact Merger Jets

This Chapter has been submitted to MNRAS as Lamb et al. (2018).

5.1 Introduction

The most promising candidate for the progenitor of short γ-ray bursts (GRBs) is the merger of a binary neutron star (NS) system or a NS black hole (BH) system (e.g. Eichler et al., 1989; Narayan et al., 1992; Mochkovitch et al., 1993; Bogomazov et al., 2007; Nakar, 2007; Berger, 2014). Such systems are candidate targets for gravitational wave detectors, and as such there has been a focus on potential electromagnetic (EM) counterparts to such mergers (Nissanke et al., 2013). Amongst the counterparts are the isotropic macro/kilo-nova (e.g. Li & Paczyński, 1998; Barnes & Kasen, 2013; Tanaka & Hotokezaka, 2013; Piran et al., 2013; Metzger & Fernández, 2014; Tanaka et al., 2014, 2018; Barnes et al., 2016; Tanaka, 2016; Metzger, 2017a), radio counterparts (e.g. Nakar & Piran, 2011; Kyutoku et al., 2014; Margalit & Piran, 2015; Hotokezaka & Piran, 2015; Hotokezaka et al., 2016), wide angle coccoon emission (Lazzati et

al., 2017a; Nakar & Piran, 2017; Gottlieb et al., 2018; Kisaka et al., 2017), resonant shattering, merger-shock or precursor flares (Tsang et al., 2012; Kyutoku et al., 2014; Metzger & Zivancev, 2016), GRBs (e.g. Coward et al., 2014; Ghirlanda et al., 2016; Kathirgamaraju et al., 2018; Jin et al., 2017), failed GRBs (fGRB) (Dermer et al., 2000; Huang et al., 2002; Nakar & Piran, 2003; Rhoads, 2003; Lamb & Kobayashi, 2016, 2017a), and off-axis orphan afterglows (e.g. Rossi et al., 2002; Granot et al., 2002; Zou et al., 2007; Zhang, 2013; Lazzati et al., 2017a; Sun et al., 2017). Some of these counterparts make promising potential transients for the next generation of optical survey telescopes e.g. Large Synoptic Survey Telescope (LSST) (LSST Science Collaboration et al., 2009), and Zwicky Transient Factory (ZTF) (e.g. Bellm, 2014; Bellm & Kulkarni, 2017).

Here we make predictions for transient rates in blind surveys (i.e. without a gravitational wave or γ-ray trigger), for orphan afterglows from short GRB jets and transients based on the expected excess as a result of low-Lorentz factor failed GRB jets (Lamb & Kobayashi, 2016) and/or jets with extended wide structure (e.g. Lamb & Kobayashi, 2017a; Kathirgamaraju et al., 2018; Jin et al., 2017; Xiao et al., 2017). Different jet structures predict different emission properties, especially for off-axis viewing angles. Therefore, the detection rate of orphan afterglows will give an important constraint on the structure and dynamics of the jets. We consider only the transients from the afterglow due to the jet-ISM interaction; such transients will be associated with all jetted short GRB progenitor models and the jet afterglow, orphan or otherwise, will have a non-thermal spectrum. Where short GRBs are exclusively due to NS/BH-NS mergers, then additional transients will be associated; most notably a macro/kilo-nova that will have a red/infra-red frequency peak brightness that depends on the viewing angle, and an earlier blue/ultra-violet peak that will be apparent depending on the system inclination. Macro/kilo-nova emission will have a thermal spectrum

and a very rapid decline after the peak.

In §5.2 we describe the merger jet parameters and models used and in §5.3 we describe the method for generating the cosmological population of merger jets. The results are described in §5.4, and discussed in §5.5. Concluding remarks are made in §5.6.

5.2 Merger Jet Models

We assume that the dominant progenitor for the short GRB population are relativistic jets from mergers (Levan et al., 2016). From the observed energetics of short GRBs a luminosity function can be determined (e.g. Wanderman & Piran, 2015; Sun et al., 2015; Ghirlanda et al., 2016; Zhang & Wang, 2018).

We generate seven populations of merger jets where we use a Wanderman & Piran (2015) redshift and luminosity function. Four have homogeneous jet structure models:

(i-iii) WP15$_{6/16/26}$: With a coasting phase bulk Lorentz factor $\Gamma = 100$ and a jet half-opening angle[1] of $\theta_j = 16 \pm 10°$ (Fong et al., 2015). For population (i) $\theta_j = 6°$, (ii) $\theta_j = 16°$, and (iii) $\theta_j = 26°$

(iv) LK16: With a bulk Lorentz factor distribution for the population defined as $N(\Gamma) \propto \Gamma^{-2}$ with a range $2 \leq \Gamma \leq 10^3$ (Lamb & Kobayashi, 2016). We assume each jet has a half-opening angle $\theta_j = 16°$

The final three jet populations use parameters that are described by the structured jet models in Lamb & Kobayashi (2017a). These jets have a core angle $\theta_c = 6°$ and a wider jet component to $\theta_j = 25°$ in each case. For the structured jets the luminosity function is used to determine the power within the jet core:

---

[1] Note that Ghirlanda et al. (2016) found this redshift distribution to indicate jet half-opening angles in the range $7° \leq \theta_j \leq 14°$, we use the wider angle and range to include the widest observations $\theta_j \gtrsim 25°$.

(v) LK17t, two-component jets where the wider component $\theta_c < \theta \leq \theta_j$ has energy and Lorentz factor at 5% the core value

(vi) LK17p, power-law jets where the energy and Lorentz factor between the core and jet edge scale with angle from the core using a negative index power-law, $\propto (\theta/\theta_c)^{-2}$

(vii) LK17g, Gaussian jets where the energy and Lorentz factor follow a Gaussian function with angle to the jet edge, $\propto e^{-\theta^2/2\theta_c^2}$

The existence of a jet edge for the structured jet models is motivated by relativistic magnetohydrodynamic simulations of neutron star mergers (e.g. Rezzolla et al., 2011; Dionysopoulou et al., 2015)

5.3 Method

We assume the short GRB rate[2] and luminosity function given in Wanderman & Piran (2015); note the event rate for this distribution varies with redshift, peaking at $z = 0.9$, and rapidly declines with increasing redshift ($R_{\mathrm{GRB}} = 45\ \mathrm{e}^{(z-0.9)/0.39}\ \mathrm{Gpc}^{-3}$ yr^{-1} where $z \leq 0.9$, and $R_{\mathrm{GRB}} = 45\ \mathrm{e}^{-(z-0.9)/0.26}$ for $z > 0.9$). At redshifts below the peak, the event rate is consistent with that found by D'Avanzo et al. (2014) and Sun et al. (2015). The luminosity function follows a broken power-law with the limits $5 \times 10^{49} \leq L_\gamma \leq 10^{53}$ erg s^{-1} and a brake at 2×10^{52} erg s^{-1}; at luminosities below the brake the power-law index is -1, and above the brake the index is -2. The luminosity function is defined with an interval $\mathrm{d}\log L_\gamma$. Note that we do not consider low-luminosity short GRBs, i.e. $L_\gamma < 5 \times 10^{49}$ erg s^{-1}. The origin of low-luminosity short GRBs is not known, the low-luminosity population could represent an extension

---

[2] Cosmological parameters $H_0 = 70$, $\Omega_M = 0.3$ and $\Omega_\Lambda = 0.7$ are used throughout

of the usual short GRB luminosity function to lower powers or a distinct population of low-luminosity short GRBs (e.g. Siellez et al., 2016). The afterglows from a population of low-luminosity GRBs would be intrinsically very faint and the redshift distribution of the observable sample limited to 'local' luminosity distances.

Using the short GRB rate (Gpc^{-3} yr^{-1}) and luminosity function, a correlation for isotropic equivalent energy and νF_ν spectral peak energy E_p in Tsutsui et al. (2013), and assuming a spectral index $\alpha = 0.5$ and $\beta = 2.25$ (Gruber et al., 2014) with a broken power-law, we find the minimum γ-ray luminosity for a detectable short GRB and the rate at a given redshift. We assume a detection if the number of photons in the energy band 15-150 keV is ≥ 0.3 ph cm^{-2} s^{-1} (Band, 2006). Using the minimum observable luminosity and the short GRB rate with redshift, the all-sky number of detectable short GRBs is ~ 71 yr^{-1}. *Swift*/BAT detects ~ 10 yr^{-1}, however as noted by Bromberg et al. (2013), the *Swift*/BAT short GRB sample is contaminated by non-merger (collapsar) short duration GRBs, the fraction of merger short GRBs is $\sim 60\%$. Using a detection rate of ~ 6 yr^{-1} the effective field-of-view for *Swift*/BAT is ~ 1.06 sr, this is less than the BAT partially coded field-of-view ~ 1.4 sr (Baumgartner et al., 2013). The *Swift*/BAT duty cycle, the sensitivity of the partially coded field-of-view, or the exact fraction of merger short GRBs may explain this discrepency. The all-sky rate for short GRBs is used to normalize the Monte Carlo merger jet samples.

For each model (i-vii), 10^5 merger-jets are generated. Each jet has a random isotropically distributed inclination i to the line-of-sight and a random redshift z using the short GRB redshift distribution. The jet energetics, and bulk Lorentz factor depend on the model parameters. The prompt emission is highly beamed and only detectable for typical cosmological distances and γ-ray energies from jets inclined within the jet half-opening angle. The γ-ray photon flux at the detector for a jet inclined within the half-opening angle is calculated considering the jet luminosity. A correlation between

the γ-ray luminosity and spectral peak energy for short GRBs is used to determine E_p (e.g. Yonetoku et al., 2004; Ghirlanda et al., 2009; Zhang et al., 2012; Tsutsui et al., 2013). We use the same GRB detection criteria as that used to estimate the all-sky *Swift*/BAT short GRB rate.

Using the fireball model (Piran, 1999) and an assumed γ-ray efficiency η for the prompt emission, the isotropic equivalent blast energy can be found from the γ-ray luminosity L_γ and timescale T_{90}. The jet kinetic energy $E_\mathrm{k} = L_\gamma T_{90}(1/\eta - 1)$ is dissipated in shocks that form as the jet decelerates in the ambient medium giving rise to an afterglow. The temporal evolution and peak afterglow flux of a GRB follows Sari et al. (1998, 1999), where the peak flux is $F_p \propto n^{1/2}\varepsilon_B^{1/2}E_\mathrm{k}D^{-2}$, here n is the ambient number density, ε_B is the microphysical magnetic parameter, and D is the luminosity distance.

For an off-axis observer, at an inclination greater than the jet half-opening angle θ_j, the observed flux is reduced by relativistic effects. The flux at a given observer frequency ν becomes $F_\nu(i,t) = a^3 F_{\nu/a}(0, at)$, where $a = \delta(i)/\delta(i=0)$ and $\delta = [\Gamma(1 - \beta\cos i)]^{-1}$ is the relativistic Doppler factor; Γ is the bulk Lorentz factor, and β is the jet velocity relative to the speed of light (Granot et al., 2002). Note that this relation is valid for a point source only and that for a jet with a defined opening angle the relativistic beaming factor for the flux is $\sim a^2$ for $i \lesssim 2\theta_j$, and the angle used to calculate the relativistic Doppler factor is $i - \theta_j$ where $i > \theta_j$ (Kumar & Panaitescu, 2000; Ioka & Nakamura, 2001). The off-axis jet model assumes multiple point sources that when summed over the extended jet opening angle account for the different analytical solution at $i \lesssim 2\theta_j$.

For all jets we use the method in Lamb & Kobayashi (2017a), with the relevant jet structure model to generate on/off-axis afterglows for the population of jets. The ambient density is assumed to be $n = 0.1$ cm^{-3}, microphysical parameter $\varepsilon_e = 0.1$,

Table 5.1: The number of afterglow transients from a given merger jet model that are brighter than a limiting r-band magnitude magnitude. All models use the redshift and luminosity function from Wanderman & Piran (2015). The GRB population in each sample is normalized to an all sky rate of *Swift*/BAT detectable short GRBs of ~ 71 yr^{-1}. The first value in each column is for orphan afterglows only, the values in square brackets are for GRB and orphan afterglows combined. The all-sky rates less than a given magnitude have an associated uncertainty of $\sim \pm 0.7$ deg^{-2} yr^{-1}. The LSST and ZTF detection rate is based on the mean timescale a transient is brighter than the telescope threshold

	Model	≤ 26 $\times 10^{-3}$ deg^{-2} yr^{-1}	≤ 24.5 $\times 10^{-3}$ deg^{-2} yr^{-1}	≤ 21 $\times 10^{-3}$ deg^{-2} yr^{-1}	≤ 20.4 $\times 10^{-3}$ deg^{-2} yr^{-1}	$\langle T_{\mathrm{LSST}} \rangle$ days	LSST yr^{-1}	$\langle T_{\mathrm{ZTF}} \rangle$ days	ZTF yr^{-1}
(i)	WP15$_6$	32.2 [33.6]	25.3 [26.7]	3.6 [5.0]	1.4 [2.8]	0.16 [0.20]	13.4 [17.6]	0.02 [0.03]	0.6 [1.9]
(ii)	WP15$_{16}$	20.2 [22.9]	18.5 [21.1]	2.3 [5.0]	0.8 [3.1]	0.12 [0.27]	7.3 [18.8]	0.03 [0.06]	0.5 [4.2]
(iii)	WP15$_{26}$	15.7 [17.5]	15.0 [16.7]	3.5 [5.2]	1.6 [3.3]	0.11 [0.34]	5.4 [18.7]	0.02 [0.07]	0.7 [5.2]
(iv)	LK16	60.0 [62.0]	39.2 [41.2]	3.7 [5.7]	1.8 [3.7]	0.54 [0.56]	70.0 [76.1]	0.09 [0.07]	3.6 [5.8]
(v)	LK17t	27.6 [29.3]	21.8 [23.5]	2.5 [4.2]	0.9 [2.5]	0.18 [0.30]	12.8 [23.2]	0.03 [0.11]	0.6 [6.2]
(vi)	LK17p	43.6 [45.4]	29.3 [31.1]	3.3 [5.0]	1.3 [2.9]	0.11 [0.25]	10.6 [25.7]	0.03 [0.12]	0.9 [7.8]
(vii)	LK17g	50.3 [51.5]	34.4 [35.5]	2.8 [4.0]	1.3 [2.5]	0.08 [0.14]	9.1 [16.4]	0.03 [0.07]	0.9 [3.9]

$\varepsilon_B = 0.01$, particle distribution index $p = 2.5$, and γ-ray radiation efficiency $\eta = 0.1$. For each population the normalized number of *Swift*/BAT GRBs and orphan afterglows are counted.

Using the distribution of peak afterglows from a given model, and a transient survey telescope's per night coverage, the number of transients with or without a GRB, that have an optical counterpart brighter than the survey's detection threshold can be found. For transients in our sample that are brighter than the LSST(ZTF) survey threshold, r-band magnitude $\sim 24.5(20.4)$, we determine the number that are brighter than this limit for $\geq 4(1)$ days. This ensures a minimum of two detections within the proposed cadence. For LSST we use a survey rate of ~ 3300 deg^2 night^{-1}, covering ~ 0.08 of the whole sky per night; for ZTF the survey rate is ~ 3760 deg^2 hour^{-1} where the average night is 8h 40m (Bellm, 2014). ZTF will cover ~ 0.09 of the whole sky per hour, and considering the observable fraction of the sky per night, will cover ~ 22500 deg^2 night^{-1} or ~ 0.55 of the whole sky per night with a 1 day cadence.
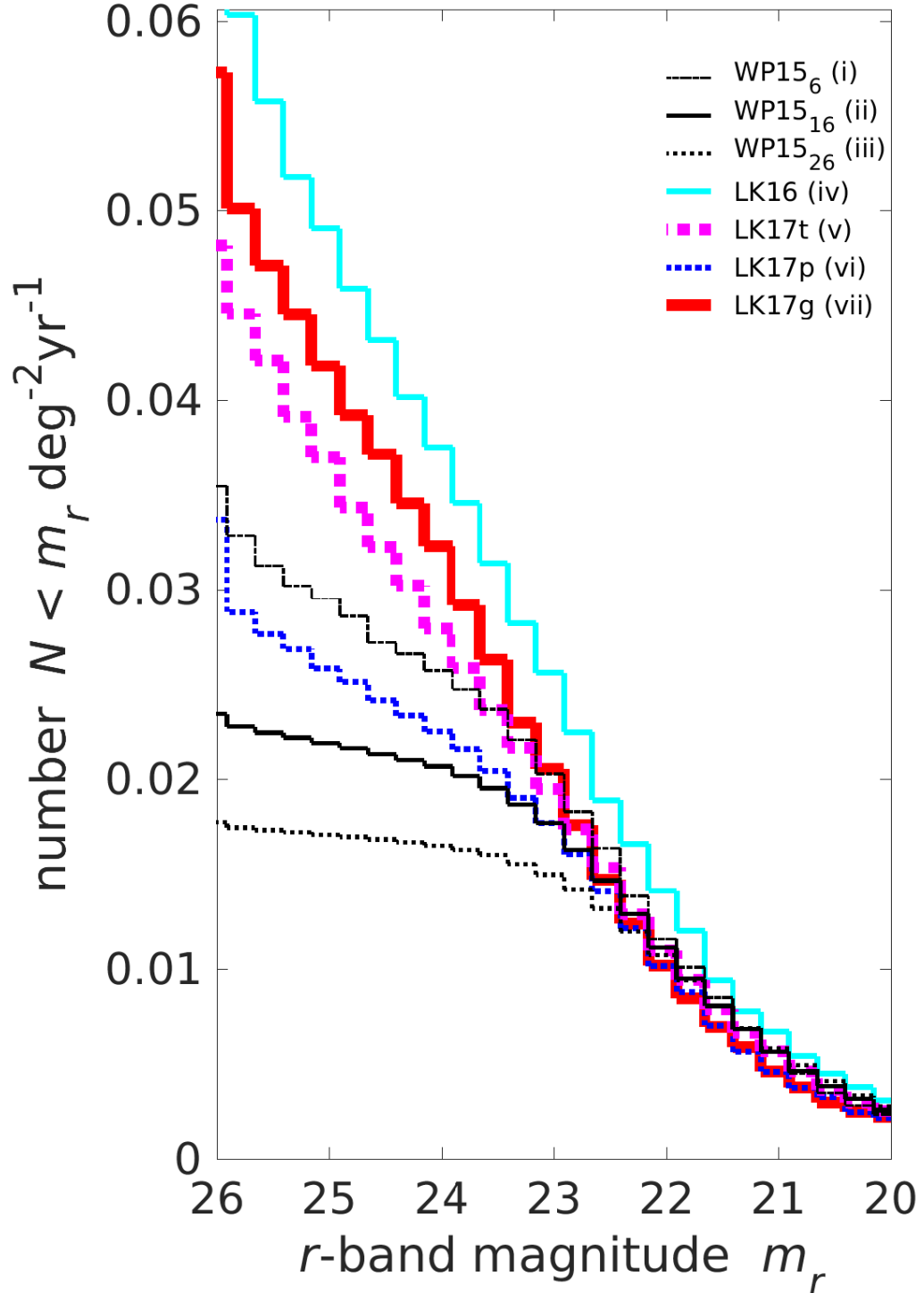
Figure 5.1: The number of afterglows (deg^{-2} yr^{-1}) brighter than a given magnitude for each jet model in $\Delta m_r = 0.25$ magnitude bins. The homogeneous jet models (i-iii) with a half-opening angle $\theta_j = 6°$ with a thin black dash-dotted line, $\theta_j = 16°$ are a black solid line, and $\theta_j = 26°$ with a thin black dotted line. The afterglows from the low Lorentz-factor jets model (iv) are shown with a medium thickness solid cyan line. The structured jet models (v-vii) are shown with a thin blue dotted line for the two-component model, a thick pink dotted line for the power-law structured jets, and a thick red solid line for the Gaussian structured jets.

5.4 Results

The rate of afterglow transients for each model is shown in Table 5.1. The various models are described in §5.2. For LK17t, LK17p and LK17g (v-vii), the opening angle at which a GRB is detectable depends on the distance, luminosity and inclination of the source. For the WP15 (i-iii) and LK16 (iv) models, a GRB is typically only detectable for inclinations that are less than the jet half-opening angle, $i \lesssim \theta_j$[3].

Figure 6.1 shows the number of afterglow transients per square degree per year brighter than a given r-band magnitude from merger jets. Each model is indicated by a different colour and line style as described in the figure caption. Each distribution is for both GRB and orphan afterglows (the value in square brackets in Table 5.1).

The homogeneous jet models with a fixed initial Lorentz factor WP15 (i,ii,iii) produce detectable GRBs, where the detector has our parameters and sensitivity, for $\sim 9 \pm 1\%$ of merger-jets that are inclined within the jet half opening angle. For homogeneous jets the typical inclination for on-axis, $i < \theta_j$, orphan afterglows and/or GRB detected systems is $\sim 2\theta_j/3$; for off-axis, $i > \theta_j$, the orphan afterglow is typically observed at an angular separation of $\sim \theta_j + 1.1°$, where the limiting magnitude is ≤ 26.

The typical redshift for a detected GRB with our detection criteria and parameters, for all of the jet models, is $\langle z \rangle = 0.5 \pm 0.07$. The uncertainty represents the different model mean values. The measured mean redshift value for the population of *Swift*/BAT short GRBs with redshift is $\langle z \rangle = 0.49$ (Berger, 2014). For the orphan afterglow populations the typical redshift is sensitive to the limiting magnitude. Where the afterglow peaks ≤ 26 and for the LSST sample where the peak ≤ 24.5 then $\langle z \rangle = 0.90 \pm 0.05$; for the limit of ≤ 21 and the ZTF sample with ≤ 20.4 then $\langle z \rangle = 0.80 \pm 0.05$. A signif-

---

[3] Merger jets at very low redshift or with very high energy may be detectable at γ-ray energies for inclinations just outside of the jet half-opening angle

icant fraction of all orphan afterglows in our sample are viewed on-axis, i.e. within the jet half opening angle. The prompt GRB can be undetected despite being favourably inclined due to the dynamics of the jet model, the detector sensitivity, γ-ray efficiency, and/or distance. The orphan afterglow in such a case will be phenomenolgically the same as a regular GRB afterglow (e.g. Cenko et al., 2013).

If detections are limited to two points brighter than the limiting magnitude in the given cadence of a survey telescope, then for LSST using a cadence of 4 days the number of transients brighter than magnitude 24.5 and the number for ZTF with a 1 day cadence but limiting magnitude of 20.4 is small in all cases. For the LSST sample, with or without a GRB, the fraction of transients brighter than the threshold for the 4 day cadence considered is $\sim 0.04 \pm 0.01$. For ZTF this fraction is $\lesssim 0.06$ for a one day cadence. These fractions are insensitive to the jet model.

5.5   Discussion

We have generated a Monte Carlo distribution of merger jets for each of the jet models considered: a population of homogeneous jets with a jet half-opening angle of $6°$, $16°$, or $26°$; a population of merger jets that have an independent Lorentz factor following a negative index power-law distribution; and three structured jet models, all with a core value of $6°$ and a jet edge at $25°$. The merger jets follow a Wanderman & Piran (2015) redshift distribution for merger (non-collapsar) short GRBs and have a random isotropic inclination. For each event the γ-ray photon flux at the detector in the energy band 15-150 keV is determined, if the flux is greater than the threshold value then a GRB is detectable. Each population of merger-jets is normalized by the all-sky rate of *Swift*/BAT detectable short GRBs.

The fraction of on-axis events $i < \theta_j$ will follow the probability distribution for

a randomly oriented bi-polar jet system with the jet half-opening angle θ_j, i.e. $1 - \cos\theta_j \sim \theta_j^2/2$. Not all on-axis events will produce a detectable GRB or afterglows above the detection threshold. For all models considered this is due to a combination of luminosity, distance to a merger, and spectral peak energy. For the LK16 and structured jet models, the failed GRB fraction is higher due to suppression of the prompt emission in the low-Γ/energy jet/components.

Forward shock afterglow transients from short GRBs, on-axis failed GRBs, and off-axis orphan afterglows are detectable by both the LSST and ZTF. The rate for both LSST and ZTF detectable transients depends on the nature of the jets in a population of mergers. Where the jet Lorentz factor varies from jet to jet, only a small fraction of the merger jets, when viewed on-axis, will produce a detectable GRB (e.g. Lamb & Kobayashi, 2016). Afterglows are typically fainter for a population of low Γ failed GRBs, this is due to the later deceleration time for the jet where $t_{\rm dec} \propto \Gamma^{-8/3}$, and the lower characteristic synchrotron frequency, $\nu_m \propto \Gamma^4$, meaning the optical peak flux is lower than the maximum synchrotron flux as $\nu_{\rm obs} > \nu_m$ at the peak time. This is reflected in the orphan afterglow rate being $\sim 2 - 3\times$ larger for LK16 model (iv) than for WP15$_{16}$ model (ii), where $\Gamma = 100$ for all events.

For jets with structure, the orphan afterglows are typically brighter than the orphan afterglows for a population of homogeneous jets (Lamb & Kobayashi, 2017a). Structured jets have higher latitude jet components with a low Γ that can suppress a GRB for an observer at these inclinations, thus structured jets can produce a larger fraction of orphan afterglows where the inclination is less than the jet half-opening angle. These orphans are typically brighter than a homogeneous jet described by the γ-ray bright region of a structured jet. However, for the two-component jet LK17t model (v) it is clear from Figure 6.1 that the rate of transients is $\sim 80\%$ that of the rate for a homogeneous jet population with $\theta_j = 6°$, WP15$_6$ model (iii). The two-component model

will typically have a γ-ray bright core, $\theta_c = 6°$, and an extended 'sheath' that generally fails to produce detectable GRBs. For model (iii), θ_j is equivalent to the core size in the two-component model. Due to the two-component models extended structure, GRBs are observable at $i > \theta_c$ in jets where the core luminosity is very high or the merger is nearby. Therefore the fraction of GRBs from this model is larger than that for the $6°$ homogeneous jet model and thus when the distributions are normalized the total number of mergers is smaller.

To consider the fraction of afterglows detected by blind sky surveys, the typical time period for which a transient is brighter than the limiting magnitude is determined. For the LSST(ZTF) limit of 24.5(20.4) the typical timescale is shown in Table 5.1. The product of the all-sky rate (deg^{-2} yr^{-1}), the per night survey field-of-view (deg^2 day^{-1}), and the typical timescale for a transient (day) gives the expected rate of detectable transients for a survey. For LSST the chance of detecting an orphan afterglow from a merger jet is reasonable, $5 \lesssim R_{\mathrm{OA}} \lesssim 70$ yr^{-1}, depending on the jet model. If we consider both orphan and GRB afterglows the rate increases, $16 \lesssim R_{\mathrm{AG}} \lesssim 76$ yr^{-1}. For ZTF the rate of detected orphan afterglows from merger jets is low, $0.5 \lesssim R_{\mathrm{OA}} \lesssim 3.6$ yr^{-1}. The combined orphan and GRB afterglow rate is more promising, $2 \lesssim R_{\mathrm{AG}} \lesssim 8$ yr^{-1}. However, in each case, the afterglow transients are rarely brighter than the detection threshold for longer than the cadence.

The differentiation between merger-jet origin orphan afterglows and collapsar or long GRB jet orphans will be difficult. Ghirlanda et al. (2015) predicts a rate of $R_{\mathrm{OA}} \sim 50$ yr^{-1} for the LSST from long-GRB jets. For faint transients, the peak flux may not be brighter than the host galaxy, magnitude $\sim 24 - 27$ (Berger, 2014). In such a case the transient will go undetected. However, short GRBs can be hostless or have typically large offsets from the bright core or star forming regions. Long GRBs are typically associated with star-forming galaxies and regions (e.g. Bloom et al., 1998; Djorgovski

et al., 1998; Fruchter et al., 2006), making faint orphan transients from long GRB jets more difficult to detect. Short GRB host galaxies systematically have an older stellar population, have a lower star-formation rate, and a higher metallicity than the host galaxies for long GRBs (Berger, 2014). Note however that short GRB host galaxies can be both early- and late- type galaxies. Additionally, simulations suggest that short GRB merger progenitor systems are over-produced by dwarf galaxies (O'Shaughnessy et al., 2017), these galaxies are typically faint with magnitude $-14 \lesssim M_{\rm B} \lesssim -10$ (Sabatini et al., 2003), approximately magnitude 28-32 at $z = 0.5$. The differences in the host galaxy and location within the host galaxy can be used to distinguish between the progenitor of GRB-less transients.

By considering the other associated transients i.e. resonant shattering flares or impact flares for NS mergers (Tsang et al., 2012; Kyutoku et al., 2014) or supernovae (SNe) for long GRBs, the origin of the orphan afterglow may be additionally constrained for nearby events. With the development of next generation gravitational wave detectors e.g. the Einstein Telescope (ET) (Punturo et al., 2010), the volume within which a NS/BH-NS merger can be detected increases. Coincident survey transients (e.g. Scolnic et al., 2018), within the ET detection horizon $z \sim 0.5$, and GW merger signals will be key to characterising the growing number of objects in the transient sky. The rate of transients at $z < 0.5$, with $m_r \leq 26$, for our models is $(0.2 \lesssim R_{z<0.5} \lesssim 6.8) \times 10^{-3}$ deg^{-2} yr^{-1}, and a mean rate $\langle R_{z<0.5} \rangle \sim 3.0 \times 10^{-3}$ deg^{-2} yr^{-1}. For each model the rate is: (i) 4.5, (ii) 0.6, (iii) 0.2, (iv) 6.8, (v) 4.0, (vi) 2.4, and (vii) 5.1 where the units are $\times 10^{-3}$ deg^{-2} yr^{-1}. These deep survey rates for a field-of-view 3300 deg^2 are: (i) 3.0(22.2), (ii) 0.5(20.4), (iii) 0.2(19.6), (iv) 12.6(114.6), (v) 3.3(24.2), (vi) 2.4(44.5), (vii) 2.4(23.7) yr^{-1} where the number in brackets is without the redshift condition.

The rate of orphan afterglows from long GRBs is higher than that for short GRBs

due to the difference in the occurence rate of either transient. Long GRBs typically have jet half-opening angles $\theta_j \sim 6°$ (Ghirlanda et al., 2015). The peak afterglow for a highly inclined system at $i > \theta_j$ decreases rapidly with increasing angle; for long GRB jets associated with SNe, the peak flux rapidly falls below the peak of the accompanying SN[4] where the absolute magnitude is typically $M \sim -19$. If the majority of long GRB jets are from core-collapse SNe then the orphan afterglow will be hidden by the SN for systems inclined at $i \gtrsim 20°$ away from the jet axis (Kathirgamaraju et al., 2016), this will reduce the number of detectable orphan afterglows from long GRBs, where it is assumed that all long GRBs have narrow homogeneous jets. Using the condition that an orphan afterglow from a long GRB must be inclined $i \leq 20°$, the fraction of the total population could be lower than the predicted 50 yr^{-1}.

Figure 6.2 shows how the absolute magnitude for an observer in the r-band changes with inclination for a homogeneous jet with $\theta_j = 16°$ and a range of isotropic equivalent energies $5 \times 10^{48} \leq E_{\text{iso}} \leq 10^{52}$ erg. The peak r-band macro/kilo-nova flux is shown as a red line, where the range is the observed diversity (Gompertz et al., 2017) which agrees with the predicted range for macro/kilo-nova peak magnitudes in Tanaka & Hotokezaka (2013) and Barnes & Kasen (2013). For jets from mergers, the associated macro/kilo-nova emission, although isotropic, is generally considered to be fainter for increasing observation angles (e.g. Tanaka et al., 2014; Tanaka, 2016; Metzger, 2017a; Wollaeger et al., 2017). The macro/kilo-nova decline with inclination shown in Figure 6.2 assumes a linear trend from an 'on-axis' view to an edge-view, where the change in magnitude is that from Wollaeger et al. (2017). The macro/kilo-nova associated with GW170817 is shown as a red triangle at an inclination of $28°$

---

[4] This depends on the K-corrected luminosity of the SN (Prentice et al., 2016). GRB afterglows are brighter over a broader spectrum than SNe due to the non-thermal nature of the emission, the off-axis GRB afterglow spectrum is increasingly shifted to lower frequencies as the observation angle increases, this effectively contributes to the reduction in the observed off-axis flux for an orphan afterglow at optical frequencies
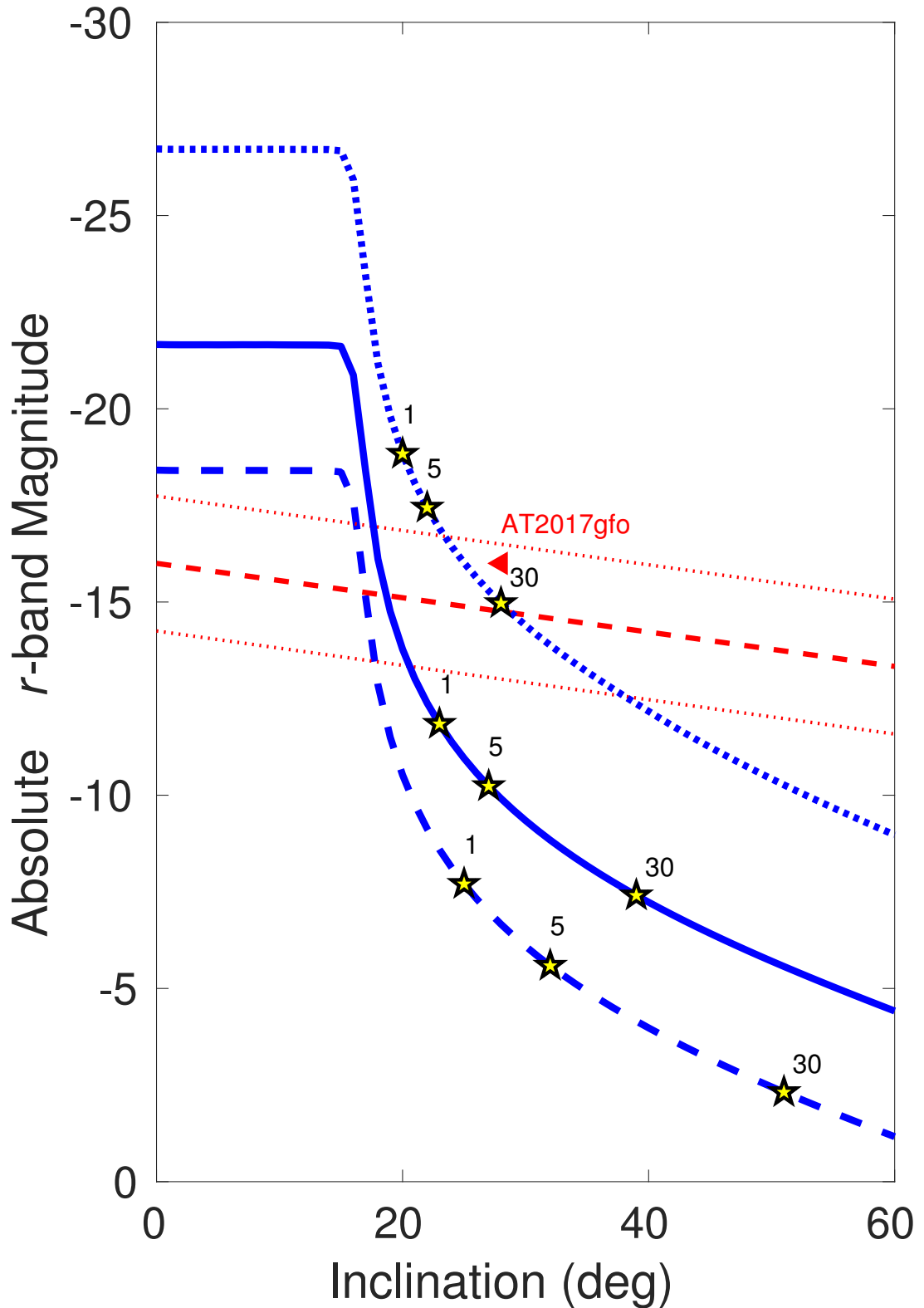
Figure 5.2: The peak afterglow in the r-band with the system inclination. The blue line indictaes the peak observed r-band absolute magnitude at a given system inclination. The jet is a homogeneous jet with a half-opening angle of $16°$ and an energy $E_{\mathrm{iso}} = 5 \times 10^{48}$ erg for the dashed blue line $E_{\mathrm{iso}} = 10^{50}$ erg for the solid blue line, and $E_{\mathrm{iso}} = 10^{52}$ erg for the dotted blue line. The yellow stars indicate the peak time after the merger in days at those points. The red lines indicate the expected peak macro/kilo-nova r-band magnitude with inclination. The dotted red lines indicate the observed diversity of macro/kilo-nova peak fluxes.

(see for example: Abbott et al., 2017e; Pian et al., 2017; Tanaka et al., 2017; Smartt et al., 2017; Tanvir et al., 2017; Evans et al., 2017b; Drout et al., 2017; Metzger, 2017b; Murguia-Berthier et al., 2017, etc.). Macro/kilo-nova will typically peak in the r-band $\lesssim 5$ days after the merger for an observer at any inclination. However, the jet afterglow peak flux time is much later for an off-axis observer (days to months) than for an on-axis observer (minutes to hours). Where an orphan afterglow peaks $\lesssim 1$ day or $\gtrsim 5$ days, a survey telescope may have two opportunities to observe the merger, one from the afterglow and a second from the macro/kilo-nova; the afterglow transient will typically fade much slower than that from a macro/kilo-nova and will have a non-thermal spectrum. Thus, even if the transients have coincident peaks, the afterglow will fade more slowly than the macro/kilo-nova. Additionally, due to the broadband nature of the afterglow a radio transient should accompany the optical, possibly peaking at a later time depending on the inclination of the system.

The orphan afterglow population may be dominated by low-luminosity GRBs. Such low-luminosity GRBs form a distinct population (Wanderman & Piran, 2010) where the rate is greater than that for long GRBs. The afterglow from low-luminosity GRBs is fainter than that for long GRBs (Barniol Duran et al., 2015), but the lower Lorentz factor of the ejecta means that any off-axis emission will have a reduced beaming effect. Where an orphan afterglow is brighter than the accompanying SNe, then low-luminosity GRB orphan afterglows may dominate the blind survey population.

The jets that produce long GRBs may exhibit the same structure or dynamical diversity as proposed for merger jets, the number of detectable orphan afterglows from long GRB or collapsar jets will be higher than that predicted by assuming homogeneous structured jets. The increased rate of orphan transients from either collapsar jets or merger jets would indicate the presence of intrinsic jet structure or a dominant population of low Γ jets. If long GRB jets follow the latter, i.e. a dominant low Γ pop-

ulation (Hascoët et al., 2014), the rate of orphan afterglows from collapsar jets would be higher by a similar fraction to that demonstrated here for merger jets with the LK16 model (iv). The light curve of an on-axis orphan afterglow will appear phenomenologically the same as a GRB afterglow, i.e. a power-law decay, $\propto t^{-1}$ with an observable break at late times. Whereas an off-axis orphan afterglow would decay with a steep, $\propto t^{<-2}$, decline with no jet-break.

We used a population of mergers that follow a lognormal time delay redshift distribution (Wanderman & Piran, 2015). If NS/BH-NS mergers follow a power-law time delay distribution that peaks $z \sim 1.5 - 2$, then a higher fraction of the short GRB population would go undetected due to the large luminosity distance. The observation of a host for short GRB 111117A at $z = 2.211$ could challenge the lognormal time delay model, although this redshift is still within the lognormal limits, the probability is ~ 2 orders of magnitude lower than for the peak at $z = 0.9$ (Selsing et al., 2017). Detectable orphan afterglows from a power-law time delay redshift distribution will follow the rates predicted here, although a significant excess would exist at very faint magnitudes, $m_r > 26 - 28$, where the population distribution peaks at a redshift $z \gtrsim 1.5$. For a discussion of a short GRB population with such a distribution see Sun et al. (2015) and Ghirlanda et al. (2016).

5.6 Conclusions

We have shown that the rate of orphan afterglows from merger (non-collapsar) short GRBs detectable by the LSST is $5 \lesssim R_{\mathrm{OA}} \lesssim 70 \ \mathrm{yr}^{-1}$, where the rate is $\sim 7.3 \ \mathrm{yr}^{-1}$ for a population of homogeneous jets with $\theta_j = 16°$. Where GRB afterglows are included, the rates become $16 \lesssim R_{\mathrm{AG}} \lesssim 76$ and $\sim 19 \ \mathrm{yr}^{-1}$ for homogeneous jets with $\theta_j = 16°$. The ZTF detection rate for orphan afterglows from short GRBs is low

$0.5 \lesssim R_{\mathrm{OA}} \lesssim 3.6$, the rate for afterglows with or without a *Swift*/BAT detectable GRB is $2 \lesssim R_{\mathrm{AG}} \lesssim 8$ yr^{-1}, and ~ 4.2 yr^{-1} for a population of homogeneous jets with $\theta_j = 16°$.

For populations of jets narrower than $\theta_j = 16°$, the rate of orphan afterglows increases. For LSST the orphan afterglow rate from a population of narrow short GRB jets is ~ 13.4 yr^{-1}. This increase is due to the increased rate in the parent merger population due to the normalization required to produce the detectable all-sky *Swift*/BAT non-collapsar GRB rate.

If the population of jets that produce short GRBs is dominated by jets with a low Γ, then the rate of orphan afterglows will increase significantly, ~ 70 yr^{-1} for LSST and ~ 3.6 yr^{-1} for ZTF. Where these jets result in failed-GRBs and are viewed within the jet half-opening angle, the light curve will appear phenomelogically the same as an on-axis GRB afterglow light curve.

If jets exhibit intrinsic structure, where the jet energetics extend beyond a homogeneous core to a defined edge, then the rate of orphan afterglows is greater than that for a homogeneous population; with the exception of the two-component jet structure when compared to the narrowest homogeneous jet population.

If LSST modifies the observation strategy from a fast survey to a deep-drilling field, then the obtainable sensitivity will increase. By focusing on a single field the potential to detect the same transient with multiple observations increases and with this the ability to identify orphan afterglows. As shown in Figure 6.1 and Table 5.1, the rate of detectable merger-jet transients increases significantly from a limiting magnitude of 24.5 to 26 for a population of narrow jets, a jet population dominated by low-Lorentz factors, or jets with intrinsic structure.

Orphan afterglows fade rapidly and will rarely be above the detection threshold > 1 day, single point candidate identification and fast targeted follow-up will be re-

quired. This presents a huge challenge for the identification of such transients by optical survey telescopes alone; however these challenges can be partially overcome by simultaneous broadband detections where unlike the majority of astrophysical transients the afterglows, both orphan and GRB, are expected to have both a radio and an X-ray counterpart. By searching for temporal and spatially coincident transients in radio and X-ray surveys (e.g. Square Kilometre Array (Dewdney et al., 2009), Einstein Probe (Yuan et al., 2015), SVOM (Cordier et al., 2018)) the correct identification of transients from GRB jets can be realised. The structured or dynamical models tested here could equally be applied to collapsar or long GRB jets. The observed rate of orphan afterglows from such jets would increase by a similar fraction for each case. Careful filtering of transients is required to successfully identify an orphan afterglow from either short or long GRB jets.

6.   Extending the "Energetic Scaling of Relativistic Jets From Black Hole Systems" to Include γ-ray-loud X-ray Binaries

This Chapter has been published as Lamb et al. (2017a).

6.1   Introduction

Astrophysical jets are observed on many different scales from proto-stars and X-ray binaries (XRBs) within our Galaxy, to radio-galaxies, blazars, and γ-ray bursts (GRBs) at cosmological distances. Relativistic jets from black hole (BH) systems have a broad range of luminosities and dynamics: XRBs with a BH component have bolometric luminosities that can reach $\sim 10^{39}$ erg s^{-1} (e.g. Mirabel & Rodríguez, 1999; Fender & Belloni, 2004), with Lorentz factors constrained by observations of the jet and counter-jet to a few $\Gamma \leq 5 - 10$; blazars, the on-axis analogue to the kilo-parsec jet structures of radio-galaxies (Urry & Padovani, 1995), have luminosities of $\sim 10^{48}$ erg s^{-1}, and Lorentz factors $\Gamma \leq 40 - 50$ (e.g. Marscher, 2006a; Lister et al., 2009; Jorstad et al.,

2013; Saikia et al., 2016); GRBs have isotropic equivalent energy outputs $\sim 10^{52}$ erg s^{-1}, where achromatic temporal breaks in the afterglow indicate a jet structure (e.g. Sari et al., 1999), and Lorentz factors $\gtrsim 100$ can be inferred from the highly variable non-thermal emission (e.g. Mészáros, 2002; Piran, 2004).

Several attempts have been made to unify the different scales of BH engines. The relativistic jets or ouflows from BH systems are thought to have a common mechanism. The appearance of superluminal features in a jet following a dip in X-ray emission has been observed for both XRBs and the radio-galaxy 3C120, where the X-ray dip is associated with accretion (Marscher et al., 2002). A fundamental plane connecting BH mass, radio, and X-ray luminosity was found for active galactic nuclei (AGN) and XRBs by Merloni et al. (2003). A scaling relation for the radio flux, from the core of AGN and XRBs, with BH mass M (or accretion rate), where most accretion scenarios produce the relation $F_\nu \propto M^{17/12-s/3}$ and s is the spectral index where $s = 0$ for flat spectrum sources and $s \sim 0.75$ for optically thin emission, demonstrates that the radio-loudness of jets scales with BH mass, where the mass can range over nine orders of magnitude (Heinz & Sunyaev, 2003). Similarly, scaling laws have been found to unify low-power accreting BH over many decades in mass (Falcke et al., 2004). The emission models for jets from a supermassive BH have also been successfully applied to an XRB e.g. GRS 1915+105 (Türler et al., 2004).

Comparisons between the jets from different mass BH systems led to Yuan & Zhang (2012) using the nature of episodic jets from AGN and XRBs to explain the erratic light-curves of GRBs. A correlation between blazar jets and GRBs was demonstrated by Nemmen et al. (2012); by considering the mechanical power of GRB and blazar jets P_j, and the collimation corrected γ-ray luminosity L_γ, the relation $P_j \propto L_\gamma^{0.98}$ was found. Blazars and GRBs occupy the low and high ends of the correlation respectively. This result implies that the efficiency of the γ-ray producing

mechanism within these jets is consistent over 10 orders of magnitude in jet power.

There have been several attempts to find a unifying scheme or scaling relation between BH systems where accretion and ejection are at work. Many results have been obtained that separately relate AGN and GRBs, or AGN and XRBs. An attempt to relate all three classes was made recently by Wang & Dai (2017), who used the X-ray and radio luminosities from GRBs and inferred a BH mass to show that the fundamental plane of BH activity (Merloni et al., 2003; Falcke et al., 2004) holds for all jetted BH systems. Also, by considering the bolometric luminosity from jets, Ma et al. (2014) demonstrated that BH XRBs and low-luminosity AGN fit on the $L_\gamma - P_j$ relation for GRBs and AGN. If the $L_\gamma - P_j$ relation is truly universal then the on-axis and collimation corrected γ-ray luminosity and power for the jets from XRBs should fit the same relation as for blazars and GRBs. A fit to this relation could indicate a ubiquitous emission mechanism for all relativistic BH jets and allow for constraints on the high energy emission models for XRBs, AGN, and GRBs.

The XRBs Cygnus X-1 (Bodaghee et al., 2013; Zanin et al., 2016; Zdziarski et al., 2016), Cygnus X-3 (Bodaghee et al., 2013; Corbel et al., 2012), and V404 Cygni (Loh et al., 2016) have been detected at *Fermi* LAT γ-ray energies. A further two sources have *Fermi* LAT upper limits; GRS 1915+105 and GX339-4 (Bodaghee et al., 2013). All of these objects have evidence for a BH component (Tetarenko et al., 2016; Corral-Santana et al., 2016): Cygnus X-1 (Cyg X-1), has a BH confirmed by dynamical modelling (Orosz et al., 2011); Cygnus X-3 (Cyg X-3), has a radio and X-ray correlation which follows that found in BH X-ray binaries (Szostek et al., 2008); V404 Cygni (V404 Cyg) has a BH confirmed by the mass function (Casares & Charles, 1994); GRS 1915+105, the BH is established using a dynamical mass estimate (Reid et al., 2014); GX339-4, the K-correction and model confirm the BH (Muñoz-Darias et al., 2008). Including these XRB on the $L_\gamma - P_j$ universal scaling found by Nemmen

et al. (2012), we make the first attempt, using γ-ray luminosities, at comparing the energetics for three classes of accreting BH systems. The comparison is extended to ~ 17 decades in both γ-ray luminosity and jet power.

In §6.2 the XRB parameters are discussed. §6.3 outlines the method for correcting the γ-ray luminosity and inferred jet power for the inclination and collimation. The results are presented in §6.4. The discussion and conclusion are in §6.5 and §6.6.

6.2 XRB Parameters

The inclusion of XRBs on the $L_\gamma - P_j$ relation requires estimates for the γ-ray luminosity from the relativistic jets, for an on-axis observer, and estimates for the jet power. Unlike blazars and GRBs, the jets from XRBs are not guaranteed to be oriented along the line-of-sight. Any detected emission from an off-axis jet will have to be corrected for the relativistic Doppler effect; this requires knowledge of the system inclination and bulk Lorentz factor Γ. Additionally, any high-energy emission from the jet will be collimated within an angle $1/\Gamma$, which is typically greater than the jet half-opening angle for XRBs. To estimate the jet power we assume equipartion of energy between the particles and magnetic field, and use the optically thin emission during radio flares to find the minimum power. The necessary parameters are: the detected γ-ray photon flux N; the system distance D; the jet inclination i; the jet bulk Lorentz factor Γ; and radio flare peak flux density S_ν, observed frequency ν, and rise time Δt.

Radio emission and flares from XRBs are attributed to relativistic jets. Accretion, seen at X-ray energies, and ejection, seen at radio, are strongly correlated (e.g. Mirabel et al., 1998; Fender & Pooley, 1998; Corbel et al., 2000; Fender, 2001; Corbel et al., 2003; Rodriguez et al., 2003, 2008; Corbel et al., 2013, etc.). The peak flux and rise time of radio flares can be used to constrain the power of a jet. Emission at γ-ray

energies from XRBs has been associated with radio flaring and variability (Corbel et al., 2012). Detection of γ-rays during periods of intense radio flaring suggests the origin of the high energy emission is a jet (Bodaghee et al., 2013). The simultaneous detection of the 511 keV annihilation line and higher energy γ-rays from V404 Cyg within hours of a giant radio flare indicates a jet as the origin of the γ-ray emission (Loh et al., 2016).

XRBs are not persistent γ-ray sources at detection sensitivity, although see Bodaghee et al. (2013) where Cyg X-3 was detected above the background without a flare. Generally XRBs have only been observed at these high energies during flares; therefore we use the detected peak *Fermi* LAT γ-ray photon flux for each source and determine an observed isotropic equivalent γ-ray luminosity $L_{\gamma,\mathrm{obs,iso}}$ from the *Fermi* LAT photon spectral index[1] α at energies > 100 MeV. Detections are in the 0.1-10 GeV range for Cyg X-1 and Cyg X-3 (Bodaghee et al., 2013; Fermi LAT Collaboration et al., 2009), and 0.1-100 GeV for V404 Cyg (Loh et al., 2016). Upper limits for the γ-ray photon flux from GRS 1915+105 and GX339-4, in the energy range 0.1-10 GeV, are used to estimate the maximum $L_{\gamma,\mathrm{obs,iso}}$ for these objects (Bodaghee et al., 2013). The detected peak photon flux and spectral index α, for Cyg X-1, Cyg X-3 and V404 Cyg, and the γ-ray photon flux upper limits for GRS 1915+105 and GX339-4 are shown in Table 6.1.

The photon spectral index is defined as $N_E \propto E^{-\alpha}$, where N_E is in units ph s^{-1} cm^{-2} erg^{-1} and E is the photon energy. The γ-ray luminosity is then,

$$L_{\gamma,\mathrm{obs,iso}} \sim 1.9 \times 10^{35} N_{-6} D_{\mathrm{kpc}}^2 \frac{(\alpha-1)}{(\alpha-2)} \frac{(E_{\mathrm{low}}^{2-\alpha} - E_{\mathrm{high}}^{2-\alpha})}{(E_{\mathrm{low}}^{1-\alpha} - E_{\mathrm{high}}^{1-\alpha})} \quad \mathrm{erg\ s}^{-1}, \qquad (6.1)$$

where E_{low} and E_{high} are the detection band limits in GeV, $N_{-6} = N/(10^{-6}\ \mathrm{ph\ s}^{-1}\ \mathrm{cm}^{-2})$

---

[1] High energy photon spectral index is regularly represented using Γ; to avoid confusion with the outflow bulk Lorentz factor (Γ) we use α throughout

and N is the detected photon flux, and D_{kpc} is the distance in kpc.

The observed proper motion of radio jet components can be used to put constraints on the value of Γ. The proper motion is defined as $\mu = c\beta \sin i/[D(1 \pm \beta \cos i)]$ radians s^{-1}, where $\beta = (1 - \Gamma^{-2})^{1/2}$. An approaching component μ_a has $1 - \beta \cos i$ and a receding component μ_r has $1 + \beta \cos i$. Using resolved μ_a and μ_r, a value for $\beta \cos i$ can be found, where $\beta \cos i = (\mu_a - \mu_r)/(\mu_a + \mu_r)$ (Mirabel & Rodríguez, 1999). Values of $\beta \cos i$ for various XRBs are listed by Miller-Jones et al. (2006) (MFN06 from here). For a system with a known inclination, the observable quantity $\beta \cos i$ can be used to determine the bulk Lorentz factor Γ. Where the inclination is unknown, the Lorentz factor can be determined using the approaching and receding proper motions and the distance to the system. From the product of the proper motions $\mu_a\mu_r$,

$$\Gamma = \left[1 - x^2 - \mu_a\mu_r \frac{D^2(1-x^2)}{c^2} \right]^{-1/2}, \tag{6.2}$$

where x is the observed value $\beta \cos i$, the proper motions μ_a and μ_r are in radians s^{-1}, D is the distance in cm, and c is the speed of light in cm s^{-1}.

If the proper motions of either component are poorly constrained then a limit on Γ can be found by considering the observed jet opening angle ϕ. The angle ϕ is an upper-limit found by measuring the angle between the jet central axis and a tangential line from the edge of a radio component to the system core. The jet components are assumed to be spherical plasmoids that expand uniformly with a co-moving velocity β_{exp}. If we assume maximum co-moving expansion velocity of c, then the jets bulk Lorentz factor is, $\Gamma \gtrsim [1 + \tan^{-2}\phi \sin^{-2}i]^{1/2}$. Where the co-moving expansion velocity is less than the maximum, $\Gamma \gtrsim [1 + \beta_{\mathrm{exp}}^2/(\tan^2\phi \sin^2 i)]^{1/2}$. This assumes no jet confinement.

The inclination i of the system to the line of sight is well constrained for Cyg X-1,

V404 Cyg, and GRS 1915+105 (Orosz et al., 2011; Huppenkothen et al., 2017; Reid et al., 2014, respectively). Cyg X-3 and GX339-4 have unknown system inclinations. For Cyg X-3; Dubus et al. (2010) showed that the jet orientation within the system is constrained to be between $20° \lesssim \theta_j \lesssim 80°$, and the system line-of-sight inclination is $i = 30°$. Vilhu & Hannikainen (2013) used an inclination of $i = 30°$ in their models. Using the $\beta \cos i$ values in MFN06 and the distance to the system, the bulk Lorentz factor Γ of the jet can be constrained. Given $\beta \cos i = 0.5$, $\mu_a \mu_r \sim 7.4 \times 10^{-26}$ rads s^{-1}, and $D = 7$ kpc, the bulk Lorentz factor is $\Gamma = 1.18$ and the line of sight inclination to the jet-axis is $i \simeq 20°$. For GX339-4; MFN06 measured $\beta \cos i \geq 0.16$ and derived a $\Gamma \geq 4.9$ from the jet opening angle; a lower limit of $\Gamma \geq 2.3$ is used by Fender et al. (2004). Using these values for Γ, the inclination of the system can be determined from $\beta \cos i = 0.16$; for $\Gamma = 4.9$ the inclination is $i = 80°.6$; for $\Gamma = 2.3$ the inclination is $i = 79°.8$. In all cases we assume that the inclination angle is the same as the line-of-sight angle to the jet axis and that there is no significant precession. Values for the inclination are listed in Table 6.1.

XRB jets typically have $\Gamma < 5$. For Cyg X-1 a Lorentz factor $\Gamma = 1.25$ is used by Pepe et al. (2015) for modelling the lepto-hadronic broadband emission, whilst from the jet opening angle and $\beta \cos i$ from MFN06, there is a minimum value of $\Gamma = 3.3$. We show results for both values. For Cyg X-3 the Lorentz factor must be $\Gamma \leq 2$ (MFN06); we derived the value $\Gamma = 1.18$ (equation 6.2). We show results for $\Gamma = 2$ and $\Gamma = 1.18$. For V404 Cyg we assume a Lorentz factor $\Gamma = 2.3$ (Tanaka et al., 2016). For GRS 1915+105, from the inclination $i = 60°$ and $\beta \cos i = 0.41$ we derive a $\Gamma = 1.75$. For GX339-4, we use the value $\Gamma = 4.9$ from the jet opening angle.

We assume that γ-ray emission, and radio flares are from the jet with negligible contribution from the accretion disk or star. The peak radio flare flux density S_ν, the rise time Δt, frequency ν, and distance D are shown with references in Table 6.1.

Table 6.1: XRB parameter values used to determine the luminosity, power, and Doppler- and collimation-corrected luminosity. Values in brackets are assumed. The derived luminosity and power values for the sample of XRB. The observed γ-ray luminosity $L_{\gamma,\mathrm{obs,iso}}$ is determined from the *Fermi* LAT photon flux and spectral index. The minimum jet power P_j, and the Doppler- and collimation-corrected luminosity L_γ are shown; where two values are present, the first is for the lower Lorentz factor in the parameters, the second for the highest. References: [1] Pepe, Vila & Romero 2015. [2] Dubus, Cerutti & Henri 2010. [3] Tanaka et al. 2016. [4] Miller-Jones, Fender & Nakar 2006. [5] Bodaghee et al. 2013. [6] Fermi LAT Collaboration 2009. [7] Loh et al. 2016. [8] Reid et al. 2011. [9] Huppenkothen et al. 2017. [10] Fender, Belloni & Gallo 2004. [11] Orosz et al. 2011. [12] Ling, Zhang & Tang 2009. [13] Zdziarski et al. 2016. [14] Corbel et al. 2012. [15] Reid et al. 2014

Parameter	Cyg X-1	Cyg X-3	V404 Cyg	GRS1915+105	GX339-4
Γ	$1.25_{[1]}$-$3.3\pm0.1_{[4]}$	$1.2_{[2,4]}$-$2.0\pm0.1_{[4]}$	$2.3\pm0.5_{[3]}$	$1.75_{[4]}$	$4.9_{[4]}$
N_γ ($\times10^{-6}$ ph cm^{-2} s^{-1})	$1.4 \pm 0.4_{[5]}$	$3.5 \pm 0.5_{[14]}$	$2.3 \pm 0.8_{[7]}$	$< 0.023 \pm 0.017_{[5]}$	$< 0.016 \pm 0.010_{[5]}$
α (ph spec. index)	$2.4_{[13]}$	$2.7_{[6]}$	$2.5_{[7]}$	(2.5)	(2.5)
D (kpc)	$1.86 \pm 0.12_{[8]}$	$7.0 \pm 0.4_{[12]}$	$2.39 \pm 0.14_{[9]}$	$9 \pm 2_{[15]}$	$8 \pm 2_{[10]}$
i (°)	$27.1 \pm 0.8_{[11]}$	$20 \pm 2_{[2,4]}$	$67 \pm 2_{[9]}$	$60 \pm 5_{[15]}$	$80.2 \pm 0.4_{[4]}$
S_ν ($\times10^3$ mJy)	$0.028_{[10]}$	$13.4_{[4]}$	$3.4_{[7]}$	$214_{[10]}$	$55_{[10]}$
ν (GHz)	5.0	5.0	13.9	5.0	5.0
Δt ($\times10^4$ s)	$0.2_{[10]}$	$30_{[4]}$	$6.9_{[7]}$	$4.32_{[10]}$	$1.98_{[10]}$
$L_{\gamma,\mathrm{obs,iso}}$ ($\times10^{35}$ erg s^{-1})	2.70 ± 0.34	76.6 ± 8.75	7.30 ± 0.86	1.00 ± 0.43	0.50 ± 0.26
L_γ ($\times10^{36}$ erg s^{-1})	0.13 ± 0.02	3.16 ± 0.60	18.8 ± 2.20	0.54 ± 0.24	70.0 ± 35.8
	0.42 ± 0.08	2.52 ± 0.64			
P_j ($\times10^{37}$ erg s^{-1})	0.03 ± 0.01	20.7 ± 4.89	17.3 ± 12.23	4.90 ± 3.42	30.7 ± 4.20
	0.02 ± 0.01	7.70 ± 1.98			

6.3 Method

We use the *Fermi* LAT measured γ-ray photon flux for three XRBs: Cygnus X-1 (Bodaghee et al., 2013), Cygnus X-3 (Fermi LAT Collaboration et al., 2009), and V404 Cygni (Loh et al., 2016). These are currently the only γ-ray detected XRBs. *Fermi* LAT upper limits exist for GRS 1915+105 and GX339-4 (Bodaghee et al., 2013); the upper limits are used for these objects. Cynus X-3 and V404 Cygni have also been detected at > 100 MeV by AGILE (Tavani et al., 2009; Piano et al., 2017). The high energy emission is associated with jet activity.

Emission from a relativistic jet is beamed in the direction of the jet bulk motion; we assume a point like emission region on the jet axis for all high energy photons. The γ-ray luminosity is corrected for the inclination of the jet to the line of sight. The Lorentz invariant quantity I_ν/ν^3 (Rybicki & Lightman, 1986), where I_ν is the specific

intensity and ν the frequency, can be used to determine the specific luminosity from a relativistic source where the observer is outside the relativistic beaming angle. As $\nu = \delta\nu'$, where $\delta = [\Gamma(1 - \beta\cos i)]^{-1}$ is the relativistic Doppler factor, Γ the bulk Lorentz factor, i the inclination, and primed quantities are in the co-moving frame, then $I_\nu = I'_{\nu'}(\nu/\nu')^3 = I'_{\nu'}\delta^3$. The observed luminosity is then $L_\nu = 4\pi I'_{\nu'}\delta^3$. For an on-axis observer the Doppler factor becomes $\delta = [\Gamma(1-\beta)]^{-1}$; the observed luminosity is then a^3 times the on-axis luminosity (Granot et al., 2002), where a is the correction for an on-axis observer to an off-axis observer; the factor $a = (1 - \beta)/(1 - \beta\cos i)$.

The γ-ray luminosity for an on-axis observer has detection band limits a factor a^{-1} times the off-axis detection limits; a correction to the on-axis Doppler boosted emission should be made to ensure the detection band is consistent. All the γ-ray detections have a single power-law spectral fit with a νF_ν index $2 - \alpha$, and no information of a spectral peak or behaviour at lower energies. A peak for the γ-ray component should exist at a few GeV (e.g. Zdziarski et al., 2014) for an on-axis observer; we therefore assume a flat spectrum for the correction. The on-axis isotropic equivalent γ-ray luminosity is then $L_{\gamma,\text{iso}} = a^{-3}\,L_{\gamma,\text{obs,iso}}$, where $L_{\gamma,\text{obs,iso}}$ is the observed isotropic equivalent γ-ray luminosity, equation 6.1. The collimation-corrected luminosity is $L_\gamma = f_b\,L_{\gamma,\text{iso}}$, where f_b is the collimation factor for the jet. The collimation-correction is $f_b = 1 - \cos(1/\Gamma)$. The intrinsic, on-axis γ-ray luminosity is then $L_\gamma = f_b\,a^{-3}\,L_{\gamma,\text{obs,iso}}$.

Bright radio flares from plasmoids that travel along the relativistic jet structures can be used to estimate the minimum power of the jet. Although γ-ray emission is often correlated with radio flaring, the site of the emission within the jet is distinct. Radio flares are contained by the plasmoids and equipartition of the energy within these structures can be assumed. The jet power is estimated by assuming equipartition of energy between the synchrotron emitting particles and the magnetic field strength

B (Burbridge, 1956, 1959; Longair, 1994; Lewin & van der Klis, 2006). The energy density in the particles, given a random magnetic field, is $e \propto B^{-3/2}$, and the energy density in the magnetic field is $u \propto B^2$. The total energy is $E_{\text{total}} = V(e + u)$, where V is the volume of the emitting region; as the dominant component is unknown i.e. large B and small e, or small B and large e, then a minimum energy can be found at the point where $dE_{\text{total}}/dB = 0$. The particle number density assumes a power-law distribution of ultra-relativistic electrons $n_e \propto E^{-p}$; the contribution from relativistic protons is included by the factor $\eta = 1 + \epsilon_p/\epsilon_e$, where ϵ_p is the energy in protons and ϵ_e is the energy in electrons. The energy in the particles is $E = C(p, \nu)\eta L_\nu B^{-3/2}$, where L_ν is the co-moving specific luminosity and $C(p, \nu)$ is a constant that depends on the particle index p, the frequency ν of the specific luminosity, and the upper and lower synchrotron frequency limits for the particle distribution (Longair, 1994).

For a distribution of particles with a power-law index $p > 2$, the low energy particles dominate. By assuming that $\nu = \nu_{\text{min}}$, the minimum synchrotron frequency, a simple estimate for the energy in the system can be made[2]. We assume a particle distribution, in all cases, of $p = 2.5$ (Sironi & Spitkovsky, 2011); the observed flux density S_ν would have a spectral index of 0.75, where $S_\nu \propto \nu^{-0.75}$. The volume of the emitting system is assumed to be spherical, where the size can be inferred from the light crossing time indicated by radio flare rise time Δt; the volume is then $V = 4\pi(\Delta t c)^3/3$. The jet-power $P_j = E_{\text{total}}/\Delta t$ can then be estimated by considering the Doppler corrected observed flux density; for an optically thin source the Doppler correction to the flux density is $\delta^{3+(p-1)/2}$ (Blandford & Königl, 1979).

The jet power P_j is a Lorentz invarient quantity, therefore the observed flux density, time, and frequency must be co-moving quantities. The flux dependence is $S'_{\nu'} = \delta^{-(3+(p-1)/2)}S_\nu$, the time is $\Delta t' = \delta \Delta t$, and frequency $\nu' = \delta^{-1}\nu$. The jet power is

---

[2] This assumes no large flux of low energy relativistic particles with a different energy spectrum

then,

$$P_j \sim 3.5 \times 10^{33} \, \eta^{4/7} \, \Delta t'^{2/7} \, \nu'^{2/7}_{\text{GHz}} \, S'^{4/7}_{\nu',\text{mJy}} \, D^{8/7}_{\text{kpc}} \quad \text{erg s}^{-1}, \tag{6.3}$$

where, $\Delta t'$ is in seconds, ν' is in GHz, $S'_{\nu'}$ is in mJy, and D is in kpc. We assume equal energy in protons and electrons, $\epsilon_p/\epsilon_e = 1$.

Uncertainties on the derived values are estimated by propagating the uncertainty on the distance, the inclination, the γ-ray flux, and the bulk Lorentz factor. The uncertainty on Γ is assumed to be $d\Gamma = 0.1$ for Cyg X-1, Cyg X-3, GRS 1915+105, and GX339-4 where the estimate for Γ is from observed proper motions, and $d\Gamma = 0.5$ for V404 Cyg where Γ is found from a model jet velocity. The choice of uncertainty for Γ reflects the estimation method and a conservative value for the minimum precision. The error on the final parameters is dominated by the uncertainty in the γ-ray flux and is only very weakly dependent on the choice of $d\Gamma$.

6.4 Results

Figure 6.1 shows the $L_\gamma - P_j$ relation for the sample of XRBs. The observed luminosities (filled markers) and collimation/Doppler-corrected values (unfilled markers) are both shown. Values for Cyg X-1 are blue squares; Cyg X-3 are red diamonds; and V404 Cyg, are pink stars. For Cyg X-1; the small unfilled marker is the estimate based on $\Gamma = 1.25$, the large marker is $\Gamma = 3.3$. For Cyg X-3; the small unfilled marker is $\Gamma = 1.18$, and the large $\Gamma = 2$. For V404 Cyg, there is only one estimate for the bulk Lorentz factor used. GRS 1915+105 is an upward pointing black triangle. GX339-4 is a downward pointing black triangle. Errorbars are those derived from the quoted uncertainties or 0.5 dex where propagated errors are large. The parameters used for the XRB sample, and the derived luminosity and power, are listed in Table 6.1.
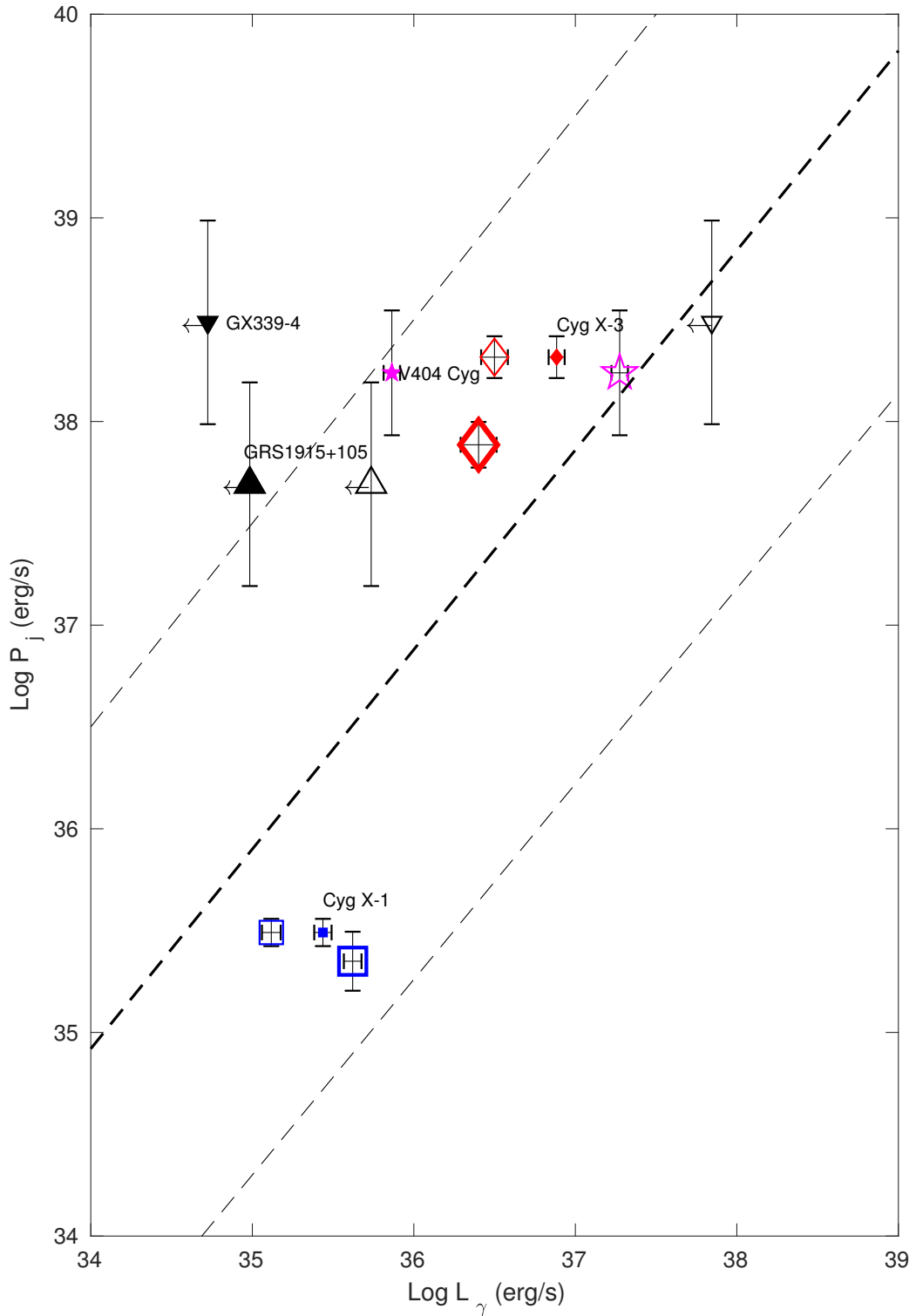
Figure 6.1: XRB $L_\gamma - P_j$ diagram: Cyg X-1 blue squares; Cyg X-3 red diamonds; V404 Cyg pink stars; GRS 1915+105 black upward-pointing triangle; GX339-4 black downward-pointing triangle. Filled markers represent observed values with no L_γ correction for collimation and Doppler-factor - where two values of Γ are listed, the lowest value is used in determining the jet power. Unfilled markers represent the collimation- and Doppler-corrected values - small markers represent the lower Γ value, large marker represents the larger Γ value. Black solid lines indicate the uncertainties calculated for each value. L_γ for GRS1915+105 and GX339-4 are upper limits. The dashed line is the $L_\gamma - P_j$ relation found by Nemmen et al. 2012 for Blazars and GRBs; the dotted lines are their uncertainties.

6.5 Discussion

Using the observed peak *Fermi* LAT γ-ray flux or upper limit, the jet to line-of-sight inclination, and the jet Lorentz factor, we have made estimates for the on-axis, isotropic equivalent γ-ray luminosity from the jets of five XRBs. The isotropic on-axis luminosity is further corrected for the collimated emission, where the fraction is given by $1 - \cos(1/\Gamma)$, resulting in a collimation-corrected estimate for the γ-ray luminosity. This γ-ray luminosity, along with an estimate for the jet power, can be directly compared with the universal scaling for relativistic jets from BH systems proposed by Nemmen et al. (2012). The Nemmen relation is based on the peak γ-ray luminosity and jet power for blazars and γ-ray bursts (GRB). The inclusion of XRBs on this plot, extends this $L_\gamma - P_j$ relation to lower luminosities and power. The XRB fit on this plot can also be used to indicate the jet origin of γ-ray photons from such sources.

The γ-ray luminosity for the three source types, blazars, GRBs, and XRBs, is the beamed on-axis and collimation corrected luminosity. The jet power is estimated for each source type uniquely: for blazars, the jet power is found from a tight correlation between the radio luminosity and the power required to inflate an X-ray cavity (Cavagnolo et al., 2010). Using the relation $P_j \sim 6 \times 10^{43} L_{40}^{0.7}$ erg s^{-1}, where L_{40} is the radio luminosity in units $\times 10^{40}$ erg s^{-1}, the power for blazars with VLA observed extended radio emission was determined; for GRBs, the jet power is found using a collimation corrected estimate for the kinetic energy from the peak of the radio or X-ray afterglow and assuming the fireball model. The jet power is then $P_j = (1 + z) f_b E_{k,\mathrm{iso}} / t_{90}$, where f_b is the collimation correction, $E_{k,\mathrm{iso}}$ the isotropic equivalent kinetic energy, and t_{90} the timescale for 90% of the prompt emission energy; for XRBs, the jet power is found using the minimum energy assuming equipartition and the peak radio flare flux density. The jet power is given by equation 6.3. Our estimates for the Doppler- and collimation-corrected γ-ray luminosity and jet power, for the five XRBs in our

sample, all fall within the uncertainties associated with the original $L_\gamma - P_j$ relation for BH jets: $\log P_j = (0.98 \pm 0.02) \log L_\gamma + (1.6 \pm 0.9)$ erg s^{-1}.

The $L_\gamma - P_j$ correlation can be applied to XRBs without a limit on the γ-ray luminosity. There are at least four additional XRBs with peak radio flare flux densities, rise times, $\beta \cos i$, and distance measurements: GRO J1655-40, V4641 Sgr, XTE J1550-564, and H 1743-322. All have BH components (Corral-Santana et al., 2016; Tetarenko et al., 2016). The distances to these systems are: GRO J1655-40 is at 3.2 kpc (Hjellming & Rupen, 1995); V4641 Sgr is at 6.2 kpc (MacDonald et al., 2014); XTE J1550-564 is at 4.5 kpc (Orosz et al., 2011); H 1743-322 is at 10 kpc (Shaposhnikov & Titarchuk, 2009; McClintock et al., 2009). Given the $\beta \cos i$ and $\mu_a \mu_r$ values in MFN06, the bulk Lorentz factors are $\Gamma = [2.5, \geq 2.5, 1.3, 3.7]$ respectively. The power of the jet for these systems, using the rise time and peak flux listed in MFN06 for GRO J1655-40, V4641 Sgr, and XTE J1550-564, and the rise time and peak flux from McClintock et al. (2009) for H 1743-322, is then $P_j = [2.93, 1.05, 0.04, 8.33] \times 10^{38}$ erg s^{-1} respectively. The $L_\gamma - P_j$ relation can give us contraints on the on-axis γ-ray luminosity. As the observed upper limit for γ-ray luminosity is $L_{\gamma,\text{obs,iso}} = f_b^{-1} a^3 L_\gamma$, using equation 6.1, the maximum γ-ray photon flux at a detector for each source is: $N_\gamma \leq [1.6, 0.5, 2.8, 0.1] \times 10^{-8}$ photons s^{-1} cm^{-2} respectively, at energies > 100 MeV and assuming $\alpha = 2.5$.

The inclination angle used for the relativistic Doppler correction is in all cases assumed to be the angle from a point source on the jet-axis to the line-of-sight. However, the jets have a finite opening angle ϕ; the angle to the jet could be as low as $(i - \phi)$. The Doppler corrected luminosity will be lower in each case than those presented here. Cyg X-1 and Cyg X-3 have relatively small inclination angles, $27°.1$ and $\sim 20°$, and jet opening angles, $< 18°$ and $< 16°.5$ respectively. The Doppler and collimation corrected values for each system using $(i - \phi)$ are shifted to lower γ-ray luminosities. For

Cyg X-1, $L_\gamma \sim 2.5 \times 10^{34}$ erg s^{-1} when $\Gamma = 3.3$, and for both Γ values used here is closer to the central $L_\gamma - P_j$ trend. For Cyg X-3, $L_\gamma \sim 10^{36}$ erg s^{-1} for $\Gamma = 2$, and for both Γ values used is well within the correlation limits.

However, note that the Doppler-corrected γ-ray energies for the five XRBs are most likely underestimates; this is due to the shift of the observed *Fermi* LAT band > 100 MeV, to the on-axis energy range, where $\nu_{\rm obs} = a\nu_{\rm o}$ and $\nu_{\rm o}$ is the value to an on-axis observer. The observed *Fermi* LAT spectrum, in all cases, is assumed to be a single power law; without information regarding the spectral peak or index below the observed minimum energy 100 MeV, we have assumed the on-axis γ-ray luminosity to be equivalent to the energy in the Doppler-corrected band i.e. a flat spectrum. If the single power-law extended to lower energies than those observed by *Fermi* LAT then the on-axis Doppler corrected luminosities would be of order $L_\gamma \sim 10^{41}$ erg s^{-1}; such a bright on-axis source could be detectable as a γ-ray transient in local galaxies e.g. $N_\gamma \sim 2 \times 10^{-6}$ ph s^{-1} cm^{-2} at 1 Mpc, and becoming limited at $N_\gamma \sim 2 \times 10^{-8}$ ph s^{-1} cm^{-2} at 10 Mpc.

To estimate the minimum power of the jet we have assumed a ratio of energy in relativistic protons to electrons in the synchrotron emitting region of $\epsilon_p/\epsilon_e = 1$. This ratio could in reality be very small or as high as ~ 100 e.g. GRBs, where the ratio is typically in the range $10 \lesssim \epsilon_p/\epsilon_e \lesssim 100$. If the energy in the hadronic particles is larger, the jet powers presented here would be underestimates; for $\epsilon_p/\epsilon_e = 2$ the jet power would increase by a factor of ~ 1.3, for $\epsilon_p/\epsilon_e = 100$ the power would be ~ 9.4 times those presented here. Alternatively, if the energy in relativistic protons is very small, then the jet power would be ~ 0.7 of those presented. As noted by Zdziarski (2014), this method does not consider the contribution by cold ions in the jet bulk flow to the total power. The minimum jet powers presented here are therefore underestimates; the maximum correction factor to the presented powers is a factor

~ 50 larger. If the minimum jet powers presented here are massively underestimated, then by considering similar arguments for the underestimate of the jet power in blazars (e.g. Ghisellini, 1999) the $L_\gamma - P_j$ correlation may still hold but with a shallower index.

Figure 6.2 shows the Nemmen et al. (2012) distribution of blazars and GRBs with the uncertainties for each population, plus the five XRBs presented here. Where two estimates for the Doppler-corrected luminosity and power exist for an XRB, we have used the values that correspond to the largest Γ. The addition of more XRBs to this distribution will help to determine the validity of the correlation, and if it holds, better constrain the index and limits for a wide range of BH jets in $L_\gamma - P_j$.

Ma et al. (2014) found a similar correlation for XRBs in the hard state using the bolometric luminosity for the jet derived from models; the power estimates for the jets in their sample were typically lower than those found here by up to 3-4 orders of magnitude. Our estimates are based on the minimum jet power during a flaring/transient event as opposed to the compact jets seen during the hard state; this difference can explain the disagreement in jet power where the same source is compared. The luminosity used in our sample is the γ-ray flare luminosity not the hard-state bolometric jet luminosity and therefore our estimates are directly comparable to the original Nemmen et al. (2012) correlation.

That Ma et al. (2014) find a correlation without using γ-ray luminosity demonstrates that a common mechanism links all BHs and jets through accretion with very small differences. By considering only the γ-ray flux from these jets we can probe the part of the outflow with the highest Lorentz factor and strongest relativistic beaming. For GRBs, the emitted γ-rays are a small fraction of the total engine energy; despite the differences in these sources (stellar mass BH in XRBs, SMBH in AGN, or SNe/merger for GRBs) the observed relation is always the same. A confirmed correlation for $L_\gamma - P_j$ for jets from accreting BH systems, regardless of phenomenological
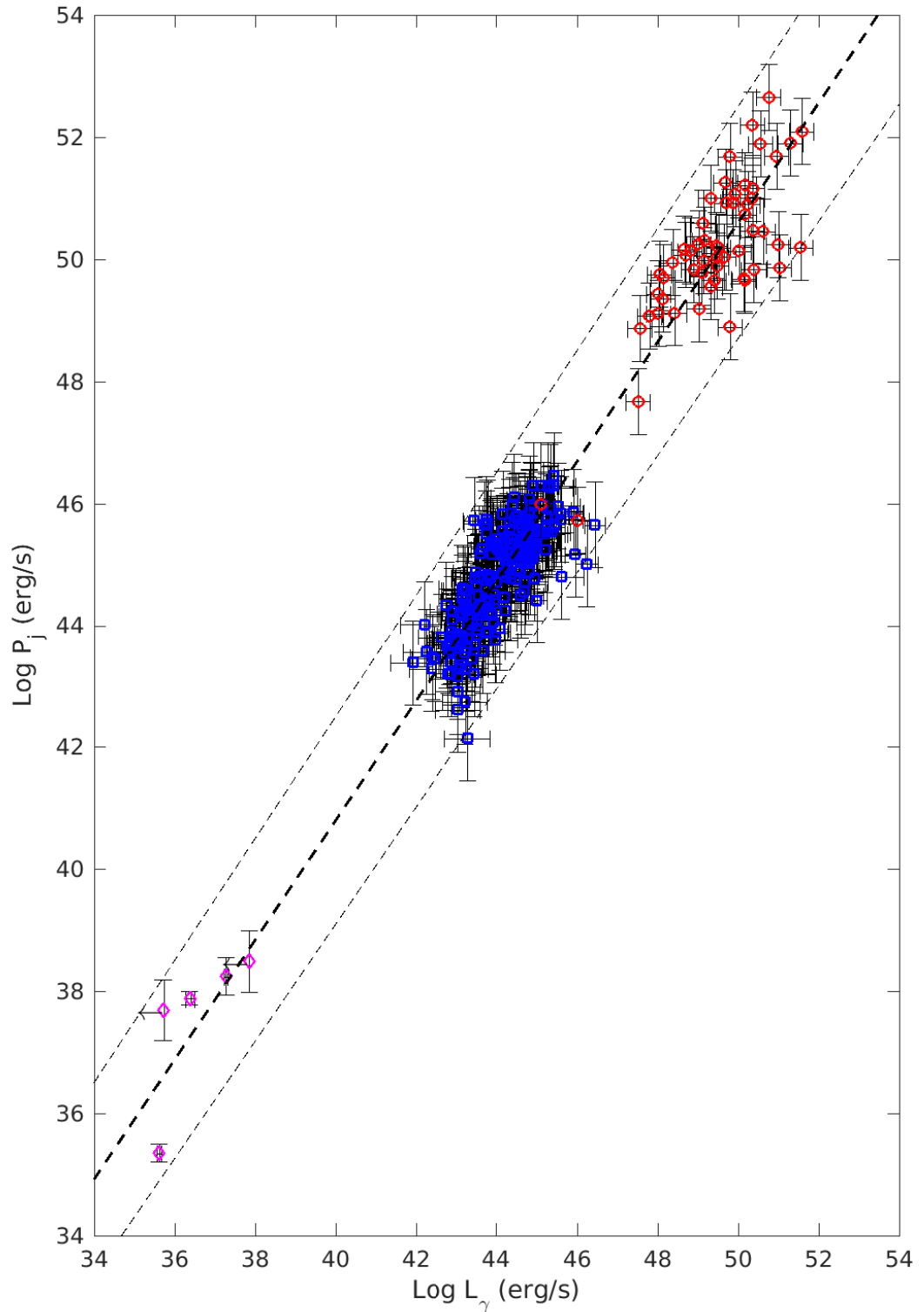
Figure 6.2: $L_\gamma - P_j$ relation including five XRBs. Doppler- and collimation-corrected luminosity and power estimates are shown for XRB (pink diamonds), using the larger Γ value where appropriate. Values for blazars are shown as blue squares, and γ-ray bursts are shown as red circles, where the data and uncertainties are from Nemmen et al. 2012. Dashed black line is the $L_\gamma - P_j$ relation, thin dashed lines represent the limits from Nemmen et al. 2012.

differences between the systems, could help determine a ubiquitous emission mechanism for high energy photons from such jets. The existence of a correlation across extremes of time and mass scale points to common physical phenomena between all relativistic BH jets. If all relativistic BH jets have the same high-energy emission mechanism then the differences between the system classes can be used to constrain the emission mechanism at γ-ray energies. Alternatively, the correlation may indicate that the efficiency for various γ-ray emission processes in relativistic jets is similar.

Two groups of models are used to explain the high energy emission in XRBs and blazars: the hadronic/lepto-hadronic models, where the high energy emission is from internal jet processes such as synchrotron self Compton (SSC), synchrotron of protons or the decay of neutral pions from proton-proton cascade; and the leptonic models, where high energy emission is due to the external Compton scattering by relativistic electrons of a strong photon field, either from stellar companion black-body photons or X-ray photons from the accretion disk for XRBs, or the accretion disk and broadline region for blazars.

Strong polarization measurements made in the γ-ray tail of Cyg X-1 favour a lepto-hadronic model, and a jet origin, for the high energy emission (Rodriguez et al., 2015). Lepto-hadronic models for the broadband emission of Cyg X-1 by Pepe et al. (2015) also favours a synchrotron or SSC, and therefore jet origin, for the high energy tail. The low mass of the companion to V404 Cyg, the temporal association of γ-ray excess and radio flares, and the simultaneous detection of the 511 keV annihilation line and γ-rays of higher energy all point to the jet as the origin for such emission (Loh et al., 2016). For blazars, the jet as the origin for the high energy emission is supported by long-term monitoring campaigns which indicate a correlation between γ-ray flares and optical flares; the optical emission from blazars is polarized to different degrees depending on the location of the synchrotron peak relative to the observed

optical bands (Jermak et al., 2016); optical and γ-ray flares, and high polarizations, are associated with the jet where observed polarization rotations can be explained by a structured magnetic field within the jet and used to support a lepto-hadronic model for the high energy emission (Böttcher et al., 2013; Böttcher, 2016). Similarly, polarization measurements of the early afterglow in GRBs indicates the existence of an ordered magnetic field in a magnetized baryonic jet (Steele et al., 2009; Mundell et al., 2013). Alternatively, if high energy emission from AGN and XRBs is due to a leptonic process i.e. inverse Compton scattering of external photons, then this correlation may have implications for the emission mechanism responsible for the high-energy prompt GRB. For a long GRB the target photons may be from shock breakout, early supernova photosphere photons, or the photons of a companion star whose presence may be inferred by the high degree of stripping of long GRB progenitor supernovae i.e. Ic SNe.

Throughout, we have made the assumption that all GRBs are powered by BH, as opposed to magnetars; the overall $L_\gamma - P_j$ correlation presented here may support this assumption. XRBs, blazars, and GRBs all populating the same relation for $L_\gamma - P_j$ indicates a common jet emission mechanism, or efficiency, for γ-rays where the magnitude of L_γ depends on the jet power.

6.6 Conclusions

We have shown that when corrected for collimation and Doppler boosting, the γ-ray luminosity from XRBs follows the $L_\gamma - P_j$ relation found by Nemmen et al. (2012) for relativistic jets from BH systems. This correlation holds across ~ 17 orders of magnitude and is the first attempt at comparing the energetics, using γ-ray luminosities, for three classes of accreting BH systems e.g. XRB, AGN, and GRB. Although

the jet powers and γ-ray luminosities for XRBs are most likely underestimates, XRBs are relatively closely grouped in the parameter space. The power of a jet from a BH system can be independently constrained by the on-axis γ-ray luminosity. Alternatively, the jet power can be used to indicate the expected on-axis γ-ray luminosity for high energy flares from BH jets. Future target of opportunity high energy observations of XRB during radio flaring events could help further constrain this relation. If such a relation is ubiquitous amongst relativistic jets from BHs, then a common emission mechanism, or efficiency, is most likely responsible. Where the efficiency here is in the range $0.2 \leq \eta \leq 0.995$, and $\eta = L_\gamma/(P_j + L_\gamma)$ By comparing the different systems, constraints can be put on the emission dynamics.

7. Conclusions and Future Work

The aim of this thesis is to give a qualitative indication of the various dynamical and structural jet properties that can be revealed by the observation of electromagnetic jet counterparts to gravitational wave detected neutron star mergers. This is motivated by the opportunity that GW triggered detections give in probing the afterglow of merger-jets and the possibilty of revealing a hidden population of low Γ failed GRB jets or the intrinsic jet structural properties that cannot be revealed by GRB triggered afterglow observations. These results will help constrain the physical mechanism that launches and accelerates relativistic jets from compact merger objects, and can potentially give insight into how the mechanism works in the jets from other systems e.g. X-ray binaries and AGN.

7.1 Conclusions

EM counterparts from relativistic merger-jets accompanying GW detected NS/BH-NS mergers will reveal the structure and dynamic properties of short GRB jets. If a significant fraction of merger-jets result in low Γ outflows, a hidden population of afterglow-like transients will be revealed. Such a population can be used to constrain the Lorentz-factor distribution for the population of merger-jets. Alternatively, the X-ray, optical, and radio frequency afterglows from jets viewed at inclinations $\sim 20 - 40°$

will reveal the presence of structure from the features and temporal behaviour in the light curve. Sharp light curve peaks, re-brightening of the afterglow during the decline after peak, or a shallow rise pre-peak are all signatures of structured jets viewed at an inclination greater than the jet core angle.

The sub-luminous γ-ray burst associated with GW 170817, GRB 170817A, is not easily explained with a traditional jet origin, however if such a GRB accompanies the majority of NS mergers then the emission can be considered quasi-isotropic and is likely to have an origin as either scattered prompt emission (Kisaka et al., 2017) or another flaring mechanism e.g. shock breakout or reconnection. The afterglow detection from $\sim 10 - 100$ days post-merger for GW 170817 is consistent with a Gaussian structured jet viewed at an inclination $\sim 20°$; see Figure 7.1 for the light curve and spectra at 15 and 108 days including X-ray, optical, IR and radio frequency observations (Lyman et al., 2018). Further GW detections will reveal if such a jet structure is a universal feature for short GRB jets.

A population of failed-GRBs from merger-jets, or the presence of extended jet structure beyond a γ-ray bright jet core will increase the rate of optical transients in an untriggered deep, $m \lesssim 26$, optical survey. If the Gaussian structure is seen to be a universal feature for short GRB jets, then the transient rate at $m_{\mathrm{AB}} \gtrsim 23$ for orphan afterglows in untriggered surveys will be above that expected from a simple homogeneous jet model alone.

This thesis presents estimates for the expected rates of various jet afterglow transients given a GW detection and a variety of jet dynamical and structural models. The observation of failed-GRB afterglows will indicate a hidden low Γ jet population that can be used to constrain the Lorentz-factor distribution for merger-jets. The off-axis light curves for various structured jet models give an indication of the various phenomenological features that can be used to distinguish between the various models.
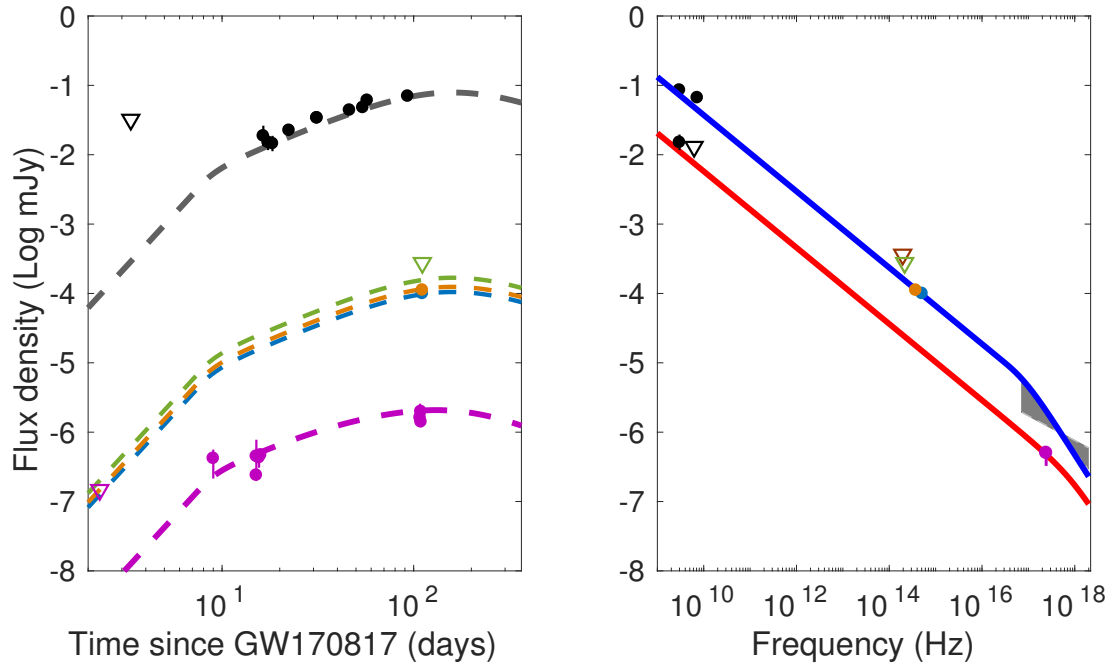
Figure 7.1: The observed light curve and spectral energy distribution of the afterglow at radio, optical, and X-ray wavelengths for GRB 170817A can be described by an off-axis structured jet. Left panel: Off-axis afterglow light-curve. Thick dashed grey and dashed purple lines indicate 3 GHz and 1 keV flux density respectively, overlaid with radio (Hallinan et al. 2017, Mooley et al. 2017) and X-ray data (Margutti et al. 2017, Haggard et al. 2017, Troja et al. 2017, Ruan et al. 2017). Upper limits are shown as triangles. The green dashed line indicates the *HST* near IR F140W frequency while the blue dashed and orange dashed lines show *HST* optical F606W and F814W fluxes. Optical detections are indicated as error bars on the optical light curves and near IR flux limits as open triangles. Right panel: The model spectra at 14.9 days (red) and 108 days (blue) post-merger compared to radio (Hallinan et al. 2017, Mooley et al. 2017) and X-ray data (Haggard et al. 2017, Ruan et al. 2017). The X-ray flux at 15 days is shown at 1 keV as an error bar and at 108 days as a spectral slope due to better spectral index constraints; the grey shaded region indicates the 1σ bounds on the slope (Ruan et al. 2017). All uncertainties are shown as 1σ, and some error bars are smaller than the marker.

The intrinsic jet structure has an implication for the rates of detectable orphan afterglows and can be used to give constraints on the local NS merger rates.

7.2 Future Works

The prompt emission for a low Γ jet or jet component in Chapters 2 and 3 makes some basic assumptions about the opacity and the emission at the photosphere. By inclusion of a more sophisticated radiative transfer model the precise nature of the prompt emission from a low Γ region can be more reliably investigated. This may have implications for the origin of X-ray flashes from both short and long GRB progenitors.

The current structured jet light curve estimates, shown in Chapter 3, are based on a few simple assumptions that give the general qualitative behaviour of the various structured jet models but cannot accurately constrain the exact parameter values given an observational fit. To improve the parameter estimates the afterglow model will have to include consideration of the entire emitting volume and the exact hydrodynamics of the emitting region. At present the emission is assumed to be from a surface at the shock front; the timescales for emission from a volume should be lengthened from those indicated by considering only a single surface, while the timescale should be shortened by considering the dynamics of the emitting region i.e $\gamma_1 = \sqrt{2}\Gamma(t)$. The model assumes a balance between these two effects. This assumption should be checked and the model improved by inclusion of the emitting volume and the hydrodynamical details of the forward shock region.

Reverse shock emission from a structured jet has not been considered. Adding a reverse shock component to the structured jet afterglow lightcurves will provide an understanding of the expected afterglow temporal and spectral behaviour at various inclinations. Understanding how the reverse shock behaves for either a thick or thin

shell in a structured relativistic outflow would enable the interpretation of optical and radio counterpoints from a jet to gravitational wave detected mergers.

The afterglow light curve model can be further improved by considering the point at which the outflow becomes Newtonian. The current version follows a Blandford & McKee (1976) solution until $\Gamma = 1$, in reality the transition may occur earlier than this (e.g. Kobayashi et al., 1999). The counterjet may also become visible once the evolution becomes spherical and this should be included to give accurate late time light curves, particularly important for radio observations. Additionally, the jet is assumed to always be confined i.e. no sideways expansion, although this is valid for the early evolution (van Eerten & MacFadyen, 2012) the jet may start to expand sideways at later times. Such sideways expansion will effect the late time post jet-break evolution, where the decline is steeper. By producing a light curve model that can include sideways expansion as an option the late time evolution of an afterglow can be better modelled. These improvements would allow the more accurate determination of the various jet parameters from observations.

A more detailed investigation of the emission characteristics of γ-rays from the various black hole jet systems will help determine if the universal scaling, observed to hold for GRBs, XRBs, and AGN, is due to intrinsic similarities in the emission process, or whether the scaling is purely due to the available efficiency for various emission processes. If this scaling pertains to a similar emission process in all systems, then a contrast of the differences will help constrain the physical processes that are responsible.

References

Aasi, J., Abadie, J., Abbott, B. P., et al. 2013, Phys. Rev. D, 88, 062001

Abadie, J., Abbott, B. P., Abbott, R., et al. 2010, Classical and Quantum Gravity, 27, 173001

Abbott, B. P., Abbott, R., Abbott, T. D., et al. 2016a, Living Reviews in Relativity, 19, 1

Abbott, B. P., Abbott, R., Abbott, T. D., et al. 2016b, Physical Review X, 6, 041015

Abbott, B. P., Abbott, R., Abbott, T. D., et al. 2017a, Phys. Rev. Lett., 118, 221101

Abbott, B. P., Abbott, R., Abbott, T. D., et al. 2017b, Phys. Rev. Lett., 119, 141101

Abbott, B. P., et al., (LIGO Scientific Collaboration and Virgo Collaboration) 2017c, Phys. Rev. Lett., 119, 161101

Abbott, B. P., Abbott, R., Abbott, T. D., et al. 2017d, Nature, 551, 85

Abbott, B. P., Abbott, R., Abbott, T. D., et al. 2017e, ApJ, 848, L12

Abbott, B. P., Abbott, R., Abbott, T. D., et al. 2017f, ApJ, 848, L13

Abdo, A. A., Ackermann, M., Ajello, M., et al. 2009, Nature, 462, 331

Ackermann, M., Ajello, M., Albert, A., et al. 2016, ApJ, 823, L2

Antonelli, L. A., D'Avanzo, P., Perna, R., et al. 2009, A&A, 507, L45

Arcavi, I., Hosseinzadeh, G., Howell, D. A., et al. 2017, Nature, 551, 64

Ashall, C., Pian, E., Mazzali, P. A., et al. 2017, arXiv:1702.04339

Aso, Y., Michimura, Y., Somiya, K., et al. 2013, Phys. Rev. D, 88, 043007

Band, D. L. 2006, ApJ, 644, 378

Barkov, M. V., & Pozanenko, A. S. 2011, MNRAS, 417, 2161

Barnes, J., & Kasen, D. 2013, ApJ, 775, 18

Barnes, J., Kasen, D., Wu, M.-R., & Martínez-Pinedo, G. 2016, ApJ, 829, 110

Barniol Duran, R., Nakar, E., Piran, T., & Sari, R. 2015, MNRAS, 448, 417

Barthelmy, S. D., Chincarini, G., Burrows, D. N., et al. 2005, Nature, 438, 994

Baumgartner, W. H., Tueller, J., Markwardt, C. B., et al. 2013, ApJS, 207, 19

Bellm, E. 2014, The Third Hot-wiring the Transient Universe Workshop, 27

Bellm, E., & Kulkarni, S. 2017, Nature Astronomy, 1, 0071

Beloborodov, A. M. 2011, ApJ, 737, 68

Berger, E., Kulkarni, S. R., Pooley, G., et al. 2003, Nature, 426, 154

Berger, E., Price, P. A., Cenko, S. B., et al. 2005, Nature, 438, 988

Berger, E., Fong, W., & Chornock, R. 2013, ApJ, 774, L23

Berger, E. 2014, ARA&A, 52, 43

Blandford, R. D., & McKee, C. F. 1976, Physics of Fluids, 19, 1130

Blandford, R. D., & Znajek, R. L. 1977, MNRAS, 179, 433

Blandford, R. D., & Königl, A. 1979, ApJ, 232, 34

Blandford, R. D., & Payne, D. G. 1982, MNRAS, 199, 883

Bloom, J. S., Djorgovski, S. G., Kulkarni, S. R., & Frail, D. A. 1998, ApJ, 507, L25

Bloom, J. S., Kulkarni, S. R., Price, P. A., et al. 2002, ApJ, 572, L45

Bloom, J. S., Prochaska, J. X., Pooley, D., et al. 2006, ApJ, 638, 354

Bloom, J. S., Giannios, D., Metzger, B. D., et al. 2011, Science, 333, 203

Bodaghee, A., Tomsick, J. A., Pottschmidt, K., et al. 2013, ApJ, 775, 98

Bogomazov, A. I., Lipunov, V. M., & Tutukov, A. V. 2007, Astronomy Reports, 51, 308

Böttcher, M., Reimer, A., Sweeney, K., & Prakash, A. 2013, ApJ, 768, 54

Böttcher, M. 2016, Galaxies, 4, 22

Bray, J. C., & Eldridge, J. J. 2016, MNRAS, 461, 3747

Bromberg, O., Nakar, E., Piran, T., & Sari, R. 2011, ApJ, 740, 100

Bromberg, O., Nakar, E., Piran, T., & Sari, R. 2013, ApJ, 764, 179

Burbridge, G. R. 1956, Phys. Rev., 103, 264

Burbridge, G. R. 1959, ApJ, 129, 849

Burrows, D. N., Kennea, J. A., Ghisellini, G., et al. 2011, Nature, 476, 421

Campana, S., Mangano, V., Blustin, A. J., et al. 2006, Nature, 442, 1008

Cano, Z., de Ugarte Postigo, A., Pozanenko, A., et al. 2014, A&A, 568, A19

Casares, J., & Charles, P. A. 1994, MNRAS, 271, L5

Castro-Tirado, A. J., de Ugarte Postigo, A., Gorosabel, J., et al. 2005, A&A, 439, L15

Cavagnolo, K. W., McNamara, B. R., Nulsen, P. E. J., et al. 2010, ApJ, 720, 1066

Cenko, S. B., Krimm, H. A., Horesh, A., et al. 2012, ApJ, 753, 77

Cenko, S. B., Kulkarni, S. R., Horesh, A., et al. 2013, ApJ, 769, 130

Cenko, S. B., Urban, A. L., Perley, D. A., et al. 2015, ApJ, 803, L24

Chen, W.-X., & Beloborodov, A. M. 2007, ApJ, 657, 383

Chevalier, R. A., & Li, Z.-Y. 2000, ApJ, 536, 195

Ciolfi, R., Kastaun, W., Giacomazzo, B., et al. 2017, Phys. Rev. D, 95, 063016

Connaughton, V., Burns, E., Goldstein, A., et al. 2016, ApJ, 826, L6

Connaughton, V., Blacburn, L., Briggs, M.S., et al. 2017, GCN 21506

Corbel, S., Fender, R. P., Tzioumis, A. K., et al. 2000, A&A, 359, 251

Corbel, S., Nowak, M. A., Fender, R. P., Tzioumis, A. K., & Markoff, S. 2003, A&A, 400, 1007

Corbel, S., Dubus, G., Tomsick, J. A., et al. 2012, MNRAS, 421, 2947

Corbel, S., Coriat, M., Brocksopp, C., et al. 2013, MNRAS, 428, 2500

Cordier, B., Götz, D., & Motch, C. 2018, arXiv:1802.01681

Corral-Santana, J. M., Casares, J., Muñoz-Darias, T., et al. 2016, A&A, 587, A61

Corsi, A., Hallinan, G., Mooley, K., et al. 2017, GCN 21815

Costa, E., Frontera, F., Heise, J., et al. 1997, Nature, 387, 783

Coulter, D. A., Foley, R. J., Kilpatrick, C. D., et al. 2017, Science, 358, 1556

Covino, S., Wiersema, K., Fan, Y. Z., et al. 2017, Nature Astronomy, 1, 791

Coward, D. M., Howell, E. J., Piran, T., et al. 2012, MNRAS, 425, 2668

Coward, D. M., Branchesi, M., Howell, E. J., Lasky, P. D., & Böer, M. 2014, MNRAS, 445, 3575

Cowperthwaite, P. S., Berger, E., Villar, V. A., et al. 2017, ApJ, 848, L17

D'Avanzo, P., Salvaterra, R., Bernardini, M. G., et al. 2014, MNRAS, 442, 2342

D'Elia, V., Pian, E., Melandri, A., et al. 2015, A&A, 577, A116

Daigne, F., & Mochkovitch, R. 1998, MNRAS, 296, 275

Daigne, F., Bošnjak, Ž., & Dubus, G. 2011, A&A, 526, A110

Deaton, M. B., Duez, M. D., Foucart, F., et al. 2013, ApJ, 776, 47

Della Valle, M., Malesani, D., Benetti, S., et al. 2006a, IAU Circ., 8696, 1

Della Valle, M., Chincarini, G., Panagia, N., et al. 2006b, Nature, 444, 1050

Dermer, C. D., Chiang, J., & Mitman, K. E. 2000, ApJ, 537, 785

Dessart, L., Ott, C. D., Burrows, A., Rosswog, S., & Livne, E. 2009, ApJ, 690, 1681

Dewdney, P. E., Hall, P. J., Schilizzi, R. T., & Lazio, T. J. L. W. 2009, IEEE Proceedings, 97, 1482

Dietrich, T., Bernuzzi, S., Ujevic, M., & Brügmann, B. 2015, Phys. Rev. D, 91, 124041

Dietrich, T., & Ujevic, M. 2017, Classical and Quantum Gravity, 34, 105014

Dionysopoulou, K., Alic, D., & Rezzolla, L. 2015, Phys. Rev. D, 92, 084064

Djorgovski, S. G., Kulkarni, S. R., Bloom, J. S., et al. 1998, ApJ, 508, L17

Drout, M. R., Piro, A. L., Shappee, B. J., et al. 2017, Science, 358, 1570

Dubus, G., Cerutti, B., & Henri, G. 2010, MNRAS, 404, L55

Eichler, D., Livio, M., Piran, T., & Schramm, D. N. 1989, Nature, 340, 126

Evans, P. A., Kennea, J. A., Breeveld, A. A., et al. 2017a, GCN 21550

Evans, P. A., Cenko, S. B., Kennea, J. A., et al. 2017, Science, 358, 1565

Falcke, H., Körding, E., & Markoff, S. 2004, A&A, 414, 895

Fender, R. P., & Pooley, G. G. 1998, MNRAS, 300, 573

Fender, R. P. 2001, MNRAS, 322, 31

Fender, R., & Belloni, T. 2004, ARA&A, 42, 317

Fender, R. P., Belloni, T. M., & Gallo, E. 2004, MNRAS, 355, 1105

Fenimore, E. E., Epstein, R. I., & Ho, C. 1993, A&AS, 97, 59

Fermi LAT Collaboration, Abdo, A. A., Ackermann, M., et al. 2009, Science, 326, 1512

Fishman, G. J., & Meegan, C. A. 1995, ARA&A, 33, 415

Fong, W., Berger, E., Margutti, R., & Zauderer, B. A. 2015, ApJ, 815, 102

Foucart, F., Duez, M. D., Kidder, L. E., et al. 2012, Phys. Rev. D, 85, 044015

Frail, D. A., Kulkarni, S. R., Nicastro, L., Feroci, M., & Taylor, G. B. 1997, Nature, 389, 261

Frail, D. A., Berger, E., Galama, T., et al. 2000, ApJ, 538, L129

Fruchter, A. S., Levan, A. J., Strolger, L., et al. 2006, Nature, 441, 463

Fynbo, J. P. U., Watson, D., Thöne, C. C., et al. 2006, Nature, 444, 1047

Gall, C., Hjorth, J., Rosswog, S., Tanvir, N. R., & Levan, A. J. 2017, ApJ, 849, L19

Gal-Yam, A., Fox, D. B., Price, P. A., et al. 2006, Nature, 444, 1053

Galama, T. J., Vreeswijk, P. M., van Paradijs, J., et al. 1998, Nature, 395, 670

Gao, H., Ding, X., Wu, X.-F., Zhang, B., & Dai, Z.-G. 2013, ApJ, 771, 86

Gao, H., Ding, X., Wu, X.-F., Dai, Z.-G., & Zhang, B. 2015, ApJ, 807, 163

Gehrels, N., Chincarini, G., Giommi, P., et al. 2004, ApJ, 611, 1005

Gehrels, N., Sarazin, C. L., O'Brien, P. T., et al. 2005, Nature, 437, 851

Gehrels, N., Norris, J. P., Barthelmy, S. D., et al. 2006, Nature, 444, 1044

Ghirlanda, G., Nava, L., Ghisellini, G., Celotti, A., & Firmani, C. 2009, A&A, 496, 585

Ghirlanda, G., Nava, L., Ghisellini, G., et al. 2012, MNRAS, 420, 483

Ghirlanda, G., Ghisellini, G., Salvaterra, R., et al. 2013, MNRAS, 428, 1410

Ghirlanda, G., Salvaterra, R., Campana, S., et al. 2015, A&A, 578, A71

Ghirlanda, G., Salafia, O. S., Pescalli, A., et al. 2016, A&A, 594, A84

Ghisellini, G. 1999, High Energy Processes in Accreting Black Holes, 161, 249

Goldstein, A., Connaughton, V., Briggs, M. S., & Burns, E. 2016, ApJ, 818, 18

Goldstein, A., Veras, P., von Kienlin, A., et al. 2017, GCN 21528

Goldstein, A., Veres, P., Burns, E., et al. 2017, ApJ, 848, L14

Gompertz, B. P., Levan, A. J., Tanvir, N. R., et al. 2017, arXiv:1710.05442

Gottlieb, O., Nakar, E., Piran, T., & Hotokezaka, K. 2017, arXiv:1710.05896

Gottlieb, O., Nakar, E., & Piran, T. 2018, MNRAS, 473, 576

Götz, D., Laurent, P., Lebrun, F., Daigne, F., & Bošnjak, Ž. 2009, ApJ, 695, L208

Gou, L. J., Dai, Z. G., Huang, Y. F., & Lu, T. 2001, A&A, 368, 464

Granot, J., & Sari, R. 2002, ApJ, 568, 820

Granot, J., Panaitescu, A., Kumar, P., & Woosley, S. E. 2002, ApJ, 570, L61

Granot, J. 2007, Revista Mexicana de Astronomia y Astrofisica, vol. 27, 27, 140

Granot, J., & Piran, T. 2012, MNRAS, 421, 570

Greiner, J., Mazzali, P. A., Kann, D. A., et al. 2015, Nature, 523, 189

Gruber, D., Goldstein, A., Weller von Ahlefeld, V., et al. 2014, ApJS, 211, 12

Gu, W.-M., Liu, T., & Lu, J.-F. 2006, ApJ, 643, L87

Guetta, D., & Piran, T. 2006, A&A, 453, 823

Haggard, D., Nynka, M., Ruan, J. J., et al. 2017, ApJ, 848, L25

Hallinan, G., Corsi, A., Mooley, K. P., et al. 2017, Science, 358, 1579

Hansen, B. M. S., & Lyutikov, M. 2001, MNRAS, 322, 695

Harrison, F. A., Bloom, J. S., Frail, D. A., et al. 1999, ApJ, 523, L121

Hascoët, R., Beloborodov, A. M., Daigne, F., & Mochkovitch, R. 2014, ApJ, 782, 5

Heinz, S., & Sunyaev, R. A. 2003, MNRAS, 343, L59

Hjellming, R. M., & Rupen, M. P. 1995, Nature, 375, 464

Hjorth, J., Sollerman, J., Møller, P., et al. 2003, Nature, 423, 847

Hjorth, J., Sollerman, J., Gorosabel, J., et al. 2005, ApJ, 630, L117

Hjorth, J., Watson, D., Fynbo, J. P. U., et al. 2005, Nature, 437, 859

Hotokezaka, K., Kyutoku, K., Tanaka, M., et al. 2013, ApJ, 778, L16

Hotokezaka, K., Kiuchi, K., Kyutoku, K., et al. 2013, Phys. Rev. D, 87, 024001

Hotokezaka, K., & Piran, T. 2015, MNRAS, 450, 1430

Hotokezaka, K., Nissanke, S., Hallinan, G., et al. 2016, ApJ, 831, 190

Huang, Y. F., Dai, Z. G., & Lu, T. 2002, MNRAS, 332, 735

Huang, Y. F., Wu, X. F., Dai, Z. G., Ma, H. T., & Lu, T. 2004, ApJ, 605, 300

Huppenkothen, D., Younes, G., Ingram, A., et al. 2017, ApJ, 834, 90

Hurley, K., Berger, E., Castro-Tirado, A., et al. 2002, ApJ, 567, 447

Ioka, K., & Nakamura, T. 2001, ApJ, 554, L163

Janiuk, A., Yuan, Y., Perna, R., & Di Matteo, T. 2007, ApJ, 664, 1011

Jermak, H., Steele, I. A., Lindfors, E., et al. 2016, MNRAS, 462, 4267

Jin, Z. P., Yan, T., Fan, Y. Z., & Wei, D. M. 2007, ApJ, 656, L57

Jin, Z.-P., Li, X., Cano, Z., et al. 2015, ApJ, 811, L22

Jin, Z.-P., Hotokezaka, K., Li, X., et al. 2016, Nature Communications, 7, 12898

Jin, Z.-P., Li, X., Wang, H., et al. 2017, arXiv:1708.07008

Jorstad, S. G., Marscher, A. P., Lister, M. L., et al. 2005, AJ, 130, 1418

Jorstad, S. G., Marscher, A. P., Smith, P. S., et al. 2013, ApJ, 773, 147

Kathirgamaraju, A., Barniol Duran, R., & Giannios, D. 2016, MNRAS, 461, 1568

Kathirgamaraju, A., Barniol Duran, R., & Giannios, D. 2018, MNRAS, 473, L121

Kawaguchi, K., Kyutoku, K., Shibata, M., & Tanaka, M. 2016, ApJ, 825, 52

Katz, J. I. 1994, ApJ, 422, 248

Katz, J. I. 1994, ApJ, 432, L107

Kehoe, R., Akerlof, C., Balsano, R., et al. 2001, ApJ, 554, L159

Kilpatrick, C. D., Foley, R. J., Kasen, D., et al. 2017, Science, 358, 1583

Kisaka, S., Ioka, K., & Takami, H. 2015a, ApJ, 802, 119

Kisaka, S., Ioka, K., & Nakamura, T. 2015b, ApJ, 809, L8

Kisaka, S., Ioka, K., Kashiyama, K., & Nakamura, T. 2017, arXiv:1711.00243

Kistler, M. D., Yüksel, H., Beacom, J. F., & Stanek, K. Z. 2008, ApJ, 673, L119

Kiuchi, K., Sekiguchi, Y., Shibata, M., & Taniguchi, K. 2010, Physical Review Letters, 104, 141101

Klebesadel, R. W., Strong, I. B., & Olson, R. A. 1973, ApJ, 182, L85

Kluźniak, W., & Lee, W. H. 1998, ApJ, 494, L53

Kohri, K., & Mineshige, S. 2002, ApJ, 577, 311

Kobayashi, S., Piran, T., & Sari, R. 1997, ApJ, 490, 92

Kobayashi, S., Piran, T., & Sari, R. 1999, ApJ, 513, 669

Kobayashi, S., & Sari, R. 2000, ApJ, 542, 819

Kobayashi, S. 2000, ApJ, 545, 807

Kobayashi, S., & Sari, R. 2001, ApJ, 551, 934

Kobayashi, S., Ryde, F., & MacFadyen, A. 2002, ApJ, 577, 302

Kobayashi, S., & Zhang, B. 2003, ApJ, 582, L75

Kobayashi, S., & Mészáros, P. 2003, ApJ, 589, 861

Kobayashi, S., Zhang, B., Mészáros, P., & Burrows, D. 2007, ApJ, 655, 391

Kochanek, C. S. 1992, ApJ, 398, 234

Kochanek, C. S., & Piran, T. 1993, ApJ, 417, L17

Kopač, D., Mundell, C. G., Kobayashi, S., et al. 2015, ApJ, 806, 179

Kouveliotou, C., Meegan, C. A., Fishman, G. J., et al. 1993, ApJ, 413, L101

Fox, D. B., Frail, D. A., Price, P. A., et al. 2005, Nature, 437, 845

Kulkarni, S. R. 2005, arXiv:astro-ph/0510256

Kumar, P., & Panaitescu, A. 2000, ApJ, 541, L51

Kumar, P., & Granot, J. 2003, ApJ, 591, 1075

Kumar, P., & Zhang, B. 2015, Phys. Rep., 561, 1

Kyutoku, K., Ioka, K., & Shibata, M. 2014, MNRAS, 437, L6

Kyutoku, K., Ioka, K., Okawa, H., Shibata, M., & Taniguchi, K. 2015, Phys. Rev. D, 92, 044028

Lamb, D. Q., Graziani, C., & Smith, I. A. 1993, ApJ, 413, L11

Lamb, D. Q., Donaghy, T. Q., & Graziani, C. 2005, ApJ, 620, 355

Lamb, G. P., & Kobayashi, S. 2016, ApJ, 829, 112

Lamb, G. P., Kobayashi, S., & Pian, E. 2017a, MNRAS, 472, 475

Lamb, G. P, Tanaka, M., & Kobayashi, S. 2018, MNRAS,

Lamb, G. P., & Kobayashi, S. 2017a, MNRAS, 472, 4953

Lamb, G. P, & Kobayashi, S. 2017b, arXiv:1710.05857

Lattimer, J. M., & Schramm, D. N. 1974, ApJ, 192, L145

Lattimer, J. M., Mackie, F., Ravenhall, D. G., & Schramm, D. N. 1977, ApJ, 213, 225

Lazzati, D., & Begelman, M. C. 2005, ApJ, 629, 903

Lazzati, D., Deich, A., Morsony, B. J., & Workman, J. C. 2017a, MNRAS, 471, 1652

Lazzati, D., López-Cámara, D., Cantiello, M., et al. 2017b, ApJ, 848, L6

Lazzati, D., Perna, R., Morsony, B. J., et al. 2017c, arXiv:1712.03237

Lee, H. K., Wijers, R. A. M. J., & Brown, G. E. 2000, Phys. Rep., 325, 83

Lei, W. H., Wang, D. X., Zhang, L., et al. 2009, ApJ, 700, 1970

Lei, W.-H., Zhang, B., & Liang, E.-W. 2013, ApJ, 765, 125

Levan, A. J., Tanvir, N. R., Cenko, S. B., et al. 2011, Science, 333, 199

Levan, A. J., Tanvir, N. R., Fruchter, A. S., et al. 2014, ApJ, 792, 115

Levan, A., Crowther, P., de Grijs, R., et al. 2016, Space Sci. Rev., 202, 33

Lei, W.-H., Zhang, B., & Liang, E.-W. 2013, ApJ, 765, 125

Levinson, A., & Eichler, D. 2003, ApJ, 594, L19

Lewin, W. H. G., & van der Klis, M. 2006, Compact stellar X-ray sources, 39

Li, L.-X., & Paczyński, B. 1998, ApJ, 507, L59

Li, L.-X. 2000, Phys. Rev. D, 61, 084016

Li, L.-X. 2008, MNRAS, 388, 1487

Liang, E.-W., Yi, S.-X., Zhang, J., et al. 2010, ApJ, 725, 2209

Ling, Z., Zhang, S. N., & Tang, S. 2009, ApJ, 695, 1111

Liodakis, I., & Pavlidou, V. 2015, MNRAS, 451, 2434

Lippuner, J., & Roberts, L. F. 2015, ApJ, 815, 82

Lippuner, J., & Roberts, L. F. 2017, ApJS, 233, 18

Lipunov, V. M., Postnov, K. A., & Prokhorov, M. E. 2001, Astronomy Reports, 45, 236

Lister, M. L., & Marscher, A. P. 1997, ApJ, 476, 572

Lister, M. L., Cohen, M. H., Homan, D. C., et al. 2009, AJ, 138, 1874-1892

Lithwick, Y., & Sari, R. 2001, ApJ, 555, 540

Loeb, A. 2016, ApJ, 819, L21

Loh, A., Corbel, S., Dubus, G., et al. 2016, MNRAS, 462, L111

Longair, M. S. 1994, High energy astrophysics. Volume 2. Stars, the Galaxy and the interstellar medium., by Longair, M. S.. Cambridge University Press, Cambridge (UK), 1994, 410 p., ISBN 0-521-43439-4.

LSST Science Collaboration, Abell, P. A., Allison, J., et al. 2009, arXiv:0912.0201

Lyman, J. D., Lamb, G. P., Levan, A. J., et al. 2018, arXiv:1801.02669

Lyutikov, M., & Blandford, R. 2002, Beaming and Jets in Gamma Ray Bursts, 146

Ma, R., Xie, F.-G., & Hou, S. 2014, ApJ, 780, L14

MacDonald, R. K. D., Bailyn, C. D., Buxton, M., et al. 2014, ApJ, 784, 2

Madau, P., & Dickinson, M. 2014, ARA&A, 52, 415

Malesani, D., Tagliaferri, G., Chincarini, G., et al. 2004, ApJ, 609, L5

Mandel, I. 2018, ApJ, 853, L12

Mao, S., Narayan, R., & Piran, T. 1994, ApJ, 420, 171

Margalit, B., & Piran, T. 2015, MNRAS, 452, 3419

Margutti, R., Berger, E., Fong, W., et al. 2017a, ApJ, 848, L20

Margutti, R., Metzger, B. D., Chornock, R., et al. 2017b, ApJ, 836, 25

Margutti, R., Alexander, K. D., Xie, X., et al. 2018, arXiv:1801.03531

Marscher, A. P., Jorstad, S. G., Gómez, J.-L., et al. 2002, Nature, 417, 625

Marscher, A. P. 2006a, Relativistic Jets: The Common Physics of AGN, Microquasars, and Gamma-Ray Bursts, 856, 1

Marscher, A. 2006b, VI Microquasar Workshop: Microquasars and Beyond, 25.1

Mazzali, P. A., Deng, J., Tominaga, N., et al. 2003, ApJ, 599, L95

McClintock, J. E., Remillard, R. A., Rupen, M. P., et al. 2009, ApJ, 698, 1398

McKinney, J. C. 2005, ApJ, 630, L5

Meegan, C. A., Fishman, G. J., Wilson, R. B., et al. 1992, Nature, 355, 143

Melandri, A., Pian, E., Ferrero, P., et al. 2012, A&A, 547, A82

Melandri, A., Pian, E., D'Elia, V., et al. 2014, A&A, 567, A29

Meng, Y.-Z., Geng, J.-J., Zhang, B.-B., et al. 2018, arXiv:1801.01410

Merloni, A., Heinz, S., & di Matteo, T. 2003, MNRAS, 345, 1057

Meszaros, P., & Rees, M. J. 1993, ApJ, 405, 278

Mészáros, P., & Rees, M. J. 1997, ApJ, 476, 232

Mészáros, P. 2002, ARA&A, 40, 137

Metzger, B. D., Martínez-Pinedo, G., Darbha, S., et al. 2010, MNRAS, 406, 2650

Metzger, B. D., & Berger, E. 2012, ApJ, 746, 48

Metzger, B. D., & Fernández, R. 2014, MNRAS, 441, 3444

Metzger, B. D., Bauswein, A., Goriely, S., & Kasen, D. 2015, MNRAS, 446, 1115

Metzger, B. D., & Zivancev, C. 2016, MNRAS, 461, 4435

Metzger, B. D. 2017a, Living Reviews in Relativity, 20, 3

Metzger, B. D. 2017b, arXiv:1710.05931

Metzger, M. R., Djorgovski, S. G., Kulkarni, S. R., et al. 1997, Nature, 387, 878

Miller-Jones, J. C. A., Fender, R. P., & Nakar, E. 2006, MNRAS, 367, 1432

Mirabel, I. F., Dhawan, V., Chaty, S., et al. 1998, A&A, 330, L9

Mirabel, I. F., & Rodríguez, L. F. 1999, ARA&A, 37, 409

Mochkovitch, R., Hernanz, M., Isern, J., & Martin, X. 1993, Nature, 361, 236

Modjaz, M., Stanek, K. Z., Garnavich, P. M., et al. 2006, ApJ, 645, L21

Mooley, K. P., Hallinan, G., & Corsi, A. 2017a, GCN 21814

Mooley, K. P., Nakar, E., Hotokezaka, K., et al. 2018, Nature, 554, 207

Morsony, B. J., Lazzati, D., & Begelman, M. C. 2010, ApJ, 723, 267

Mundell, C. G., Kopač, D., Arnold, D. M., et al. 2013, Nature, 504, 119

Muñoz-Darias, T., Casares, J., & Martínez-Pais, I. G. 2008, MNRAS, 385, 2205

Murguia-Berthier, A., Ramirez-Ruiz, E., Kilpatrick, C. D., et al. 2017, ApJ, 848, L34

Nagakura, H., Hotokezaka, K., Sekiguchi, Y., Shibata, M., & Ioka, K. 2014, ApJ, 784, L28

Nakar, E., & Piran, T. 2002, MNRAS, 330, 920

Nakar, E., & Piran, T. 2003, New A, 8, 141

Nakar, E. 2007, Phys. Rep., 442, 166

Nakar, E., & Piran, T. 2011, Nature, 478, 82

Nakar, E., & Piran, T. 2017, ApJ, 834, 28

Narayan, R., Paczynski, B., & Piran, T. 1992, ApJ, 395, L83

Narayan, R., Piran, T., & Kumar, P. 2001, ApJ, 557, 949

Nemiroff, R. J. 1994, Comments on Astrophysics, 17, 189

Nemmen, R. S., Georganopoulos, M., Guiriec, S., et al. 2012, Science, 338, 1445

Nicholl, M., Berger, E., Kasen, D., et al. 2017, ApJ, 848, L18

Nissanke, S., Holz, D. E., Hughes, S. A., Dalal, N., & Sievers, J. L. 2010, ApJ, 725, 496

Nissanke, S., Kasliwal, M., & Georgieva, A. 2013, ApJ, 767, 124

O'Shaughnessy, R., Bellovary, J. M., Brooks, A., et al. 2017, MNRAS, 464, 2831

Olivares E., F., Greiner, J., Schady, P., et al. 2015, A&A, 577, A44

Orosz, J. A., Steiner, J. F., McClintock, J. E., et al. 2011, ApJ, 730, 75

Orosz, J. A., McClintock, J. E., Aufdenberg, J. P., et al. 2011, ApJ, 742, 84

Paczynski, B. 1986, ApJ, 308, L43

Paczynski, B. 1990, ApJ, 363, 218

Paczynski, B. 1991, Acta Astron., 41, 257

Paczynski, B., & Rhoads, J. E. 1993, ApJ, 418, L5

Panaitescu, A., Mészáros, P., & Rees, M. J. 1998, ApJ, 503, 314

Panaitescu, A., & Mészáros, P. 1999, ApJ, 526, 707

Panaitescu, A., & Kumar, P. 2000, ApJ, 543, 66

Panaitescu, A., & Kumar, P. 2002, ApJ, 571, 779

Panaitescu, A. 2005, MNRAS, 363, 1409

Paul, D. 2017, arXiv:1710.05620

Pe'er, A., Mészáros, P., & Rees, M. J. 2005, ApJ, 635, 476

Pe'er, A., Mészáros, P., & Rees, M. J. 2006a, ApJ, 642, 995

Pe'er, A., Mészáros, P., & Rees, M. J. 2006b, ApJ, 652, 482

Pedersen, H., Jaunsen, A. O., Grav, T., et al. 1998, ApJ, 496, 311

Peng, F., Königl, A., & Granot, J. 2005, ApJ, 626, 966

Penner, A. J., Andersson, N., Samuelsson, L., Hawke, I., & Jones, D. I. 2011, Phys. Rev. D, 84, 103006

Pepe, C., Vila, G. S., & Romero, G. E. 2015, A&A, 584, A95

Perego, A., Rosswog, S., Cabezón, R. M., et al. 2014, MNRAS, 443, 3134

Perley, D. A., Cenko, S. B., Bloom, J. S., et al. 2009, AJ, 138, 1690

Perley, D. A., Cenko, S. B., Corsi, A., et al. 2014, ApJ, 781, 37

Perna, R., Armitage, P. J., & Zhang, B. 2006, ApJ, 636, L29

Perna, R., Lazzati, D., & Giacomazzo, B. 2016, ApJ, 821, L18

Pescalli, A., Ghirlanda, G., Salafia, O. S., et al. 2015, MNRAS, 447, 1911

Peters, P. C., & Mathews, J. 1963, Physical Review, 131, 435

Petrillo, C. E., Dietz, A., & Cavaglià, M. 2013, ApJ, 767, 140

Phinney, E. S. 1991, ApJ, 380, L17

Pian, E., Mazzali, P. A., Masetti, N., et al. 2006, Nature, 442, 1011

Pian, E., D'Avanzo, P., Benetti, S., et al. 2017, Nature, 551, 67

Piano, G., Munar-Adrover, P., Verrecchia, F., Tavani, M., & Trushkin, S. A. 2017, ApJ, 839, 84

Piner, B. G., Pushkarev, A. B., Kovalev, Y. Y., et al. 2012, ApJ, 758, 84

Piran, T. 1992, ApJ, 389, L45

Piran, T., Shemi, A., & Narayan, R. 1993, MNRAS, 263, 861

Piran, T. 1999, Phys. Rep., 314, 575

Piran, T. 2004, Reviews of Modern Physics, 76, 1143

Piran, T. 2005, Magnetic Fields in the Universe: From Laboratory and Stars to Primordial Structures., 784, 164

Piran, T., Nakar, E., & Rosswog, S. 2013, MNRAS, 430, 2121

Piron, F. 2016, Comptes Rendus Physique, 17, 617

Planck Collaboration, Ade, P. A. R., Aghanim, N., et al. 2016, A&A, 594, A13

Popham, R., Woosley, S. E., & Fryer, C. 1999, ApJ, 518, 356

Prentice, S. J., Mazzali, P. A., Pian, E., et al. 2016, MNRAS, 458, 2973

Punturo, M., Abernathy, M., Acernese, F., et al. 2010, Classical and Quantum Gravity, 27, 194002

Qin, S.-F., Liang, E.-W., Lu, R.-J., Wei, J.-Y., & Zhang, S.-N. 2010, MNRAS, 406, 558

Rees, M. J., & Meszaros, P. 1992, MNRAS, 258, 41P

Rees, M. J., & Meszaros, P. 1994, ApJ, 430, L93

Reid, M. J., McClintock, J. E., Narayan, R., et al. 2011, ApJ, 742, 83

Reid, M. J., McClintock, J. E., Steiner, J. F., et al. 2014, ApJ, 796, 2

Riess, A. G., Macri, L. M., Hoffmann, S. L., et al. 2016, ApJ, 826, 56

Rezzolla, L., Giacomazzo, B., Baiotti, L., et al. 2011, ApJ, 732, L6

Rhoads, J. E. 1999, ApJ, 525, 737

Rhoads, J. E. 2003, ApJ, 591, 1097

Ricker, G. R., Atteia, J.-L., Crew, G. B., et al. 2003, Gamma-Ray Burst and Afterglow Astronomy 2001: A Workshop Celebrating the First Year of the HETE Mission, 662, 3

Robertson, B. E., & Ellis, R. S. 2012, ApJ, 744, 95

Rodriguez, J., Corbel, S., & Tomsick, J. A. 2003, ApJ, 595, 1032

Rodriguez, J., Shaw, S. E., Hannikainen, D. C., et al. 2008, ApJ, 675, 1449-1458

Rodriguez, J., Grinberg, V., Laurent, P., et al. 2015, ApJ, 807, 17

Rossi, E., Lazzati, D., & Rees, M. J. 2002, MNRAS, 332, 945

Rossi, E. M., Lazzati, D., Salmonson, J. D., & Ghisellini, G. 2004, MNRAS, 354, 86

Rosswog, S., Davies, M. B., Thielemann, F.-K., & Piran, T. 2000, A&A, 360, 171

Rosswog, S. 2013, Nature, 500, 535

Ruan, J. J., Nynka, M., Haggard, D., Kalogera, V., & Evans, P. 2018, ApJ, 853, L4

Ruderman, M. 1975, Seventh Texas Symposium on Relativistic Astrophysics, 262, 164

Ruffert, M., & Janka, H.-T. 2001, A&A, 380, 544

Ruiz, M., Lang, R. N., Paschalidis, V., & Shapiro, S. L. 2016, ApJ, 824, L6

Rybicki, G. B., & Lightman, A. P. 1979, New York, Wiley-Interscience, 1979. 393 p.,

Rybicki, G. B., & Lightman, A. P. 1986, Radiative Processes in Astrophysics, by George B. Rybicki, Alan P. Lightman, pp. 400. ISBN 0-471-82759-2. Wiley-VCH , June 1986., 400

Sabatini, S., Roberts, S., & Davies, J. 2003, Ap&SS, 285, 97

Saikia, P., Körding, E., & Falcke, H. 2016, MNRAS, 461, 297

Salafia, O. S., Ghisellini, G., Pescalli, A., Ghirlanda, G., & Nappo, F. 2015, MNRAS, 450, 3549

Salafia, O. S., Ghisellini, G., & Ghirlanda, G. 2018, MNRAS, 474, L7

Salmonson, J. D., & Galama, T. J. 2002, ApJ, 569, 682

Salmonson, J. D. 2003, ApJ, 592, 1002

Sari, R., & Piran, T. 1995, ApJ, 455, L143

Sari, R., Narayan, R., & Piran, T. 1996, ApJ, 473, 204

Sari, R., & Piran, T. 1997, ApJ, 485, 270

Sari, R. 1997, ApJ, 489, L37

Sari, R. 1998, ApJ, 494, L49

Sari, R., Piran, T., & Narayan, R. 1998, ApJ, 497, L17

Sari, R., & Piran, T. 1999, ApJ, 520, 641

Sari, R., Piran, T., & Halpern, J. P. 1999, ApJ, 519, L17

Savchenko, V., Ferrigno, C., Mereghetti, S., et al. 2016, ApJ, 820, L36

Savchenko, V., Mereghetti, S., Ferrigno, C., et al. 2017a, GCN 21507

Savchenko, V., Ferrigno, C., Kuulkers, E., et al. 2017b, ApJ, 848, L15

Schmidt, W. K. H. 1978, Nature, 271, 525

Schutz, B. F. 2011, Classical and Quantum Gravity, 28, 125023

Scolnic, D., Kessler, R., Brout, D., et al. 2018, ApJ, 852, L3

Selsing, J., Krühler, T., Malesani, D., et al. 2017, arXiv:1707.01452

Shemi, A., & Piran, T. 1990, ApJ, 365, L55

Siellez, K., Boër, M., & Gendre, B. 2014, MNRAS, 437, 649

Siellez, K., Boer, M., Gendre, B., & Regimbau, T. 2016, arXiv:1606.03043

Sironi, L., & Spitkovsky, A. 2011, ApJ, 726, 75

Shapiro, S. L. 2017, Phys. Rev. D, 95, 101303

Shaposhnikov, N., & Titarchuk, L. 2009, ApJ, 699, 453

Shibata, M., Fujibayashi, S., Hotokezaka, K., et al. 2017, Phys. Rev. D, 96, 123012

Smartt, S. J., Chen, T.-W., Jerkstrand, A., et al. 2017, Nature, 551, 75

Sparre, M., Sollerman, J., Fynbo, J. P. U., et al. 2011, ApJ, 735, L24

Stanek, K. Z., Bersier, D., Garnavich, P. M., Holland, S. T., & Matheson, T. 2003, Bulletin of the American Astronomical Society, 35, 132.03

Starling, R. L. C., Wiersema, K., Levan, A. J., et al. 2011, MNRAS, 411, 2792

Steele, I. A., Mundell, C. G., Smith, R. J., Kobayashi, S., & Guidorzi, C. 2009, Nature, 462, 767

Sun, H., Zhang, B., & Li, Z. 2015, ApJ, 812, 33

Sun, H., Zhang, B., & Gao, H. 2017, ApJ, 835, 7

Szostek, A., Zdziarski, A. A., & McCollough, M. L. 2008, MNRAS, 388, 1001

Tanaka, M., & Hotokezaka, K. 2013, ApJ, 775, 113

Tanaka, M., Hotokezaka, K., Kyutoku, K., et al. 2014, ApJ, 780, 31

Tanaka, M. 2016, Advances in Astronomy, 2016, 634197

Tanaka, Y. T., Itoh, R., Uemura, M., et al. 2016, ApJ, 823, 35

Tanaka, M., Kato, D., Gaigalas, G., et al. 2018, ApJ, 852, 109

Tanaka, M., Utsumi, Y., Mazzali, P. A., et al. 2017, PASJ, 69, 102

Tang, Q.-W., Peng, F.-K., Wang, X.-Y., & Tam, P.-H. T. 2015, ApJ, 806, 194

Tanvir, N. R., Levan, A. J., Fruchter, A. S., et al. 2013, Nature, 500, 547

Tanvir, N. R., Levan, A. J., González-Fernández, C., et al. 2017, ApJ, 848, L27

Tavani, M., Bulgarelli, A., Piano, G., et al. 2009, Nature, 462, 620

Tetarenko, B. E., Sivakoff, G. R., Heinke, C. O., & Gladstone, J. C. 2016, ApJS, 222, 15

Thompson, C., Mészáros, P., & Rees, M. J. 2007, ApJ, 666, 1012

Toma, K., Ioka, K., Yamazaki, R., & Nakamura, T. 2006, ApJ, 640, L139

Troja, E., Rosswog, S., & Gehrels, N. 2010, ApJ, 723, 1711

Troja, E., Piro, L., van Eerten, H., et al. 2017, Nature, 551, 71

Tsang, D., Read, J. S., Hinderer, T., Piro, A. L., & Bondarescu, R. 2012, Physical Review Letters, 108, 011102

Tsutsui, R., Yonetoku, D., Nakamura, T., Takahashi, K., & Morihara, Y. 2013, MNRAS, 431, 1398

Türler, M., Courvoisier, T. J.-L., Chaty, S., & Fuchs, Y. 2004, A&A, 415, L35

Urry, C. M., & Padovani, P. 1995, PASP, 107, 803

Valenti, S., David, Sand, J., et al. 2017, ApJ, 848, L24

van Eerten, H., Zhang, W., & MacFadyen, A. 2010, ApJ, 722, 235

van Eerten, H. J., & MacFadyen, A. I. 2012, ApJ, 751, 155

van Paradijs, J., Groot, P. J., Galama, T., et al. 1997, Nature, 386, 686

van Putten, M. H. P. M., & Levinson, A. 2003, ApJ, 584, 937

Verrecchia, F., Tavani, M., Ursi, A., et al. 2017, ApJ, 847, L20

Vilhu, O., & Hannikainen, D. C. 2013, A&A, 550, A48

Villasenor, J. S., Lamb, D. Q., Ricker, G. R., et al. 2005, Nature, 437, 855

Virgili, F. J., Zhang, B., Nagamine, K., & Choi, J.-H. 2011a, MNRAS, 417, 3025

Virgili, F. J., Zhang, B., O'Brien, P., & Troja, E. 2011b, ApJ, 727, 109

Vlahakis, N., Peng, F., & Königl, A. 2003, ApJ, 594, L23

Wanderman, D., & Piran, T. 2010, MNRAS, 406, 1944

Wanderman, D., & Piran, T. 2015, MNRAS, 448, 3026

Wang, D. X., Xiao, K., & Lei, W. H. 2002, MNRAS, 335, 655

Wang, F. Y., & Dai, Z. G. 2017, MNRAS, 470, 1101

Wei, D. M., & Jin, Z. P. 2003, A&A, 400, 415

Wollaeger, R. T., Korobkin, O., Fontes, C. J., et al. 2017, arXiv:1705.07084

Woods, E., & Loeb, A. 1995, ApJ, 453, 583

Woosley, S. E., & Bloom, J. S. 2006, ARA&A, 44, 507

Wu, X. F., Dai, Z. G., Huang, Y. F., & Lu, T. 2005, MNRAS, 357, 1197

Xiao, D., Liu, L.-D., Dai, Z.-G., & Wu, X.-F. 2017, ApJ, 850, L41

Yamamoto, T., Shibata, M., & Taniguchi, K. 2008, Phys. Rev. D, 78, 064054

Yamazaki, R., Ioka, K., & Nakamura, T. 2002, ApJ, 571, L31

Yamazaki, R., Asano, K., & Ohira, Y. 2016, Progress of Theoretical and Experimental Physics, 2016, 051E01

Yonetoku, D., Murakami, T., Nakamura, T., et al. 2004, ApJ, 609, 935

Yonetoku, D., Murakami, T., Tsutsui, R., et al. 2010, PASJ, 62, 1495

Yonetoku, D., Murakami, T., Gunji, S., et al. 2011, ApJ, 743, L30

Yost, S. A., Harrison, F. A., Sari, R., & Frail, D. A. 2003, ApJ, 597, 459

Yu, H.-F., Preece, R. D., Greiner, J., et al. 2016, A&A, 588, A135

Yuan, F., & Zhang, B. 2012, ApJ, 757, 56

Yuan, W., Zhang, C., Feng, H., et al. 2015, arXiv:1506.07735

Zanin, R., Fernández-Barral, A., de Oña Wilhelmi, E., et al. 2016, A&A, 596, A55

Zauderer, B. A., Berger, E., Soderberg, A. M., et al. 2011, Nature, 476, 425

Zdziarski, A. A., Pjanka, P., Sikora, M., & Stawarz, Ł. 2014, MNRAS, 442, 3243

Zdziarski, A. A. 2014, MNRAS, 445, 1321

Zdziarski, A. A., Malyshev, D., Chernyakova, M., & Pooley, G. G. 2016, arXiv:1607.05059

Zhang, B., & Mészáros, P. 2002, ApJ, 571, 876

Zhang, B., & Mészáros, P. 2004, International Journal of Modern Physics A, 19, 2385

Zhang, B., Dai, X., Lloyd-Ronning, N. M., & Mészáros, P. 2004, ApJ, 601, L119

Zhang, B., & Kobayashi, S. 2005, ApJ, 628, 315

Zhang, B., Zhang, B.-B., Virgili, F. J., et al. 2009, ApJ, 703, 1696

Zhang, B., & Yan, H. 2011, ApJ, 726, 90

Zhang, B. 2013, ApJ, 763, L22

Zhang, B. 2016, ApJ, 827, L31

Zhang, F.-W., Shao, L., Yan, J.-Z., & Wei, D.-M. 2012, ApJ, 750, 88

Zhang, W., Woosley, S. E., & MacFadyen, A. I. 2003, ApJ, 586, 356

Zhang, W., Woosley, S. E., & Heger, A. 2004, ApJ, 608, 365

Zhang, G. Q., & Wang, F. Y. 2018, ApJ, 852, 1

Zou, Y. C., Wu, X. F., & Dai, Z. G. 2007, A&A, 461, 115